Energy Storage and Generation from Thermopower Waves

by

Joel T. Abrahamson

B. S., Chemical Engineering
University of Kansas, 2006

Submitted to the Department of Chemical Engineering
in Partial Fulfillment of the Requirements for the Degree of

DOCTOR OF PHILOSOPHY IN CHEMICAL ENGINEERING

at the

MASSACHUSETTS INSTITUTE OF TECHNOLOGY

June 2012

Signature of Author: _____
Department of Chemical Engineering
June 2012

Certified by: _____
Michael S. Strano
Professor of Chemical Engineering
Thesis Advisor

Accepted by: _____
Patrick S. Doyle
Professor of Chemical Engineering
Chairman, Committee for Graduate Students

Energy Storage and Generation from Thermopower Waves

by

Joel T. Abrahamson

Submitted to the Department of Chemical Engineering
on May 21, 2012 in Partial Fulfillment
of the Requirements for the Degree of
Doctor of Philosophy in Chemical Engineering

Abstract

The nonlinear coupling between an exothermic chemical reaction and a nanowire or nanotube with large axial heat conduction guides a self-propagating thermal wave along the nano-conduit. The thermal conduit accelerates the wave by rapidly transporting energy to un-reacted fuel. The reaction wave induces what we term a thermopower wave, resulting in an electrical current in the same direction. At up to 7 W/g, peak power density is larger than that of many present micro-scale power sources (e.g. fuel cells, batteries) and even about seven times greater than commercial Li-ion batteries. Thermopower waves also tend to produce unipolar voltage pulses, although conventional thermoelectric theory predicts bipolar voltage. These waves also generate thermopower in excess of previous measurements in carbon nanotubes (CNTs) and therefore could increase figures of merit in a variety of thermoelectric materials.

In this thesis, I have developed the theoretical framework to describe the thermal and chemical profiles of propagating reaction waves, and their electrical properties. My analysis yielded a new analytical solution for one-dimensional reaction and thermal diffusion systems with n^{th}-order kinetics that obviates many approximate or numerical approaches from the past 80 years. A generalized logistic function describes the temperature and concentration profiles within the solid fuel and provides a solution for the wave velocity for a wide range of conditions. This approach offers new insight into such problems spanning several fields in science and engineering, including propulsion and self-propagating high-temperature synthesis (SHS) of materials, as well as the dynamics of thermopower waves.

Temperature and voltage measurements of thermopower waves on CNTs show that they can generate power as much as four times greater than predictions based on reference measurements of the Seebeck coefficient for static temperature gradients. We hypothesize that the excess thermopower stems from a chemical potential gradient across the CNTs. The fuel (*e.g.* picramide) adsorbs and dopes the CNTs ahead of the wave and desorbs and reacts behind the wave front. Furthermore, the excess thermopower depends on the mass of fuel added (relative to CNT mass), and the chemical potential difference matches the magnitude of the excess thermopower. Thus, a major conclusion of this thesis is that coupling to a chemical reaction can boost the performance of thermoelectric materials through differential doping.

Thermopower waves can have well defined velocity oscillations for certain kinetic and thermal parameter values. Cyclotrimethylene-trinitramine (fuel) on multiwalled CNTs (conduit) system generates voltage oscillations of 400 to 5000 Hz. These frequencies agree with velocity oscillations predicted by my thermochemical model of the reaction wave, extended to include thermal transport within the conduits. Thermopower waves could thus find applications as new types of alternating current (AC) batteries and self-powered signal generators, which could easily be miniaturized.

Microelectromechanical systems and sensors would benefit from thermopower wave generators to enable functions such as communications and acceleration that currently require large power packs. Additionally, the "self-discharge" rate of thermopower wave generators is extremely low in contrast to electrochemical storage, since their energy is stored in chemical bonds. Thermopower waves thus enable new energy storage devices and could exceed limitations of conventional thermoelectric devices.

Thesis supervisor: Michael S. Strano
Title: Professor of Chemical Engineering

Table of Contents

Chapter 1

Introduction

1.1 Present Energy Storage Technologies

Portable energy storage and delivery is the cornerstone of modern transportation systems and the proliferation of portable electronic devices and is a rapidly growing field. For example, the global market for rechargeable batteries is projected to grow from $12.3 billion in 2010 to $77.9 billion by 2020[1]. In energy terms, today's annual global production is around 21,000 MWh for Li-ion batteries alone[2], equivalent to about 570,000 gal of gasoline. Additionally, the development of the newest autonomous and mobile sensors, robots,[3] disposable medical diagnostics,[4, 5] and off-grid distributed wireless networks[6], particularly at the micro- and nanoscale, is often hampered today by the lack of high-power-density energy systems of similar size.[7] Each of today's portable energy technologies has its distinct shortcomings.

Batteries are the most familiar form of electrical energy storage, but electrochemical energy density is fundamentally limited compared to storing energy in the chemical bonds of fuels. For example, ethanol has specific energy storage of 26.8 MJ/kg, whereas Li-ion batteries can only store 0.72 MJ/kg, about 2.7% of ethanol[8, 9]. Ethanol's energy density is also about 20 times larger in volume terms. Table 1 expands this comparison for a variety of today's batteries and chemical fuels.[8-12]

Table 1: Energy density of electrochemical and chemical storage materials

	Energy Density (MJ/L)	Specific Energy (MJ/kg)
Electrochemical		
Li-ion	1.44	0.72
NiCd	0.72	0.18
NiMH	1.08	0.36
Chemical		
Gasoline	34.8	44.4
Ethanol	21.2	26.8
Natural Gas (liq)	22.2	53.6
Glucose	24.0	15.6
H2 (1 bar)	0.0029	143
H2 (700 bar)	2	143

Due to multi-step ion- and charge-transport processes, batteries have also been limited in terms of power density, that is, how fast they can discharge their stored energy.[8] Certain functions such as long-distance communication (where the coverage radius scales with the square root of power) and acceleration require high-power and not only energy density. This problem has received a lot of recent attention, leading to notable advances such as Kang and Ceder's report[13] of (macroscale) Li-ion batteries with power densities up to 25 W/cm^3. By comparison, NiMH batteries can produce about 1 W/cm^3 at a similar scale[14], fairly standard for today's commercial batteries. In addition, batteries slowly lose their charge over years, making them less ideal for long-term energy storage. Batteries with a two-year half-life will lose 31% of their charge in one year, an energy loss equivalent to 180,000 gal/yr of gasoline for the global Li-ion market as described above.

By contrast, supercapacitors (SCs) offer substantially higher power density (in weight and volume terms), but at the expense of energy density.[15-18] Their mechanisms rely on direct storage of charge by ionizing atoms/molecules on surfaces separated by a dielectric layer (like a ceramic). The newer classes of pseudocapacitors take a slightly different approach by using fast-

reacting redox species that cycle between oxidation states, rather than being simply ionized, allowing them to achieve higher energy density. Thus, typical materials for SCs have very large surface area (while still maintaining interconnection for current to flow through the circuit) and high conductivity. Activated carbon has been popular for this reason, and new SCs improve upon it with nanostructures such as nano-onions[17] or graphene.[18] However, this storage can be less stable than batteries over long periods (months to years); SCs leak charge as carriers diffuse through the dielectric to balance charge.

Energy storage in the chemical bonds of fuels dominates today's landscape, particularly for transportation. As described above, systems like engines can make use of the large enthalpies of reaction of fuels and can achieve high power through rapid reactions (sometimes with the aid of appropriate catalysts). Here the challenges for electricity generation include efficient conversion of the chemical energy, which can be limited by mechanical losses in engines, and miniaturization of many complex moving parts. Thus, engines are not presently feasible micro-scale power sources.

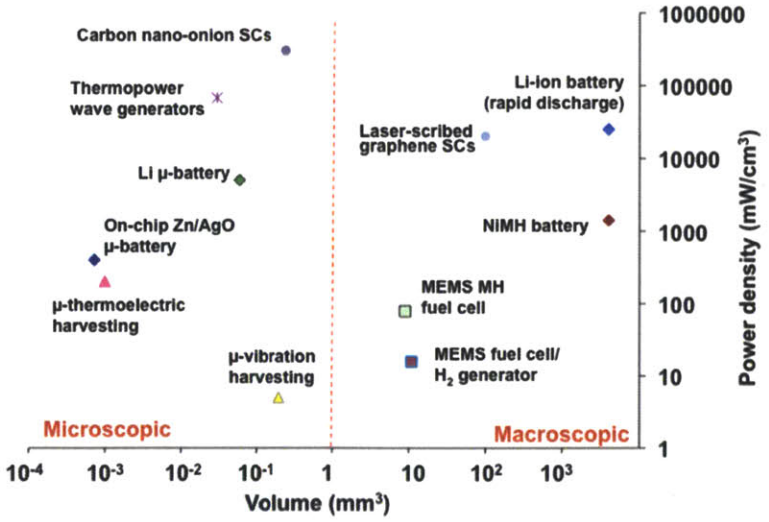

Figure 1: Volumetric power density comparison for microscale and full-scale power sources. MEMS = microelectromechanical systems; MH = metal hydride; SC = supercapacitor. Some volumes were estimated from published device descriptions; references given in text. Volumes shown are the minimum for the technologies; if connected in parallel (scaling out), they can combine their power to reach the macroscale.

Fuel cells can directly convert chemical energy to electricity with higher efficiencies than engines, and recent research has driven forward their miniaturization. [19, 20] However, power density remains limited because of difficulties with small-scale H_2 storage or reformers, which can be much larger than the fuel cell itself, not to mention preventing shorts or leak-through between very close electrodes. Figure 1 shows the power density of MEMS fuel cells, on the order of 100 mW/cm^3, in addition to other electrical technologies discussed here. Although larger fuel cells can achieve higher power density, MEMS fuel cells still fall short of microbatteries. Albano *et al.*[21] have designed an on-chip Zn/AgO battery producing about 400 $\mu W/mm^3$. Dudney *et al.*[22] have reported a somewhat larger Li microbattery with high power density up to 10 mW/mm^3.

Harvesting ambient thermal, solar, or acoustic/mechanical energy is appealing because of the small sizes of such devices and their ability to work with otherwise wasted energy.[23-29] The truly tiny footprints of these devices allow them to operate autonomously, enabling possible applications like implantable biomedical devices. For example, a 10^{-3} mm^3 thermoelectric harvester[30] can produce about 200 $\mu W/mm^3$. Energy is even available from ambient vibrations, on the order of 10 $\mu W/mm^3$. [31] However, the power generated tends to be too small for communication or acceleration, as discussed above, and remains smaller than batteries or supercapacitors. Collecting energy slowly over time then discharging it at high power would require other energy storage systems and thus would be limited by them.

1.2 The Physics of Thermoelectricity

Thermoelectric (TE) materials have a number of advantages for portable and small-scale energy system; they can be entirely solid-state, potentially eliminating the fabrication complexities and

mechanical energy losses associated with engines, turbines, and the like. Physically, thermoelectricity is defined as the direct conversion of a thermal gradient to voltage and/or current, known as the Seebeck effect, or vice versa (the Peltier effect). Thus, the ratio between voltage and temperature difference, here denoted Γ, is called the Seebeck coefficient.

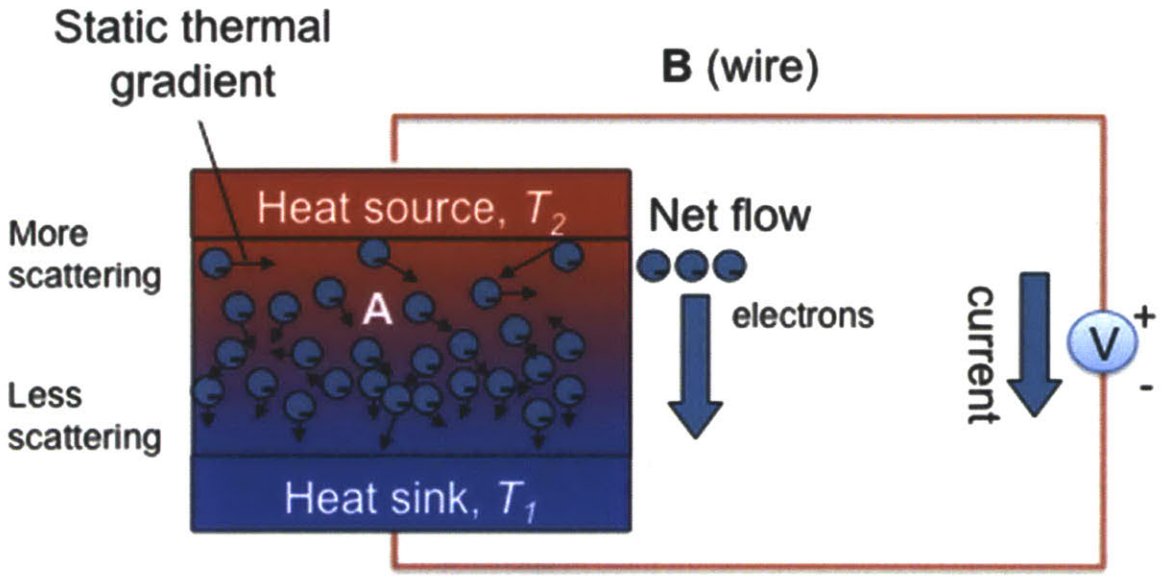

Figure 2: Schematic of conventional (diffusive) thermoelectric effect. Charge carriers (electrons in this example) scatter more on the hotter side of the thermal gradient, leading to a net flow towards the heat sink. For holes, the signs of voltage and current are opposite. Not shown in this diagram is phonon drag, where concerted motion of phonons transfers momentum to charge carriers, impelling a current. Mathematically, equations (1) and (2) describe this system.

Figure 2 illustrates the phenomenon schematically. Because their scattering rate increases with temperature, charge carriers (electrons or holes) will diffuse from the hot side of a thermal gradient to the cold side. This process is the main contributor in bulk TE materials; a second process called phonon drag will be explained later. The voltage between two points is proportional to the temperature difference, ΔT, scaled by Γ, as will be developed mathematically. The demarcation of the circuit into materials A and B is important. Because any ΔT between two points in the circuit corresponds to an opposite difference in the other direction, using only one material

in the circuit would create equal and opposite voltages that entirely cancel. TE devices must therefore contain a junction between materials with different Seebeck coefficients to generate net voltage.

Three forces can drive current: an electric field (E), a chemical potential (μ) gradient, or a temperature gradient. These forces can be combined in the charge transport equation.

$$J = -\sigma_h(E + \frac{\nabla\mu}{e}) - L_{12}\nabla T \quad (1)$$

J is current, σ is electrical conductivity, e is the elementary charge, and L_{12} is an Onsager coupling coefficient. Here properties are written in terms of holes as the majority carrier, although it is simple to write an additional equation for electrons by changing the sign before σ. When current is small enough to neglect, one can solve for E and integrate between two contacts (at positions x_L and x_R) to obtain an equation for voltage. With no differential doping across the material $\nabla\mu$ is negligible, as in most literature reference measurements, the Seebeck coefficient is $\Gamma_{\text{ref}} = \pm L_{12}/\sigma$, with the sign the opposite of the majority charge carrier.

$$V = -\int_{x_L}^{x_R} \frac{L_{12}}{\sigma_h}\nabla T \mathrm{dx} = -\int_{T_L}^{T_R} \Gamma_{ref} dT \quad (2)$$

The dimensionless figure of merit for TE materials is

$$ZT = \frac{S^2\sigma}{\chi}T \quad (3)$$

Here, χ is thermal conductivity. TE devices find applications[32] in heat pumps, refrigeration, and space exploration, where their robustness and small footprint are highly valuable. Efficiencies are proportional to ZT and are generally about 1-5%, limiting wider application.[33] Since combustion processes often create "waste" thermal gradients, researchers are interested in improving TE materials and lower their cost to take advantage of these potential energy sources. As can be seen

from the form of *ZT*, the challenge is maintaining a large thermal gradient while allowing a large electrical current to flow. In devices designed to harvest electrical power from waste heat, the goal of materials scientists has been to create materials that conduct heat primarily as phonons but block their propagation across an interface where electrical conduction is large. An example would be Bi_2Te_3/Sb_2Te_3 superlattices (243 μV/K).[34]

1.3 Thermoelectricity in Nanostructured Materials and Systems

With their unique, often tunable electrical and thermal properties, nanomaterials have been the focus of much research on increasing TE figures of merit[35]. Because of the role of χ, many efforts, such as those of the Chen group, focus on understanding heat transfer at the nanoscale.[36] The Dresselhaus group has been at the forefront of theoretical investigation of TE nanomaterials since the 1990s, when they first showed that quantum confinement could increase *ZT* by preferentially increasing phonon over electron scattering, leading to a decrease in χ. [37, 38] In bulk Bi_2Te_3, *ZT* = 0.83 at room temperature,[39] but according to this theory in 2D quantum wells the upper bound rises to 5,[39], and in 1D quantum wires (5 Å diameter) $ZT \leq 14$.[40] Later models investigated the role of crystallographic alignment, showing that Bi nanowires grown along the trigonal axis could have higher *ZT*.[41, 42] Similarly, recent experiments with SiGe nanostructures doubled the power factor ($\Gamma^2\sigma$) compared to bulk SiGe.[43] Furthermore, a p-doped core/shell structure of Ge/Si has been recently predicted to increase *ZT* to 0.85. [44]

Bismuth is often featured in TE materials due to its favorable properties, often alloyed or mixed with chalcogenides or pnictides. Poudel *et al.*[45] achieved a record *ZT* of 1.4 at 100 °C in BiSbTe bulk alloy. However, Bi nanowires have the highest Seebeck coefficient (260 μV/K),[46]

more than BiSbTe bulk alloy (220 μV/K) [45] or Bi_2Te_3 thin films (188 μV/K),[14] without having higher *ZT*.

Sb content can benefit Bi nanowires as well. Lin *et al.*[47] demonstrated that decreasing the diameter of nanowires and adding 5% Sb enhanced the Seebeck effect in $Bi_{1-x}Sb_x$ nanowires of diameter 40 nm (-64 μV/K) and 65 nm (-57 μV/K), compared to pure Bi nanowire arrays of 40 nm (-55 μV/K) and 65 nm (-48 μV/K). All these forms surpassed the Seebeck coefficient of bulk $Bi_{1-x}Sb_x$ (-45 μV/K).

Both Bi and Te face the disadvantage of low earth-abundance; accordingly they remain expensive and difficult to scale up. Te is almost the most rare (natural) element on earth, less abundant than Au or Pt.[48] Figure 3 broadens this comparison, showing the abundance of 78 elements in Earth's crust. Additionally, Bi/Te materials are often brittle, limiting the niches where they can be deployed. These concerns prompt the consideration of other materials for TE generators. Silicon is one of the principle components of Earth's crust; if formed in nanowires its *ZT* is 0.6 at 300 K, 100 times higher than bulk Si.[49] p-doping silicon nanowires[50] further increases *ZT* to 1.0 at 200 K. Other nanomaterials studied for TE applications include ZnO (-400 μV/K) [51], PbSe (193 μV/K) [52], and InSb (-220 μV/K).[53]

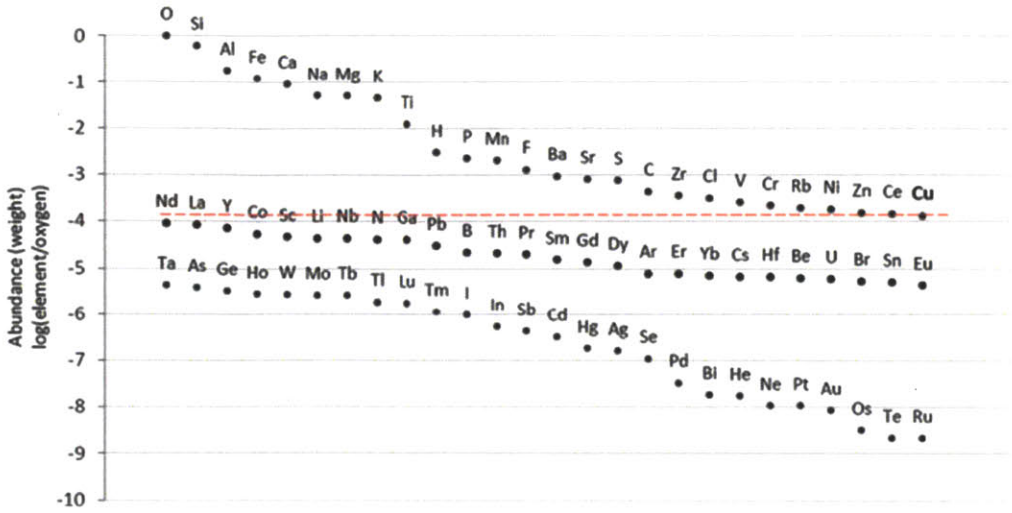

Figure 3: Abundance of elements (by mass) in Earth's crust, normalized to oxygen. Bi, Te, and Sb, all popular thermoelectric materials, are some of the rarest. Reproduced from reference [54].

1.4 Thermoelectricity in Carbon Nanotubes

Carbon, as another highly abundant element, could also play a role in widening the deployment of TE generators, especially in nanoscale forms such as nanotubes (CNTs) or graphene. Individual multiwalled CNTs (MWNTs) possess high axial room temperature thermal conductivity (3000 W/m/K)[55-57] and electrical conductivity (10,000 S/cm) [58, 59] in high aspect ratio (>100), one-dimensional structures.[60, 61] The thermal conductivity of single-walled nanotubes (SWNTs) is as much as 10,000 W/m/K, more than ten times higher than copper. This property results from their low-dimensional quantum confinement, as the movement of phonons, quantized lattice vibrations that carry heat, is restricted, decreasing the possible scattering modes that slow thermal transport. Essentially, only the presence of defects will scatter phonons at low densities. At room temperature, the Seebeck coefficient for individual MWNTs, 80 μV/K,[62] is higher than that of SWNTs, 40 μV/K.[63]

The 1D quantum confinement of CNTs leads to more complex TE effects than carrier diffusion alone. Phonon drag (known at least since the 1960s)[64] refers to a process wherein

mobile charge carriers polarize sites in the lattice as they move around, distorting phonon modes.[65] This distortion decreases carrier mobility and can thus increase *ZT*. To the extent that phonon motion is aligned (such as in quantum-confined materials with a thermal gradient), momentum transfer from phonons to charge carriers will tend to push the carriers in one direction, enhancing the TE effect. Thus, phonon drag is most influential in materials with strong electron (/hole)-phonon coupling (such as carbon nanotubes).[66, 67]

The thermoelectric properties of CNTs can change drastically when assembled into macrostructures. Hone *et al.*[68] measured the thermal conductivity of crystalline ropes of SWNTs to be only 35 W/m/K at room temperature. They found that the thermal conductivity is dominated by phonons at all temperatures with a mean free path on the order of 1 μm. Hewitt *et al.* prepared SWNT films with varying amounts of polyvinylidene fluoride (PVDF); the pure SWNT films had Γ = 20 μV/K at 300 K, which exhibited temperature-dependence characteristic of mixtures of metals and semiconductors.[69] Some PVDF content could increase *ZT* 100-fold but did not appreciably change Γ. Nevertheless, this increase puts SWNT composites on par with conjugated polymers (*ZT* ~ 10^{-3}),[70, 71] although the *ZT* of pure CNTs is quite low (~10^{-4}).[72]

While these measurements were in the temperature range of 10 K to 300 K, Zhang *et al.*[73] measured thermopower in sintered MWNT mats up to 958 K. Even though the Seebeck coefficients of all types of nanotubes are higher than graphite, MWNT mats demonstrated relatively lower Seebeck coefficients (10 μV/K) than individual MWNT and SWNT due to the low concentrations of charge carriers that can freely move in bulk materials. Junctions between tubes and void spaces often hinder mobility.

Covalent bonding to the sidewalls or physisorption of molecules to CNTs can change their electronic properties through doping, another way to enhance TE effects.[74-77] Adsorption of O_2

makes conduction in SWNTs p-type under ambient conditions, but its removal will switch conduction (and therefore the sign of the Seebeck coefficient) to n-type.[78, 79] Sumanasekera *et al.* found that de-doped SWNTs had Γ = -44 μV/K, compared to 65 μV/K under ambient conditions.[79] On the other hand, potassium doping decreased average Γ of a suspended film of nitric-acid-purified SWNTs near room temperature from 32 to 16 μV/K.[80] Thus, doping has not been found to increase the magnitude of the Seebeck coefficient.

Due to their strength and flexibility, CNTs have been included as fillers in composite materials, often with polymers, offering a vision of TE-generating fabrics and conformal devices. The Seebeck coefficient of a CNT sheet coated with polyaniline (0.3 – 0.5 mm thick) is remarkably higher (22 μV/K) than both bulk parent samples[81] (12 μV/K for CNTs, 3 μV/K for polyaniline). Van *et al.*[82] integrated a CNT/Au junction into a micro-thermocouple but did not find any difference in Seebeck coefficient or TE performance. Thus, the TE properties of CNTs lag significantly behind inorganic nanowires despite these efforts. The simultaneously high phonon and electron conductivities in CNTs limit their use in conventional TE applications.

References

1. Doo-hyong, H. *Obama attends groundbreaking of LG-affiliated battery factory*. Yonhap News, 2010.
2. See, K., A. Wirshba, and M. Holman, *Using Partnerships to Stay Afloat in the Electric Vehicle Storm*, in *Lux Research State of the Market*, I. Lux Research, Editor 2011, Lux Research, Inc.
3. Cook-Chennault, K.A., N. Thambi, and A.M. Sastry, *Powering MEMS portable devices - a review of non-regenerative and regenerative power supply systems with special emphasis on piezoelectric energy harvesting systems.* Smart Materials & Structures, 2008. **17**(4).
4. Kerzenmacher, S., et al., *Energy harvesting by implantable abiotically catalyzed glucose fuel cells.* Journal of Power Sources, 2008. **182**(1): p. 1-17.
5. Yager, P., et al., *Microfluidic diagnostic technologies for global public health.* Nature, 2006. **442**(7101): p. 412-418.

6. Cook, B.W., S. Lanzisera, and K.S.J. Pister, *SoC issues for RF smart dust.* Proceedings of the IEEE, 2006. **94**(6): p. 1177-1196.
7. Sailor, M.J. and J.R. Link, *"Smart dust": nanostructured devices in a grain of sand.* Chemical Communications, 2005(11): p. 1375-1383.
8. Armand, M. and J.-M. Tarascon, *Building better batteries.* Nature, 2008. **451**: p. 652-657.
9. Thomas, G., *Overview of Storage Development DOE Hydrogen Program*, 2000, Sandia National Laboratories: Livermore, CA.
10. Tarascon, J.-M. and M. Armand, *Issues and challenges facing rechargeable lithium batteries.* Nature, 2001. **414**: p. 359-367.
11. Lide, D.R., ed. *CRC Handbook of Chemistry and Physics*. 92 ed. 2012, CRC Press: Boca Raton.
12. *National Hydrogen Energy Roadmap*, 2002, Department of Energy: Washington, DC.
13. Kang, B. and G. Ceder, *Battery materials for ultrafast charging and discharging.* Nature, 2009. **458**(7235): p. 190-193.
14. Kuriyama, N., et al., *Hydrogen storage alloys for nickel/metal-hydride battery.* Vacuum, 1996. **47**(6-8): p. 889-892.
15. Hulicova-Jurcakova, D., et al., *Nitrogen-Enriched Nonporous Carbon Electrodes with Extraordinary Supercapacitance.* Advanced Functional Materials, 2009. **19**(11): p. 1800-1809.
16. Lee, J.A., et al., *Hybrid Nanomembranes for High Power and High Energy Density Supercapacitors and Their Yarn Application.* ACS Nano, 2011. **6**(1): p. 327-334.
17. Pech, D., et al., *Ultrahigh-power micrometre-sized supercapacitors based on onion-like carbon.* Nat Nano, 2010. **5**(9): p. 651-654.
18. El-Kady, M.F., et al., *Laser Scribing of High-Performance and Flexible Graphene-Based Electrochemical Capacitors.* Science, 2012. **335**(6074): p. 1326-1330.
19. Moghaddam, S., et al., *A self-regulating hydrogen generator for micro fuel cells.* Journal of Power Sources, 2008. **185**(1): p. 445-450.
20. Zhu, L., et al., *Integrated micro-power source based on a micro-silicon fuel cell and a micro electromechanical system hydrogen generator.* Journal of Power Sources, 2008. **185**(2): p. 1305-1310.
21. Albano, F., et al., *A fully integrated microbattery for an implantable microelectromechanical system.* Journal of Power Sources, 2008. **185**(2): p. 1524-1532.
22. Dudney, N.J., *Solid-state thin-film rechargeable batteries.* Materials Science and Engineering B-Solid State Materials for Advanced Technology, 2005. **116**(3): p. 245-249.
23. Qin, Y., X.D. Wang, and Z.L. Wang, *Microfibre-nanowire hybrid structure for energy scavenging.* Nature, 2008. **451**(7180): p. 809-813.
24. Song, J.H., J. Zhou, and Z.L. Wang, *Piezoelectric and semiconducting coupled power generating process of a single ZnO belt/wire. A technology for harvesting electricity from the environment.* Nano Letters, 2006. **6**(8): p. 1656-1662.
25. Mor, G.K., et al., *A review on highly ordered, vertically oriented TiO2 nanotube arrays: Fabrication, material properties, and solar energy applications.* Solar Energy Materials and Solar Cells, 2006. **90**(14): p. 2011-2075.
26. Shao, Z.P., et al., *A thermally self-sustained micro solid-oxide fuel-cell stack with high power density.* Nature, 2005. **435**(7043): p. 795-798.
27. Strasser, M., et al., *Micromachined CMOS thermoelectric generators as on-chip power supply.* Sensors and Actuators a-Physical, 2004. **114**(2-3): p. 362-370.

28. Mitcheson, P.D., et al., *Energy harvesting from human and machine motion for wireless electronic devices.* Proceedings of the Ieee, 2008. **96**(9): p. 1457-1486.
29. Arnold, D.P., *Review of microscale magnetic power generation.* IEEE Transactions on Magnetics, 2007. **43**(11): p. 3940-3951.
30. Watkins, C., B. Shen, and R. Venkatasubramanian, *Low-grade-heat energy harvesting using superlattice thermoelectrics for applications in implantable medical devices and sensors.* ICT: 2005 24th International Conference on Thermoelectrics, 2005: p. 250-252
533.
31. Jeon, Y.B., et al., *MEMS power generator with transverse mode thin film PZT.* Sensors and Actuators a-Physical, 2005. **122**(1): p. 16-22.
32. Riffat, S.B. and X.L. Ma, *Thermoelectrics: a review of present and potential applications.* Applied Thermal Engineering, 2003. **23**(8): p. 913-935.
33. DiSalvo, F.J., *Thermoelectric cooling and power generation.* Science, 1999. **285**(5428): p. 703-706.
34. Venkatasubramanian, R., et al., *Thin-film thermoelectric devices with high room-temperature figures of merit.* Nature, 2001. **413**(6856): p. 597-602.
35. Chen, G., et al., *Recent developments in thermoelectric materials.* International Materials Reviews, 2003. **48**(1): p. 45-66.
36. Chen, G., *Nanoscale heat transfer and nanostructured thermoelectrics.* Ieee Transactions on Components and Packaging Technologies, 2006. **29**(2): p. 238-246.
37. Dresselhaus, M.S., et al., *Low-dimensional thermoelectric materials.* Physics of the Solid State, 1999. **41**(5): p. 679-682.
38. Dresselhaus, M.S., et al., *Quantum wells and quantum wires for potential thermoelectric applications.* Recent Trends in Thermoelectric Materials Research Iii, 2001. **71**: p. 1-121.
39. Hicks, L.D. and M.S. Dresselhaus, *Effect of Quantum-Well Structures on the Thermoelectric Figure of Merit.* Physical Review B, 1993. **47**(19): p. 12727-12731.
40. Hicks, L.D. and M.S. Dresselhaus, *Thermoelectric Figure of Merit of a One-Dimensional Conductor.* Physical Review B, 1993. **47**(24): p. 16631-16634.
41. Lin, Y.M., X.Z. Sun, and M.S. Dresselhaus, *Theoretical investigation of thermoelectric transport properties of cylindrical Bi nanowires.* Physical Review B, 2000. **62**(7): p. 4610-4623.
42. Sun, X., Z. Zhang, and M.S. Dresselhaus, *Theoretical modeling of thermoelectricity in Bi nanowires.* Applied Physics Letters, 1999. **74**(26): p. 4005-4007.
43. Dresselhaus, M.S., et al., *New directions for low-dimensional thermoelectric materials.* Advanced Materials, 2007. **19**(8): p. 1043-1053.
44. Chen, X., Y.C. Wang, and Y.M. Ma, *High Thermoelectric Performance of Ge/Si Core-Shell Nanowires: First-Principles Prediction.* Journal of Physical Chemistry C, 2010. **114**(19): p. 9096-9100.
45. Poudel, B., et al., *High-thermoelectric performance of nanostructured bismuth antimony telluride bulk alloys.* Science, 2008. **320**(5876): p. 634-638.
46. Zhou, J.H., et al., *Thermoelectric properties of individual electrodeposited bismuth telluride nanowires.* Applied Physics Letters, 2005. **87**(13): p. -.
47. Lin, Y.M., et al., *Semimetal-semiconductor transition in Bi1-xSbx alloy nanowires and their thermoelectric properties.* Applied Physics Letters, 2002. **81**(13): p. 2403-2405.
48. Alharbi, F., et al., *Abundant non-toxic materials for thin film solar cells: Alternative to conventional materials.* Renewable Energy, 2011. **36**(10): p. 2753-2758.

49. Hochbaum, A.I., et al., *Enhanced thermoelectric performance of rough silicon nanowires.* Nature, 2008. **451**(7175): p. 163-U5.
50. Boukai, A.I., et al., *Silicon nanowires as efficient thermoelectric materials.* Nature, 2008. **451**(7175): p. 168-171.
51. Lee, C.H., et al., *Thermoelectric power measurements of wide band gap semiconducting nanowires.* Applied Physics Letters, 2009. **94**(2): p. -.
52. Liang, W.J., et al., *Field-Effect Modulation of Seebeck Coefficient in Single PbSe Nanowires.* Nano Letters, 2009. **9**(4): p. 1689-1693.
53. Uryupin, O.N., et al., *Thermoelectric Properties of InSb Nanowires Over a Wide Temperature Range.* Journal of Electronic Materials, 2009. **38**(7): p. 990-993.
54. Alharbi, F., et al., *Abundant non-toxic materials for thin film solar cells: Alternative to conventional materials.* Renewable Energy, 2011. **36**: p. 2753-2758.
55. Yu, C.H., et al., *Thermal conductance and thermopower of an individual single-wall carbon nanotube.* Nano Letters, 2005. **5**(9): p. 1842-1846.
56. Adu, C.K.W., et al., *Carbon nanotubes: A thermoelectric nano-nose.* Chemical Physics Letters, 2001. **337**(1-3): p. 31-35.
57. Sumanasekera, G.U., et al., *Giant thermopower effects from molecular physisorption on carbon nanotubes.* Physical Review Letters, 2002. **89**(16): p. -.
58. Ebbesen, T.W., et al., *Electrical conductivity of individual carbon nanotubes.* Nature, 1996. **382**(6586): p. 54-56.
59. Ando, Y., et al., *Physical properties of multiwalled carbon nanotubes.* International Journal of Inorganic Materials, 1999. **1**(1): p. 77-82.
60. Cahill, D.G., et al., *Nanoscale thermal transport.* Journal of Applied Physics, 2003. **93**(2): p. 793-818.
61. Fisher, T.S. and D.G. Walker, *Thermal and electrical energy transport and conversion in nanoscale electron field emission processes.* Journal of Heat Transfer-Transactions of the Asme, 2002. **124**(5): p. 954-962.
62. Kim, P., et al., *Thermal transport measurements of individual multiwalled nanotubes.* Physical Review Letters, 2001. **8721**(21): p. 215502-215505.
63. Yu, C.H., et al., *Thermal conductance and thermopower of an individual single-wall carbon nanotube.* Nano Lett., 2005. **5**(9): p. 1842-1846.
64. Hutson, A.R., *Piezoelectric Scattering and Phonon Drag in ZnO and CdS.* Journal of Applied Physics, 1961. **32**(10): p. 2287 - 2292.
65. Kittel, C., *Introduction to Solid State Physics*. 7 ed1996: John Wiley and Sons.
66. Tsaousidou, M., *Theory of phonon-drag thermopower of extrinsic semiconducting single-wall carbon nanotubes and comparison with previous experimental data.* Phys. Rev. B, 2010. **81**(23).
67. Pop, E., et al., *Negative differential conductance and hot phonons in suspended nanotube molecular wires.* Physical Review Letters, 2005. **95**(15): p. 155505-155508.
68. Hone, J., et al., *Thermoelectric power of single-walled carbon nanotubes.* Physical Review Letters, 1998. **80**(5): p. 1042-1045.
69. Hewitt, C.A., et al., *Varying the concentration of single walled carbon nanotubes in thin film polymer composites, and its effect on thermoelectric power.* Applied Physics Letters, 2011. **98**(18): p. 183110-3.
70. Levesque, I., et al., *Highly Soluble Poly(2,7-carbazolenevinylene) for Thermoelectrical Applications: From Theory to Experiment.* React. Funct. Polym., 2005. **65**: p. 23-36.

71. Yan, H., N. Sada, and N. Toshima, *Thermal Transporting Properties of Electrically Conductive Polyaniline Films as Organic Thermoelectric Materials.* J. Therm. Anal. Calorim., 2002. **69**: p. 881-887.
72. Zhan, G.D., et al., *Thermoelectric properties of carbon nanotube/ceramic nanocomposites.* Scripta Materialia, 2006. **54**(1): p. 77-82.
73. Zhang, H.L., et al., *Electrical and thermal properties of carbon nanotube bulk materials: Experimental studies for the 328-958 K temperature range.* Physical Review B, 2007. **75**(20): p. -.
74. Choi, Y.M., et al., *Nonlinear behavior in the thermopower of doped carbon nanotubes due to strong, localized states.* Nano Letters, 2003. **3**(6): p. 839-842.
75. Vavro, J., et al., *Thermoelectric power of p-doped single-wall carbon nanotubes and the role of phonon drag.* Physical Review Letters, 2003. **90**(6): p. -.
76. Sadanadan, B., et al., *Synthesis and thermoelectric power of nitrogen-doped carbon nanotubes.* Journal of Nanoscience and Nanotechnology, 2003. **3**(1-2): p. 99-103.
77. Sumanasekera, G.U., et al., *Giant thermopower effects from molecular physisorption on carbon nanotubes.* Physical Review Letters, 2002. **89**(16): p. 166801.
78. Bradley, K., et al., *Is the Intrinsic Thermoelectric Power of Carbon Nanotubes Positive?* Physical Review Letters, 2000. **85**: p. 4361-4364.
79. Sumanasekera, G.U., et al., *Effects of Gas Adsorption and Collisions on Electrical Transport in Single-Walled Carbon Nanotubes.* Physical Review Letters, 2000. **85**(1096-1099).
80. St-Antoine, B.C., D. Ménard, and R. Martel, *Single-Walled Carbon Nanotube Thermopile For Broadband Light Detection.* Nano Letters, 2010. **11**: p. 609-613.
81. Meng, C.Z., C.H. Liu, and S.S. Fan, *A Promising Approach to Enhanced Thermoelectric Properties Using Carbon Nanotube Networks.* Advanced Materials, 2010. **22**(4): p. 535-+.
82. Van, T.D., et al., *Integration of SWNT film into MEMS for a micro-thermoelectric device.* Smart Materials & Structures, 2010. **19**(7): p. -.

Chapter 2

Modeling increased anisotropic oxidation rates in metal nanoparticles around carbon nanotube thermal conduits: the role of interfacial thermal conductance

2.1: Previous research on nano-structured energetic materials and applications

Nano-structured energetic materials, such as nanothermites, have attracted attention because of new observations of reaction front velocity enhancements compared to energetic materials with microscale structure [1-8]. We define reaction front velocity, sometimes called combustion or flame velocity, as the velocity at which the border between un-reacted and reacting regions moves through a material. It is a simple, but important metric for understanding not just the speed, but also the combustion regime of energetic reactions. For example, if the reaction front velocity is greater than the acoustic velocity in an energetic material, it can detonate instead of deflagrating [9].

Experimentally measured increases in reaction front velocity in nanothermites vary widely, depending on particle size, materials, and sample geometry. Aumann *et al.* noted that 20 – 50 nm particles of Al and MoO_3 can react up to one thousand times faster than conventional powder sizes [3]. Bockmann *et al.* reported for the Al/MoO_3 system that as Al particle diameter decreases, even just from 121 nm to 75 nm, velocity increased from 750 to 950 m/s [4]. However, Granier and Pantoya observed that while ignition time does decrease by a factor of several hundred when particle size decreases from the microscale to the nanoscale,

the burn rate was still the highest for 10 to 14 μm Al particles (30 m/s) compared to at most 11 m/s for 53 nm Al particles [6]. They attributed this to the very dense packing of the nanoparticles, leading to oxygen supply problems. Plantier and colleagues found that, depending on how the fuel and oxidizer were synthesised and mixed, reaction speeds in the Al/Fe_2O_3 system could vary from 10 to 900 m/s [5]. These faster reaction front velocities make Al-based nanothermites a popular choice for studies of nanoscale combustion, compared to slower burning materials like Zr, for which studies tend to focus on the microscale [10-13].

Initially, the fast reaction rates of nanothermites were attributed to the very high surface area-to-volume ratio of nanoparticles, which greatly decreases mass transport limitations on reaction rate, and more homogeneous distribution of fuel and oxidizer [2, 3, 8]. However, the diffusion-limited model does not always adequately explain combustion. For example, reaction front velocity is independent of particle diameter below 80 nm [6]. Levitas *et al.* proposed that a different, faster combustion mechanism could be taking place in nanoscale Al combustion [14]. In the melt dispersion mechanism (MDM), the metal core of a spherical Al particle melts before the surrounding Al_2O_3 shell. If the particle is small enough, the shell can be nearly free of defects and thus very strong, allowing pressure to build up in the core as the Al expands. When the shell finally breaks, the unloading pressure wave disperses small Al clusters at high velocity, sparking further reactions and promoting rapid oxidation of the aluminum atoms.

Another characteristic of some nano-structured energetic materials that has received less attention is anisotropy. For example, single crystals of pentaerythritol tetranitrate (PETN) have different times and distances from shock to detonation depending upon which orientation is shocked [7]. Jindal and Dlott also modeled shock wave initiation in naphthalene, which exhibits some directional dependence [15]. By contrast, anisotropy has been studied very little

for nanothermite systems since their component particles are spherical and do not exhibit the directional properties characteristic of crystal lattices.

Previous studies such as those mentioned above tended to focus on anisotropy in the initiation of a detonation wave, which would then spread in three dimensions. However, a material that released energy selectively in one dimension would enable a number of interesting applications. For example, energy could be focused at the nanoscale in the solid state, creating an environment analogous to collapsing ultrasonic bubbles in the liquid phase, which achieve very high energy densities. Ultrasonic processing is used ubiquitously in the preparation of colloidal dispersions [16], materials synthesis [17], and sonochemistry [17, 18]. Also, the extreme conditions of detonation have been shown to simplify otherwise difficult syntheses (e.g. detonation nanodiamonds [19]). A 1-D energetic release would enable more precise synthesis of such materials with more control over geometry. It is possible that 1-D energetic systems could be used as propellant in pulse detonation engines [20], which offer higher thermodynamic efficiencies (even at subsonic velocities) than conventional combustion engines in airplanes and rockets. A 1-D detonating fuel additive would be ideal for pulse detonation engines, since almost all of the thrust could be directed backwards if the propellant were aligned with the nozzle and initiated at the end farthest from the nozzle. Moreover, a nanostructured propellant could offer precise control of the fuel/oxidizer ratio and mixing by controlling the placement of nanoparticles during synthesis.

Towards these ends, this chapter considers the concept of an anisotropic nanothermite where a single-walled carbon nanotube, thermally coupled to a metal oxidation reaction, accelerates the reaction front velocity only along the nanotube axis. Defect-free single-walled carbon nanotubes (SWNTs) can possess high thermal conductivity. Simulations predict exceptionally high values, between 1500 and 6600 W/m/K for room temperature single-walled

nanotubes [21, 22], while experimental measurements have produced values anywhere from 300 to at least 3000 W/m/K for multi-walled carbon nanotubes, depending on diameter, length, and the density of defects [23-27]. Room temperature thermal conductivity has been measured as at least 200 W/m/K for bundles of SWNTs [28, 29] and 2500 to 10000 W/m/K for individual SWNT, depending inversely on diameter [30, 31]. This work explores values bracketed by these studies: 300 to 11000 W/m/K. For this study we chose zirconium as the metal because its relatively slow reaction rate offers potential for significant enhancement by the addition of SWNTs, and its reaction parameters are readily available in the literature.

The effectiveness of a 1-D thermal conductor such as a SWNT towards increasing reaction front velocities in combusting metal nanoparticle systems depends upon several variables: the interfacial thermal conductance between the metal and the nanotube, G, the nanotube thermal conductivity, k_{SWNT}, and the geometry of both phases. A faster mode of heat transfer through the nanotube promotes the chemical reaction in metal nanoparticles ahead of the reaction front by providing thermal energy to overcome the thermal activation energy barrier towards oxidation, thereby increasing the reaction velocity considerably. Our interest is in calculating the magnitude of this enhancement. The role of the interfacial thermal conductance, previously shown to limit thermal applications of SWNTs, is shown to not present a substantial barrier to this application due to the non-linear nature of the coupling heat transfer equations.

2.2. Case I: Heat Conduction in Nanotube Alone

We first consider a single nanotube of length L not thermally coupled to any other system. For SWNTs with few defects, heat conduction will likely be ballistic. In this case we can describe the movement of phonons using the Boltzmann transport equation.

$$\frac{\partial f}{\partial t} + \mathbf{v} \cdot \nabla_{\mathbf{r}} f + \frac{\partial \mathbf{v}}{\partial t} \cdot \nabla_{\mathbf{v}} f = \left.\frac{\partial f}{\partial t}\right|_{coll} \quad (1)$$

Here f is the distribution function of phonons in three-dimensional Cartesian space, **r**. **v** is the velocity space corresponding to **r**, t is time, and $(\partial f/\partial t)|_{coll}$ describes the change in phonon distribution due to collisions. Diffusive Fourier heat conduction is derived from equation (1) when the number of collisions is large. It is unclear to what extent covering a nanotube with a reactive metal shell, as we will model in Case II, increases phonon scattering. At low temperature, transport in the defective, functionalized nanotube is likely diffusive. But upon heating from the exothermic reaction, homolytic cleavage of any bonds between the SWNT and the reacting layer will eliminate defects, returning the SWNT conductivity to a quasi-ballistic regime. Thus, fully modeling equation (1) (e.g. with Monte Carlo simulation) would be very difficult, as scattering rates and relaxation times would be unknown. Also, the system transitions between diffusive and ballistic regimes with coupling to chemical reaction. Therefore, we will approximate heat conduction as always diffusive in both cases for consistency.

The energy balance for the nanotube is

$$\frac{\partial T_2}{\partial t} = \frac{\partial}{\partial x}\left(\alpha_2 \frac{\partial T_2}{\partial x}\right) \quad (2)$$

where α_2 is the thermal diffusivity, T_2 is the temperature at a certain instant and position, t is time, and x is the distance coordinate. We define boundary conditions by supposing the SWNT is instantly heated (e.g. by a laser) to 1000 K at its right end at t = 0. That temperature is maintained throughout the simulation. The rest of the SWNT starts out at 298 K. These boundary conditions can also be stated as

$t \geq 0$, $x = L$ $T = T_{2,e} = 1000$ K

$t = 0$, $x < L$ $T = 298$ K

Equation (2) has a well-known analytical solution by separation of variables:

$$T_2 = A_1 + A_2 e^{-c^2 t\alpha_2}\left(A_3 \sin(cx) + A_4 \cos(cx)\right) \tag{3}$$

We solve for A_1, A_2, A_3, and A_4 to get equation (4) by applying the boundary conditions to the uncoupled nanotube case

$$T_2 = T_{2,e} + \sum_{n=0}^{\infty}\left(\frac{2}{L}\int_0^L \left(T_{2,i} - T_{2,e}\right)\cos\left(\frac{n\pi x}{2L}\right)dx\right) e^{-t\left(\frac{n\pi x}{2L\alpha_2}\right)^2}\left(\cos\left(\frac{n\pi x}{2L}\right)\right) \tag{4}$$

We model thermal conduction in a 10-μm long nanotube for two limiting cases of thermal conductivity: 300 [23] and 6600 W/m/K [22]. This frames the problem and provides an estimate of what degree of enhancement is possible.

The evolution of the temperature profile along the length of the nanotube is shown in Figure 1. In both cases the shape of the temperature profile development is very similar, but the time scale for Figure 1b is shorter by a factor of 220, corresponding to the ratio of the two thermal conductivities. The reason for this is that $\frac{\partial T_2}{\partial t}$ depends linearly on α_2 if we assume thermal diffusivity is constant. While the nanotube cannot be considered to be one constant temperature for reaction front velocities of 100 m/s and higher for k_{SWNT} = 300 W/m/K, this is a reasonable approximation for k_{SWNT} = 6600 W/m/K. Even for u = 1000 m/s, the temperature difference between the two ends of the nanotube is only about 125 K.

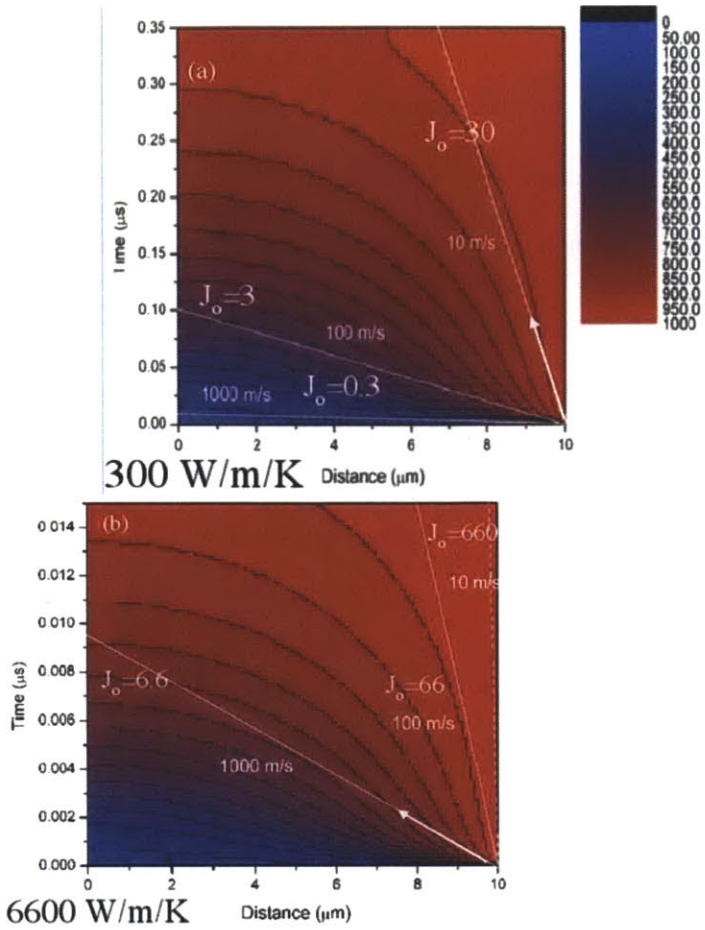

Figure 1. Thermal profiles of nanotubes at limiting values of thermal conductivity. Black lines are isotherms; white lines are profiles of an uncoupled SWNT parallel to a reaction wave travelling at a certain velocity. The ratio of heat to reaction "velocities," J_o, is also included with each line.

In addition, the nonlinear nature of thermal diffusion in the nanotube means that the temperature profile with respect to a constant velocity reaction front generally does not decrease monotonically. The temperature of the nanotube may decrease initially, but tends to increase again as the reaction front reaches the end of the nanotube.

We can define a dimensionless number J_o to compare reaction front velocity and "heat velocity" in the nanotube in a simple fashion. J_o is the ratio of the "velocity" of heat conduction based on thermal diffusivity, α/L, to the speed of the reaction front, u. The parameter L is a

characteristic length of the system; since heat transport is controlled by phonons in SWNTs at all temperatures, we use 1 μm, an average phonon mean free path [32, 33]. Based on Figure 1, we define three regimes of coupled heat conduction and reaction. For J_o less than 1, the nanotube is not at a uniform temperature during the reaction time scale. The heat conducted in the SWNT contributes only modestly to the reaction. A value of J_o between 1 and 15 represents a transition regime in which SWNT temperature is still not uniform, but SWNT heat conduction plays a larger role in the energy transport of the system. If J_o is greater than 15, SWNT temperature is essentially uniform during the reaction time scale and controls the progress of the reaction along the length of the SWNT.

Thus, to gain the greatest benefits from including SWNTs in the system, reaction front velocity should be no more than 20 m/s (for the 300 W/m/K case) or no more than 400 m/s (for the 6600 W/m/K case). Since 400 m/s is significantly less than the speed of sound in energetic materials, it seems unlikely that adding SWNTs, even with the best thermal properties, will increase reaction front velocity sufficiently to make a deflagration-to-detonation transition possible.

2.3. Case II: Conduction and Reaction in Nanotube with Metal Annulus

Next we consider a cylinder composed of a mixture of metal and metal oxide. A continuous native oxide layer surrounds the cylinder, as in Figure 2. Our model will overestimate reaction rate in both the cylinder and the annulus since it assumes a lack of voids in the material. In reality, the cylinder would be composed of imperfectly packed spherical particles, for example.

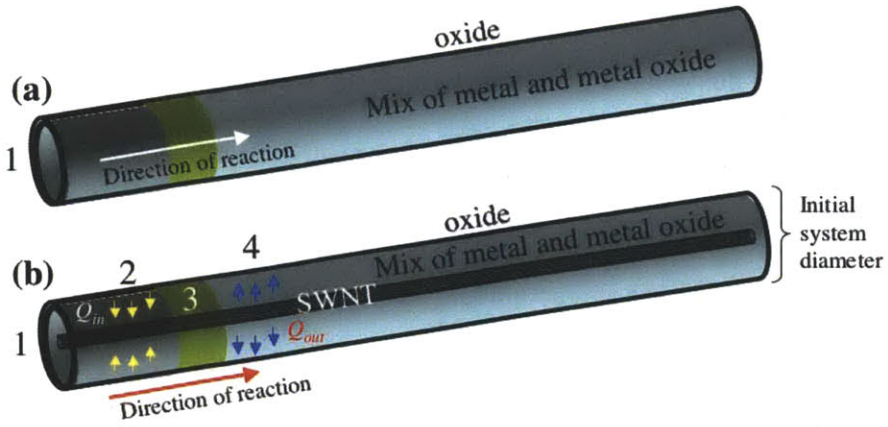

Figure 2. Conceptual design of an anisotropic nanothermite based upon a metal nanoparticle-SWNT model system. The nanoparticle phase was first modeled as a continuous cylinder with no radial variances (a); later models had the cylinder surrounding a nanotube (b). In both cases, reaction is arbitrarily initiated at the left end of the system (1). In (b), behind (2) and in the reaction front (3) the evolved heat is transferred (Q_{in}) into the thermally coupled SWNT which may then rapidly conduct along the length, potentially accelerating the energetic release from un-reacted material (4) only in this direction.

The one-dimensional energy balance equation for this system involves conduction and reaction terms, and is given by

$$\frac{\partial T_1}{\partial t} = \frac{\partial}{\partial x}\left(\alpha_1 \frac{\partial T_1}{\partial x}\right) - \frac{Q}{\rho_1 C_{p,1}} \frac{\partial \eta}{\partial t} \tag{5}$$

where Q is the enthalpy of combustion for the metal, $C_{p,1}$ is the specific heat, ρ_1 is the density, and η is the extent of reaction (as measured in units of concentration). The thickness of the outer oxide shell is calculated as a fraction of the total diameter of the cylinder and affects the equation through the kinetics term, $\frac{\partial \eta}{\partial t}$. We ignore convection and temperature dependencies

of the heat capacities or thermal conductivities. The Stefan-Boltzmann law dramatically overestimates radiation flux when the emitting particle size is smaller than the wavelength of the radiation and is therefore neglected [34]. While the magnitude of reaction rate may be incorrect, the terms are neglected for both coupled and uncoupled systems. The effect of these assumptions on the *enhancement* of reaction rate will be minimal, provided thermal conduction in the solid is the dominant heat transfer mode.

The model also neglects phase changes in the metallic cylinder, although temperatures could be high enough to melt both the metal and the oxide. Thus, in the interest of simplicity, the model does not simulate the melt dispersion mechanism (MDM) of nanoparticle combustion [14], in which the inner cores of the nanoparticles are liquid at points in the reaction. The MDM cannot work if the oxide shells on the nanoparticles are incomplete or cracked; in these cases our simplified model is applicable. The enthalpy of phase change is accounted for in the energy balance by fitting liquid and solid phase data about enthalpy of combustion and heat capacities of metal and oxide in one averaged expression [10].

The purpose of enclosing a single-walled carbon nanotube within this metallic cylinder is to enhance the propagation of the heat released along the axial dimension, due to the significantly higher thermal conductivity of the nanotube. The coupling between the nanotube and the metal leads to mutual heat transfer, the rate of which depends on the interfacial conductance, *G*. We begin with the full, coupled energy balance for the annulus of energetic material.

$$V_1 \frac{\partial(\rho_1 C_{p,1} T_1)}{\partial t} = V_1 \frac{\partial}{\partial x}\left(k_1 \frac{\partial T_1}{\partial x}\right) - V_1 \frac{\partial(Q\eta)}{\partial t} - GA(T_1 - T_2) \qquad (6)$$

k_1 is the thermal conductivity of the energetic material, V_1 is the volume of the annulus (assumed to be constant), and A is the contact area between the nanotube and the annulus. Assuming ρ, C_p, and Q are constant, we can bring them outside of the derivatives and divide

$$V_1 \frac{\partial T_1}{\partial t} = V_1 \frac{\partial}{\partial x}\left(\alpha_1 \frac{\partial T_1}{\partial x}\right) - \frac{QV_1}{\rho_1 C_{p,1}} \frac{\partial \eta}{\partial t} - \frac{GA}{\rho_1 C_{p,1}}(T_1 - T_2) \tag{7}$$

At this point we divide by V_1.

$$\frac{\partial T_1}{\partial t} = \frac{\partial}{\partial x}\left(\alpha_1 \frac{\partial T_1}{\partial x}\right) - \frac{Q}{\rho_1 C_{p,1}} \frac{\partial \eta}{\partial t} - \frac{G(\pi d_N L)}{\rho_1 C_{p,1}(\pi d_M^2 - \pi d_N^2)L}(T_1 - T_2) \tag{8}$$

d_N is very small compared to d_M, so the last term is simplified to

$$\frac{\partial T_1}{\partial t} = \frac{\partial}{\partial x}\left(\alpha_1 \frac{\partial T_1}{\partial x}\right) - \frac{Q}{\rho_1 C_{p,1}} \frac{\partial \eta}{\partial t} - \frac{G}{\rho_1 C_{p,1}}(T_1 - T_2)\frac{d_N}{d_M^2} \tag{9}$$

The derivation for the nanotube energy balance is very similar, only lacking the reaction term.

$$\frac{\partial T_2}{\partial t} = \frac{\partial}{\partial x}\left(\alpha_2 \frac{\partial T_2}{\partial x}\right) + \frac{G(\pi d_N L)}{\rho_2 C_{p,2}(\pi d_N^2)L}(T_1 - T_2) = \frac{\partial}{\partial x}\left(\alpha_2 \frac{\partial T_2}{\partial x}\right) + \frac{G}{\rho_2 C_{p,2}}(T_1 - T_2)\frac{1}{d_N} \tag{10}$$

The equations neglect phase changes as well as combustion reactions in the nanotube; not enough data exist to create averaged expressions for SWNTs. However, the SWNT will only evaporate or combust behind the reaction front (if anywhere), as the material that the front has not yet passed will not be hot enough. Since the velocity of the reaction front is of primary concern for this model, what happens in the system after the front passes is not as important. Moreover, the SWNT may survive the traveling reaction wave if the wave speed is large relative to reaction rate.

The coupled system of partial differential equations is solved using the Crank-Nicolson method and the MATLAB software package. For each time step, the reaction front is defined as the point where the reaction rate is at a maximum, and the velocity is calculated accordingly.

For this study, all metal and oxide parameter values, as well as boundary conditions, are based on Arimondi *et al.*'s earlier work modeling Zr combustion in one dimension [10]. Ewald *et al.* later expanded this simulation to a two-dimensional model [11], but we restrict our system to one dimension based on the geometry of the Zr/SWNT system. Since Zr is a relatively slow combusting material, we hypothesized it would have significant potential for reaction velocity enhancement by the addition of SWNTs. Moreover, our MATLAB model, reproduces Arimondi *et al.*'s results for an uncoupled Zr cylinder, shown in Figure 3, demonstrating the model's validity before use on the coupled Zr/SWNT system. With this groundwork laid, future studies will be able to focus on faster reacting materials of interest.

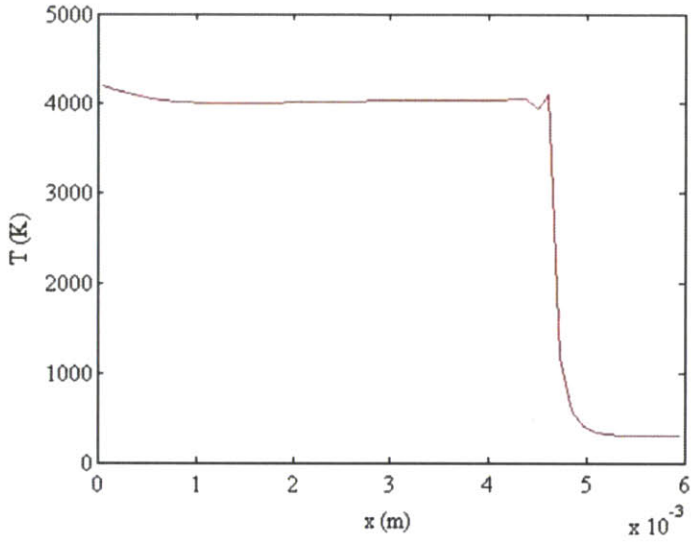

Figure 3. Uncoupled Zr reaction front temperature profile. Initial oxide fraction = 75%. Initial system diameter = 10 μm. t = 1250 s.

Arimondi *et al.* represented the kinetics term, $\frac{\partial \eta}{\partial t}$, as the minimum of the diffusion rate of oxygen through the solid oxide layer and the transport rate of oxygen gas to the surface of the cylinder. For nanoscale systems, oxygen transport may not be the rate-limiting step.

Nevertheless, we use Arimondi's kinetic expressions in order to reproduce their results and prove our model's validity. The kinetic terms are integrated using a fourth-order Runge-Kutta method.

The boundary conditions for the model are

$t \geq 0$, $x = 0$ $T = 4500$ K (adiabatic combustion temperature of Zr)

$t = 0$, $x > 0$ $T = 298$ K

The initial composition of the system is 50% Zr and 50% ZrO_2, unless specified otherwise. We use Arimondi's average values for thermal conductivity of Zr and ZrO_2: 35.5 and 4.15 W/m/K, respectively. Oxygen partial pressure is 1 atm. SWNT density and specific heat are estimated to be 1300 kg/m^3 and 770 J/kg/K [35], respectively. This is a very rough estimate, but the specific heat of nanotubes should not vary by more than a factor of three over the temperature range of the simulations [36]. The system length is fixed at 6 mm so that the length is always much greater than the diameter of the system (for which we used values up to 200 nm) in order to justify the one-dimensional approximation.

Another important constraint is the induction distance, below which thermal transport and chemical reaction of the reaction front are not at steady state; the system length must be several times greater than this to accurately determine reaction front velocity. We can estimate the induction distance as $\sqrt{\alpha_1 \tau}$ where α_1 is the thermal diffusivity in the carbon nanotube (at most 6.6x10^{-3} m^2/s) and τ is the characteristic time for the reaction front to develop. The parameter τ can be approximated as d_M/v_{ss}, where d_M is the thickness of the metal annulus (at most 100 nm in this work) and v_{ss} is the steady state reaction front velocity in the absence of thermal coupling to the SWNT (0.4 m/s, as seen in Figure 4). Using the above values, we estimate a maximum induction distance of 40 μm. As long as the system is at least 100 μm long, we can consider the reaction front to be well developed for most of the length.

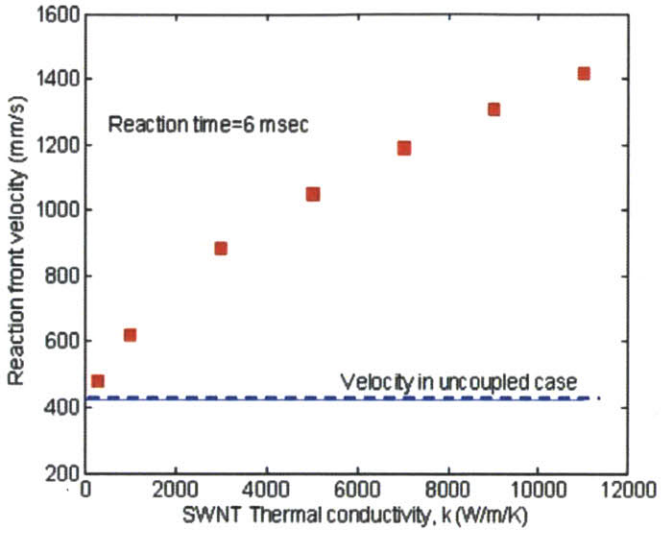

Figure 4. Effect of SWNT thermal conductivity on reaction front velocity. SWNT diameter = 1 nm with G = 100 W/m^2/K, initial oxide fraction of 0.5 and initial system diameter of 10 nm. For k_{SWNT} = 6600 W/m/K, velocity is increased by a factor of three over the reaction of Zr with no SWNT present (G = 0) (blue dotted line).

Figure 4 shows that, for a constant interfacial conductance, reaction front velocity in the coupled system increases with higher SWNT thermal conductivity. These data support the hypothesis that the nanotube will absorb the heat generated by the reaction and quickly disperse the energy along its length, initiating more reactions. A G value of 100 $Wm^{-2}K^{-1}$ is exceedingly low; G for the interface between SWNTs and sodium dodecyl sulfate (SDS) has been measured at $1.2x10^6$ $Wm^{-2}K^{-1}$ [37] and $4.1x10^8$ $Wm^{-2}K^{-1}$ between SWNTs and epoxy [38]. Still, even at this G value the reaction front velocity can be increased by about a factor of three by the addition of SWNTs to the Zr, assuming the highest calculated SWNT thermal conductivity from the literature [22].

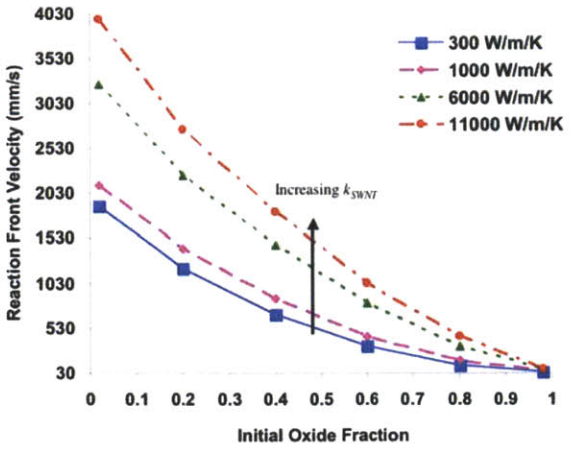

Figure 5. Influence of initial oxide fraction on reaction front velocity. Initial system diameter = 10 nm, SWNT diameter = 1 nm, G = 100 W/m^2/K, velocities calculated after 6 ms. The SWNT increases velocity more for higher oxide fractions because thermal conductivity through nanoparticles with higher oxide fraction is accordingly lower.

As one would expect, reaction front velocity decreases with an increasing fraction of the initial Zr mass in the oxide form, as seen in Figure 5. However, a careful examination reveals that SWNTs provide the largest enhancement (in fractional terms), for the higher initial oxide concentrations. Since the thermal conductivity of ZrO_2 is only 12% of that of Zr, the faster heat dissipation through the nanotube outpaces the thermal energy moving through the Zr annulus even more in this case. For an initial concentration of 20% ZrO_2 increasing k_{SWNT} from 300 to 11000 W/m/K corresponds to a 125% increase in reaction front velocity. But for an initial concentration of 80% ZrO_2, the same conductivity increase results in a 275% increase in reaction front velocity.

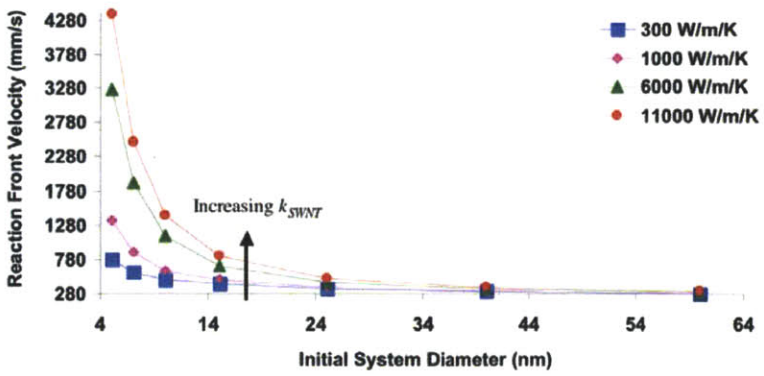

Figure 6. Effect of initial system diameter on reaction front velocity. SWNT diameter = 1 nm. G = 100 W/m^2/K, initial oxide fraction = 50%, velocities calculated after 6 ms. The greatest increases in velocity are possible when initial system diameter is decreased below 15 nm (7 nm Zr annulus diameter).

The previous three figures display data for simulations of SWNT-Zr complexes initially 10 nm in diameter. As Figure 6 shows, the magnitude of enhancement from the addition of the SWNT drops off precipitously with increasing system diameter. When the annulus outer diameter is 5 nm, the enhancement is 460% but it drops to 41% at 25 nm and a mere 7% for a 60 nm annulus. This reflects a shift in the primary reaction barrier from activation energy at small initial diameters to the oxygen transport-limited case at larger diameters as the surface area to volume ratio of the Zr phase increases. Furthermore, since the metal mass increases as the cube of diameter, much more heat is being generated by the reaction of the larger annulus, and the heat capacity of the SWNT is rapidly saturated, limiting its effectiveness for thermal transport. However, since the model equations do not take into account heat transfer in the radial direction, the actual reaction front velocity parallel to the SWNT in larger diameter systems will be slower than these simulations indicate; energy will not be confined to the layer nearest the SWNT.

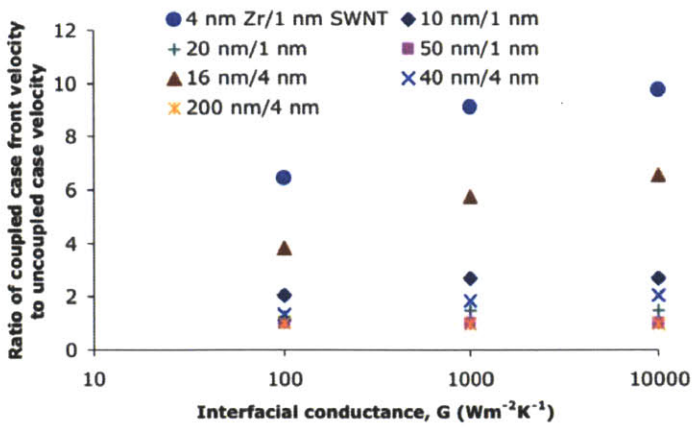

Figure 7. Effects of SWNT diameter and initial system diameter on reaction front velocity. Initial oxide fraction = 50%, k_{SWNT} = 3000 W/m/K. Velocities were calculated after steady state was attained at 1.3 ms.

Figure 7 demonstrates that, provided SWNT conductivity is sufficiently large, higher interfacial conductance leads to a greater enhancement in reaction front velocity. However, the relation is not linear; gains in reaction front velocity grow progressively smaller with each order of magnitude increase in interfacial conductance. Even if *G* between Zr and SWNTs were as large as between SWNTs and SDS (1.2×10^6 $Wm^{-2}K^{-1}$), the improvement over $G = 10^4$ $Wm^{-2}K^{-1}$ would be marginal. For the 4 nm annulus outer diameter/1 nm SWNT system, the improvement in the enhancement ratio between 1000 and 10000 $Wm^{-2}K^{-1}$ is only from 9.1 to 9.7, or 7%. As *G* becomes large, the nanotube thermal conductivity becomes the limiting factor in energy propagation. This is evident in Figure 8, in which only very small enhancements in reaction front velocity result from increased *G*.

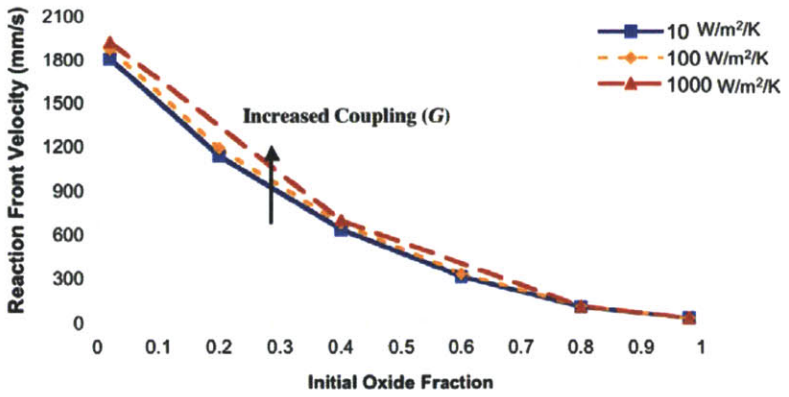

Figure 8. Effects of interfacial conductance on reaction front velocity for low k_{SWNT}. Initial system diameter = 10 nm, SWNT diameter = 1 nm, k_{SWNT} = 300 W/m/K, velocities calculated after 6 ms. SWNT conductivity and heat capacity, not thermal coupling, limit velocity increase in this case.

Even using the highest SWNT conductivity value predicted from the literature, 6600 W/m/K, does not change the overall trend, as Figure 9 shows. Velocity can be increased by a factor of ten over the uncoupled case, but the properties of the nanotube still limit further enhancement for $G > 10^4$ $Wm^{-2}K^{-1}$. Either higher conductivity or a larger SWNT thermal conduit is needed to further increase velocity. However, k_{SWNT} and d_N are inversely related, so the increase will be limited by some optimum combination of the two parameters.

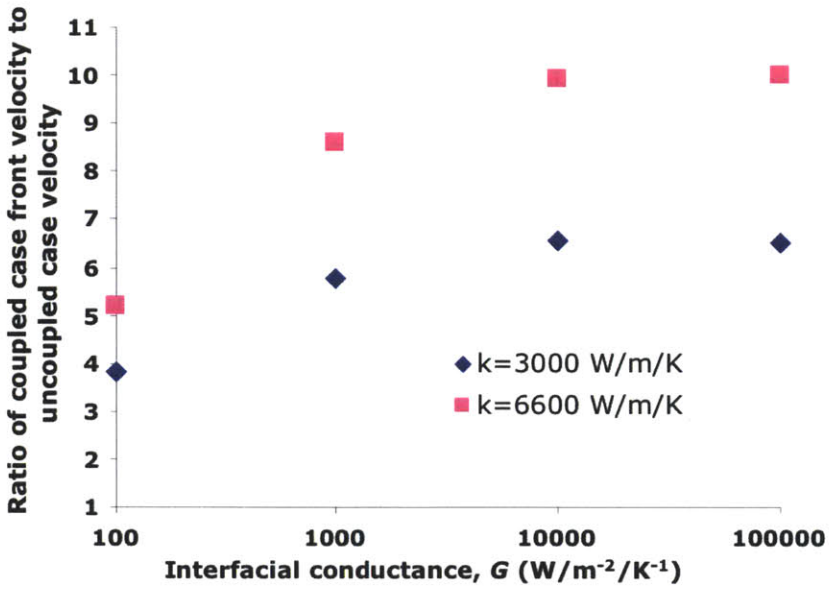

Figure 9. Front velocity enhancement at two different values of k_{SWNT}. Initial system diameter 16 nm, d_{SWNT} = 4 nm. Initial oxide fraction = 50%. At high interfacial conductance, the velocity enhancement after 1.3 ms is limited by SWNT thermal properties for both cases.

It might also be possible to increase front velocity by connecting multiple SWNTs to the metal annulus. However, analysis of the basic differential equations of the model shows that adding some number of equivalent SWNTs has the same effect as multiplying *G* in the one-SWNT case by the total number of SWNTs. Each additional individual nanotube inside the annulus requires the subtraction of another term of the form $\frac{G_i}{\rho_1 C_{p,1}}(T_1 - T_i)\frac{d_{N,i}}{d_m^2}$ from the end of equation (9). Here the index *i* signifies the nanotube in question. If the nanotubes are all equivalent, then all G_i, $d_{N,i}$, and T_i will be equal, and we can simply group the new terms. The end result looks the same as multiplying *G* by some factor. The positioning of SWNTs inside the annulus does not enter into consideration because the model is one-dimensional.

We can similarly simplify other geometries involving multiple SWNTs. A SWNT bundle centered inside the metal annulus will affect temperature in the metal in the same way as one larger-diameter SWNT; we can account for the interfacial resistance between the SWNTs by using a smaller k_{SWNT}. Also, attaching SWNTs to the exterior of the annulus will not lead to reaction velocity enhancements greater than those that the model predicts for the interior SWNT case. The contact area between each exterior nanotube and the metal would be much smaller, and the SWNTs would interfere with oxygen transport to the metal, inhibiting reaction.

Although both Figure 6 and Figure 7 show similar drops in the velocity enhancement as initial system diameter increases for a given nanotube diameter, Figure 7 also shows that increasing the size of the nanotube in the complex can counter this trend. For the purposes of this model a "larger" nanotube could be either a single nanotube with a larger diameter and therefore more mass per unit length or a bundle of smaller tubes with SWNT-SWNT interfacial conductance sufficiently large such that the bundle behaves thermally like a single unit. However, it is not simply a matter of preserving the same mass ratio of Zr to SWNT; the cases of a 16 nm complex with a 4-nm SWNT core and a 4 nm complex with a 1-nm SWNT core have the same mass ratios, but significantly different velocity enhancements. Again, the thickness of the Zr layer is important because, independent of SWNT diameter, it determines the oxygen transport properties and thus the kinetics of the model. For a Zr annulus about twenty times thicker than the SWNT, the nanotube will not increase reaction front velocity appreciably at any value of interfacial conductance.

2.4. Summary

We modeled reaction and heat flow in a system of zirconium nanoparticles attached to a SWNT, approximating the particles as a continuous annulus. The nanotube increased Zr reaction front velocity in the direction of the nanotube length by up to a factor of ten compared to a system containing only Zr. SWNT conductivity and the relative sizes of Zr and SWNT, not interfacial thermal conductance, limit the reaction velocity enhancement. The thickness of the Zr annulus must be less than twenty times the diameter of the SWNT for the nanotube to increase reaction velocity, or else it does not have sufficient heat capacity to handle the energy from the Zr oxidation. Although the enhancement is insufficient to change Zr from a deflagrating to a detonating material, using faster reacting materials may enable SWNTs to effect this transition, but only if the nanotubes have the optimal thermal properties predicted. Our model offers a proof-of-concept for one-dimensional anisotropic energetic materials.

References

1. Menon, L., et al., *Size dependence of energetic properties in nanowire-based energetic materials.* J. Appl. Phys., 2006. **100**(3): p. 034317.
2. Dlott, D.D., *Thinking big (and small) about energetic materials.* Mater. Sci. Tech., 2006. **22**(4): p. 463-473.
3. Aumann, C.E., G.L. Skofronick, and J.A. Martin, *Oxidation behavior of aluminum nanopowders.* J. Vac. Sci. Tech. B, 1995. **13**(3): p. 1178-1183.
4. Bockmon, B.S., et al., *Combustion velocities and propagation mechanisms of metastable interstitial composites.* J. Appl. Phys., 2005. **98**(6): p. 064903.
5. Plantier, K.B., M.L. Pantoya, and A.E. Gash, *Combustion wave speeds of nanocomposite Al/Fe2O3: the effects of Fe2O3 particle synthesis technique.* Combust. Flame, 2005. **140**: p. 299-309.
6. Granier, J.J. and M.L. Pantoya, *Laser ignition of nanocomposite thermites.* Combust. Flame, 2004. **138**: p. 373-383.
7. Dreger, Z.A., et al., *Shock Wave Induced Decomposition Chemistry of Pentaerythritol Tetranitrate Single Crystals: Time-Resolved Emission Spectroscopy.* J. Phys. Chem. B, 2002. **106**: p. 247-256.
8. Brousseau, P. and C.J. Anderson, *Nanometric aluminum in explosives.* Propellants Explosives Pyrotechnics, 2002. **27**(5): p. 300-306.
9. Zel'dovich, Y.B. and Y.P. Raiser, *Physics of Shock Waves and High-temperature Hydrodynamic Phenomena*1966, New York: Academic Press.

10. Arimondi, M., et al., *Chemical Mechanism of the Zr + O2 --> ZrO2 Combustion Synthesis Reaction.* J. Phys. Chem. B, 1997. **101**: p. 8059-8068.
11. Ewald, K.H., U. Anselmi-Tamburini, and Z.A. Munir, *A finite difference model for the combustion of zirconium in oxygen.* J. Mater. Res., 2000. **15**(9): p. 1922-1935.
12. Ewald, K.H., U. Anselmi-Tamburini, and Z.A. Munir, *Combustion of zirconium foils in oxygen.* J. Mater. Res., 2001. **16**(9): p. 2687-2694.
13. Anselmi-Tamburini, U., G. Spinolo, and Z.A. Munir, J. Mater. Synth. Proc., 1993. **1**.
14. Levitas, V.I., et al., *Melt dispersion mechanism for fast reaction of nanothermites.* Appl. Phys. Lett., 2006. **87**: p. 071909-071911.
15. Jindal, V.K. and D.D. Dlott, *Orientation dependence of shock-induced heating in anharmonic molecular crystals.* J. Appl. Phys., 1998. **83**(10): p. 5203-5211.
16. Challis, R.E., et al., *Ultrasound techniques for characterizing colloidal dispersions.* Rep. Progr. Phys., 2005. **68**(7): p. 1541-1637.
17. Suslick, K.S. and G.J. Price, *Applications of ultrasound to materials chemistry.* Annu. Rev. Mater. Sci., 1999. **29**: p. 295-326.
18. Thompson, L.H. and L.K. Doraiswamy, *Sonochemistry: Science and engineering.* Ind. Eng. Chem. Res., 1999. **38**(4): p. 1215-1249.
19. Greiner, N.R., et al., *Diamonds in detonation soot.* Nature, 1988. **333**(6172): p. 440-442.
20. Roy, G.D., et al., *Pulse detonation propulsion: challenges, current status, and future perspective.* Progr. Energ. Combust. Sci., 2004. **30**(6): p. 545-672.
21. Osman, M.A. and D. Srivastava, *Temperature dependence of the thermal conductivity of single-wall carbon nanotubes.* Nanotechnology, 2001. **12**(1): p. 21-24.
22. Berber, S., Y.-K. Kwon, and D. Tomanek, *Unusually High Thermal Conductivity of Carbon Nanotubes.* Phys. Rev. Lett., 2000. **84**(20): p. 4613-4616.
23. Choi, T.Y., et al., *Measurement of the Thermal Conductivity of Individual Carbon Nanotubes by the Four-Point Three-omega Method.* Nano Lett., 2006. **6**(8): p. 1589-1593.
24. Cahill, D.G., et al., *Nanoscale thermal transport.* J. Appl. Phys., 2003. **93**(2): p. 793-818.
25. Che, J.W., T. Cagin, and W.A. Goddard, *Thermal conductivity of carbon nanotubes.* Nanotechnology, 2000. **11**(2): p. 65-69.
26. Fujii, M., et al., *Measuring the thermal conductivity of a single carbon nanotube.* Phys. Rev. Lett., 2005. **95**(6).
27. Kim, P., et al., *Thermal transport measurements of individual multiwalled nanotubes.* Phys. Rev. Lett., 2001. **8721**(21).
28. Hone, J., et al., *Thermal properties of carbon nanotubes and nanotube-based materials.* Appl. Phys. Mater. Sci. Process., 2002. **74**(3): p. 339-343.
29. Hone, J., et al., *Electrical and thermal transport properties of magnetically aligned single walt carbon nanotube films.* Appl. Phys. Lett., 2000. **77**(5): p. 666-668.
30. Yu, C.H., et al., *Thermal conductance and thermopower of an individual single-wall carbon nanotube.* Nano Lett., 2005. **5**(9): p. 1842-1846.
31. Pop, E., et al., *Thermal conductance of an individual single-wall carbon nanotube above room temperature.* Nano Lett., 2006. **6**(1): p. 96-100.
32. Xiao, Y., et al., *Three-phonon Umklapp process in zigzag single-walled carbon nanotubes.* J. Phys. Condens. Matter, 2003. **15**(23): p. L341-L347.
33. Hone, J., et al., *Thermal conductivity of single-walled carbon nanotubes.* Phys. Rev. B, 1999. **59**(4): p. R2514-R2516.
34. Martynenko, Y.V. and L.I. Ognev, *Thermal Radiation from Nanoparticles.* Tech. Phys., 2005. **50**(11): p. 1522-1524.

35. Yi, W., et al., *Linear specific heat of carbon nanotubes.* Phys. Rev. B, 1999. **59**(14): p. R9015-R9018.
36. Li, C. and T.-W. Cho, *Modeling of heat capacities of multi-walled carbon nanotubes by molecular structural mechanics.* Mater. Sci. Eng. A, 2005. **409**: p. 140-144.
37. Huxtable, S.T., et al., *Interfacial heat flow in carbon nanotube suspensions.* Nat. Mater., 2003. **2**(11): p. 731-734.
38. Bryning, M.B., et al., *Thermal conductivity and interfacial resistance in single-wall carbon nanotube epoxy composites.* Appl. Phys. Lett., 2005. **87**(16).

Chapter 3

An Analytical Solution to Coupled Chemical Reaction and Thermally Diffusing Systems

3.1 Background: Self-Propagating Thermochemical Reaction Waves

Self-propagating chemical reaction waves in solids are an interesting phenomenon wherein enthalpy released by a reaction thermally activates further reactions, resulting in a spreading wave front between reacted and un-reacted regions. Such reaction waves are widely used in the chemistry, physics and technology of propulsion.[1-3] This phenomenon is also central to solid materials synthesis in the form of self-propagating high-temperature synthesis (SHS).[4-9] Here, a singular chemical reaction wave can produce a uniform material and/or nanoparticles, for example, Ni/Al composites[10], wear-resistant carbides,[11, 12] as well as $LiCoO_2$ for battery cathodes.[13] SHS can also produce functionally graded composite materials blending thermal and mechanical properties of multiple precursors.[14, 15] For example, TiC and Ni can be blended in this way to produce a composite in which the hardness and density vary continuously along one axis.[14] These systems are generally modeled numerically using finite differences/element/volume methods[1, 6, 15-17] or molecular dynamics.[18] Lastly, in thermopower waves, such self-propagating reaction waves are driven along a thermally conductive nanowire or nanotube.

Thermally coupling an exothermic fuel to an anisotropic heat conductor, such as a carbon nanotube, maintains a large temperature gradient between reacted and un-reacted regions. The conduit

conducts heat released by the fuel's reaction ahead of the front, where it diffuses back into un-reacted fuel, sparking new reactions and accelerating the wave propagation speed. Large surface area-to-volume ratios and temperature differences can overcome the generally mediocre interfacial thermal conductivity between carbon nanotubes and surrounding solids. If the thermal conduit is also electrically conductive, the reaction wave will generate a large pulse of electrical energy accordingly, entraining electrons or holes to produce single-polarity electrical pulses. This is the principle of the thermopower wave, which could overcome certain limitations of conventional TE materials.[19] The electrical pulses produced by the first thermopower wave generators were as large as 7 W/g, and the specific power was greatest in devices with the smallest mass – an unexpected inverse scaling. Such waves may form the basis of new battery and fuel cell technologies.[20, 21]

Interestingly, all of these reaction wave systems share a common mathematical formulation of a one-dimensional Fourier heat diffusion equation with a non-linear Arrhenius source term, coupled to a chemical reaction equation, generally using first-order kinetics.[22-26] Modeling and solving these equations is an important way to calculate the reaction wave velocity and the temperature and chemical conversion profiles, which control and define desired properties.[6, 8, 13, 15] Although approximate solution methods for the equations describing chemical reaction and diffusion abound in the literature, to date no exact analytical solution has been developed. Numerical solutions can offer accurate results, but such simulations of combustion processes and reaction waves are still generally intensive computationally. Moreover, they can be quite sensitive to initial conditions and numerical mesh sizes, making it difficult to find converged solutions to study propagating waves. An analytical solution, even within a limited scope, could significantly accelerate such calculations or eliminate their necessity. We present the first analytical solution to these coupled equations, based on a known form of the solution temperature profile.

3.2 Previous Mathematical Methods for Self-Propagating Waves

In 1938, Zeldovich and Frank-Kamenetskii developed one of the first approximate solution methods for reaction-diffusion equations in gases to describe flame propagation.[27] (One year earlier, R. A. Fisher used very similar equations to describe a variant problem in genetics.)[28] They assumed mass diffusivity and thermal conductivity to be equal, along with constant temperature and reactant concentrations in the zones far ahead of and behind the reaction front. Their approximate solution then focused only on the reaction zone (where the change in temperature is steepest), using a singular perturbation method and a moving coordinate system (also known as a similarity transformation) to solve for the profiles within the reaction zone. Finally, they matched asymptotic expansions to construct complete profiles. This three-zone model was later extended to reaction waves in condensed phases.[22, 23]

Later, Maksimov and Merzhanov contributed a multiphase model for combustion waves in solids (but with the reactions actually occurring in the liquid and gas phases).[29] While this approximation improves accuracy of the velocity calculation for certain systems and requires fewer coarse-scale assumptions, it needs significantly more property information about the materials involved. Additionally, numerical simulations are still needed to produce temperature and conversion profiles of the system. More recently, asymptotic solution methods based on a different temperature scaling have been developed by Weber *et al.*[25] and Please *et al.*[26] to allow for fairly accurate, simple formulae for velocity based only the dimensionless parameter $\beta = \frac{C_p E_a}{-\Delta H R}$, equivalent to the inverse adiabatic reaction temperature rise. Here C_p is specific heat, ΔH is the enthalpy of reaction, R is the universal gas constant, and E_a is the activation energy of reaction. Again, these methods did not yield further information about temperature and conversion without numerical solutions. McIntosh, Weber, and Mercer have extended asymptotic analysis to non-adiabatic conditions and any Lewis number (*i. e.* the

ratio of thermal to mass diffusivity).[30] For a more comprehensive review, see the seminal book from Zeldovich and co-workers[31] or the review on numerical methods from Mukasyan and Rogachev.[1]

In solids, where mass diffusion is negligible on the time scale of reactions, the equations for the energy and mass balances in the approximately one-dimensional large aspect ratio systems where reaction waves are generally studied are as follows:

$$\rho C_p \frac{\partial T}{\partial t} = \chi \frac{\partial^2 T}{\partial x^2} - \left(\Delta H \cdot k_o Y\right) e^{-\frac{E_a}{RT}} \tag{1}$$

$$\frac{\partial Y}{\partial t} = -\left(k_o Y\right) e^{-\frac{E_a}{RT}} \tag{2}$$

Here, ρ is density, T is temperature, t is time, χ is thermal conductivity, x is distance, k_0 is the Arrhenius prefactor, and Y is the (mass) concentration of reactive material. In their most basic, fundamental form, the modeling equations neglect convection and radiation, as these add significant non-linearity, and with the exception of McIntosh *et al.*,[30] all the previously described methods drop those terms. The chemical reaction kinetics are first-order in equation (2), indicating a single-component decomposition or a combustion reaction where the oxidizer is in great excess. This is particularly relevant for the study of thermopower waves, in which the reaction of many useful fuels can be described this way; they decompose very exothermically without need for an oxidizer. Examples include cyclotrimethylene-trinitramine[32, 33], picramide[34], and nitrocellulose[35]. To facilitate mathematical solution, the next step is to non-dimensionalize the other variables – temperature $u = \left(\frac{R}{E_a}\right) T$, time $\tau = \left(\frac{-\Delta H k_0 R}{C_p E_a}\right) t$, space $\xi = x\sqrt{\left(\frac{\rho C_p}{\chi}\right)\left(\frac{-\Delta H k_0 R}{C_p E_a}\right)}$, and concentration $\frac{Y}{\rho} = y$.

Then the simplified equations are

$$\frac{\partial u}{\partial \tau} = \frac{\partial^2 u}{\partial \xi^2} + y e^{-1/u} \tag{3}$$

$$\frac{\partial y}{\partial \tau} = -\beta y e^{-1/u} \tag{4}$$

3.3 Logistic Wave Analytical Solution Method

An analytical solution is, in fact, possible if a general form of the solution is known such that derivatives can be evaluated analytically. This insight is actually aided by numerical solutions of equations (3) and (4), which reveal that the temperature profiles, $u(\xi)$, have a consistent shape over time while the wave velocity, c, is constant. For constant wave velocity, space and time can be combined in a moving coordinate system, as Weber *et al.* have done:[25] $\eta = \xi - c\tau$. Previous work has demonstrated this to be accurate for $\beta < 7$.[25] Using several different values of β, Figure 1 compares the temperature profiles obtained from numerical solution and from the analytical solution we will subsequently develop in this chapter. A Matlab program solved the implicit equation for Q as a function of β and numerically integrated the equation for y. The numerical solution was calculated using COMSOL 3.5 with an adaptive time-stepping finite element method and spatial mesh size of $\Delta\xi = 2$ over a total length of 6000 (*i.e.* 3000 points). This solution was also tested at other mesh spacings ranging from $\Delta\xi = 0.5$ to $\Delta\xi = 10$ to verify convergence.

The shape of the temperature profiles is recognizable as a logistic function, the general form of which is

$$u(\eta) = \frac{u_{max}}{(1 - Qe^{s\eta})^{1/Q}} \tag{5}$$

Here u_{max} is the maximum temperature of the reaction, reached behind the front and s is the growth parameter, which affects the slope of u in the middle of the curve. Using this form assumes that the temperature does not overshoot the upper asymptote and that the temperature of the surroundings is

assumed to approach zero, such that the lower asymptote of $u(\eta)$ does as well. Finally, Q is a symmetry parameter that affects the different curvatures of the function near the asymptotes. When $Q = 1$, the function is symmetric around its inflection point; the upper and lower curvatures are equal.

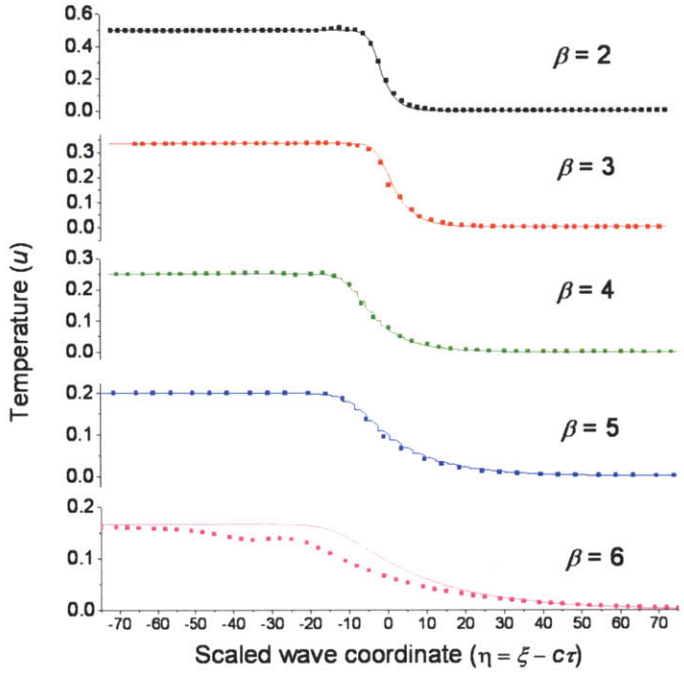

Figure 1: Analytical and numerical solutions using a logistic temperature profile. Analytical solutions are represented by lines, numerical solutions by points. The profiles match closely for several different values of β. Above $\beta = 6$ the logistic form becomes less accurate.

Restating equations (3) and (4) in terms of η, we have

$$-cu' = u'' - ye^{-1/u} \tag{6}$$

$$cy' = \beta ye^{-1/u} \tag{7}$$

The dashes denote differentiation with respect to η; the derivatives can be calculated exactly since $u(\eta)$ is known.

Given the form of $u(\eta)$, it is possible to analytically solve equations (6) and (7) by examining the limits of the functions, since the solutions must be consistent everywhere. Multiplying equation (6) by a factor of β and subtracting equation (7) yields $-\beta cu' - cy' = \beta u''$, which can then be integrated once to yield

$$-\beta cu - cy = \beta u' - K \tag{8}$$

where K is an integration constant. Applying the $\eta \to \infty$ boundary condition (far ahead of the reaction front), $y \to 1$ (completely un-reacted fuel) and $u \to 0$. In this limit, $u' \to 0$ as well, so it is simple to derive that $K = -c$. Then y can be written as a function of u.

$$y = 1 - \beta u - \frac{\beta}{c} u' \tag{9}$$

Applying the second boundary condition, as $\eta \to -\infty$ (far behind the reaction front), $y \to 0$ (completely reacted) and $u \to u_{max}$. Equation (8) then becomes

$$-\beta c u_{max} = \beta \left[-u_{max} s e^{\eta s} \left[1 - Q e^{\eta s} \right]^{-1 - Q/Q} \right] - c$$

and since $e^{\eta s} \to 0$, $u_{max} = \frac{1}{\beta}$. This is consistent with the findings of other approximate solution methods.[25]

After the coordinate transformation, equation (7) is now an ordinary differential equation and can be solved to yield

$$y(\eta) = C \cdot e^{\int_1^{\eta} \left(\frac{\beta}{c}\right) e^{(-\beta)(1-Q e^{\eta_2 s})^{1/Q}} d\eta_2} \tag{10}$$

Here C is a constant of integration, and η_2 is a dummy variable for integration. When $\eta = 1$, the integral is zero, so therefore $C = y(1)$.

The next insight is available by examining equation (6) in the limit of the first boundary condition ($\eta \to \infty$), using the analytical expressions for the derivatives.

$$\left(\frac{1}{\beta}s^2e^{\eta s}\left(-1+e^{\eta s}\right)\left(1+Qe^{\eta s}\right)^{-2-(1/Q)}\right)+c\left(\frac{-1}{\beta}se^{\eta s}\left(1+Qe^{\eta s}\right)^{-(1+Q)/Q}\right)+ye^{-\beta\left(1+Qe^{\eta s}\right)^{1/Q}}=0 \qquad (11)$$

which simplifies to

$$ye^{-\beta\left(1+Qe^{\eta s}\right)^{1/Q}}=\frac{1}{\beta}\left(se^{\eta s}\left(1+Qe^{\eta s}\right)^{-2-(1/Q)}\left(c+s+e^{\eta s}\left(cQ-s\right)\right)\right)$$

In this limit, $e^{-1/u} \to 0$, so the left side of the equation approaches zero as well. Factoring yields

$$\frac{e^{2\eta s}}{\beta}\left(s\left(1+Qe^{\eta s}\right)^{-2-(1/Q)}\left(ce^{-\eta s}+se^{-\eta s}+\left(cQ-s\right)\right)\right)\to 0$$

Parameters *c*, *s*, *Q*, and *β* are all constant, finite, and positive. Of the last set of terms, $ce^{-\eta s} \to 0$ and $se^{-\eta s} \to 0$, so this can only be satisfied if $s = cQ$. Since these variables are all constant, the validity of this relation at the infinite limit can be extended to the entire domain.

Now it is possible to solve for *c* solely as a function of *Q* and *β* by substituting equation (9) back into equation (6). This combined equation is

$$\frac{1}{\beta}\left(e^{-\beta\left(1+Qe^{\eta cQ}\right)^{1/Q}}\left(1+Qe^{\eta cQ}\right)^{-2-(1/Q)}\right)$$
$$\left(-c^2Q\left(1+Q\right)e^{\eta cQ+\beta\left(1+Qe^{\eta cQ}\right)^{1/Q}}+\beta\left(1+Qe^{\eta cQ}\right)\left(-1+\left(1+Qe^{\eta cQ}\right)^{1/Q}+Qe^{\eta cQ}\left(1+Qe^{\eta cQ}\right)^{1/Q}\right)\right)=0$$

This equation can be simplified when $\eta = 0$; once again, since *c* is constant, its value for $\eta = 0$ will be true everywhere.

$$\frac{1}{\beta}\left(e^{-\beta(1+Q)^{1/Q}}\left(1+Q\right)^{-2-(1/Q)}\right)\left(-c^2Q\left(1+Q\right)e^{\beta(1+Q)^{1/Q}}+\beta\left(1+Q\right)\left(-1+\left(1+Q\right)^{1/Q}+Q\left(1+Q\right)^{1/Q}\right)\right)=0$$

Solving this for *c* yields a positive solution of

$$c = e^{-(\beta/2)(1+Q)^{1/Q}} \sqrt{\frac{\beta}{Q}\left(-1+(1+Q)^{(1+Q)/Q}\right)} \tag{12}$$

Equation (6) can also be solved at $\eta = 1$ to eliminate the problem of calculating the integral in equation (10) exactly.

$$\left(\frac{1}{\beta}c^2Q^2e^{cQ}\left(-1+e^{cQ}\right)\left(1+Qe^{cQ}\right)^{-2-(1/Q)}\right)+c^2\left(\frac{-1}{\beta}Qe^{cQ}\left(1+Qe^{cQ}\right)^{-(1+Q)/Q}\right)+Ce^{-\beta\left(1+Qe^{cQ}\right)^{1/Q}}=0 \tag{13}$$

The functional form is complicated, so it is not simple to explicitly solve for Q, even with an expression for c now available. However, it is relatively straightforward to implicitly solve this equation by iterating Q and C (that is, $y(\eta = 1)$) such that both equations (13) and (10) are satisfied. (Numerical integration is required in equation (10).)

Empirically, the implicit solution for $Q = f(\beta)$ can be approximated by a cubic polynomial, as shown in Figure 2a.

$$Q = 0.0061\beta^3 - 0.077\beta^2 + 1.2531\beta - 0.208 \tag{14}$$

The real root of this equation is $\beta = 0.1677$; since Q must be positive, this gives one bound for the validity of this solution method. The functional form of c still depends most strongly on the exponential term, as the comparison to the fit curve in Figure 2b shows. The square root term in equation (12) contributes little, although its effects increase as β and Q decrease. This confirms the results of previous asymptotic methods for estimating c.[25, 26]

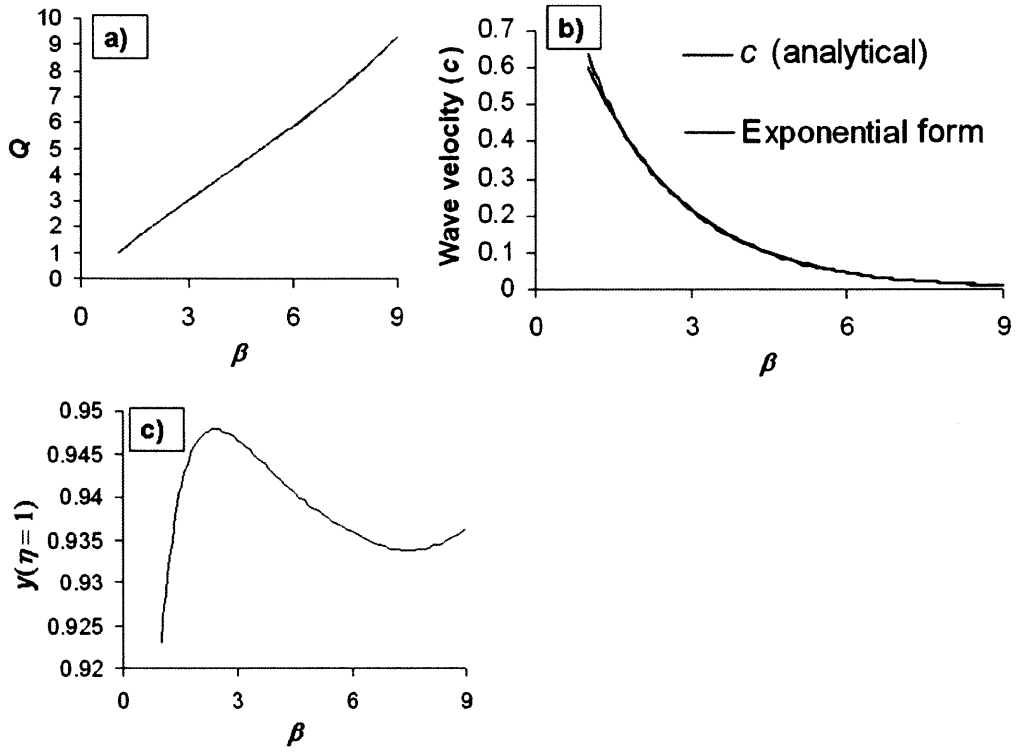

Figure 2: Effects of β on reaction wave parameters. a) The logistic symmetry parameter (Q) is a cubic function of β. b) Wave velocity (c) shows an inverse exponential dependence on β, confirming the results of asymptotic solution methods. c) The reactant concentration (y) at $\eta = 1$, which is the constant of integration in equation (10), does not vary monotonically with β.

However, not all parameters are simply monotonic functions of β. As Figure 2c shows, $y(1)$, which is the constant of integration in equation (10), has a maximum at $\theta = 2.5$ and a minimum at $\theta = 7.6$. It only varies a few percent over $1 < \beta < 9$, and its rapid drop in the region of $\theta < 2.5$ further demonstrates a breakdown in steady wave propagation.

3.4 Generalization to n^{th}-order Kinetics

The solution method can be generalized to any n^{th}-order chemical kinetics involving only one reactant. For n^{th}-order reactions, the Arrhenius prefactor k_0 has units that depend on n: (time)$^{-}$

^{1}(concentration)$^{1-n}$. However, the non-dimensionalization of Y^n to $\rho^n y^n$ provides an extra factor that compensates for these units in the time and space scalings, which then become $\tau = \left(\frac{-\Delta H k_0 \rho^{n-1} R}{C_p E_a} \right) t$ and $\xi = x \sqrt{\left(\frac{\rho C_p}{\chi} \right) \left(\frac{-\Delta H k_0 \rho^{n-1} R}{C_p E_a} \right)}$. After this, one simply replaces y with y^n in equations (3) and (4), and equations (6) and (7) can be combined in the same way as in the $n = 1$ solution such that the last term of equation (6) is replaced with cy'. The application of boundary conditions in the next steps is not affected. But when equation (9) for $y = f(u,u')$ is combined with equation (6), it is as y^n, so a different equation for c is derived.

$$c = e^{-(\beta/2)(1+Q)^{1/Q}} \sqrt{\frac{\beta}{Q}(1+Q)^{(1+Q)/Q}\left(1-(1+Q)^{(Q-1)/Q}\right)^n} \qquad (15)$$

The integration to obtain $y(\eta)$ yields a result of a similar form as equation (10).

$$y(\eta) = \left((n-1)\left(-C - \int_1^{\eta} \left(\frac{\beta}{c} \right) e^{(-\beta)(1+Qe^{\eta_2 s})^{1/Q}} d\eta_2 \right) \right)^{\frac{1}{1-n}} \qquad (16)$$

with $y(1) = \left(C(1-n)\right)^{\frac{1}{1-n}}$. The change to n^{th}-order kinetics affects the temperature profile shape by replacing C with $y(1)^n = \left(C(1-n)\right)^{\frac{n}{1-n}}$ in equation (13), which is solved self-consistently with equation (10) for c and Q. The solution method could also be extended to other chemical kinetics (*e.g.* bimolecular) in a similar way as described here, although introducing mass diffusion (*i.e.* with fluids rather than solids) would require a y'' term in equation (7), and thus a different solution method.

3.5 Solution Method Limits, Accuracy, and Applications

The most significant limitation of this solution method is its requirement of constant wave velocity, c. Above a certain value of β (Weber *et al.* found it to be 6.8),[25] temperature overshoots

that the temperature profile is no longer consistently a logistic function of the form in equation (5). We also note that for $\beta < 1$, the error in iterative solution method for equations (10) and (13) diverges rapidly, another indication of the lack of steady wave propagation in this regime that others have noted.[25, 26]

The accuracy of the analytical solution method is supported by comparison with numerical solution. Figure 1 shows temperature profiles for $2 < \beta < 6$ calculated analytically and, using the COMSOL software package, numerically. The initial conditions for the numerical solutions were $u(\xi, \tau = 0) = g \cdot e^{-\xi^2/w}$ and $y(\xi, \tau = 0) = 1$, where $g = 0.15$ and $w = 500$. At each value of β, the shapes of the temperature profiles match closely. This confirms the validity of the original choice of functional form, although for $\beta > 6$, the logistic form becomes less accurate. We note also that the numerical method tends to over-predict average velocity since it includes an initial energy pulse required to initiate reaction, whereas the analytical solution only deals with steady wave propagation long after the initial phase.

We anticipate that analytical solution techniques of this form will support the study of thermopower waves. Advances in understanding wave physics and in device design require more detailed models that can predict the voltage and current generated in highly anisotropic systems with large temperature gradients. Such models would benefit from complete time-dependent solutions for temperature and chemical potential and could help to explain the anomalously large voltage generated by thermopower waves in experiments to date. The modeling equations for carrier density and potential (e.g. drift-diffusion) can even be uncoupled from the energy balance and reaction equations (1) and (2) since the time scale for carrier motion and equilibration with the lattice is considerably shorter than the time scales for heat diffusion and chemical reaction.

We have demonstrated an analytical solution to the equations describing thermal and chemical reaction waves in solids. It requires fewer assumptions and less information about system physical

properties than other methods, such the three-zone approximation or asymptotic expansions. This solution should be useful in many scientific disciplines, including self-propagating high-temperature synthesis (SHS) and thermopower waves.

References

1. Mukasyan, A.S. and A.S. Rogachev, *Discrete reaction waves: Gasless combustion of solid powder mixtures.* Progress in Energy and Combustion Science, 2008. 34(3): p. 377-416.
2. Margolis, S.B., *The Transition to Nonsteady Deflagration in Gasless Combustion.* Progress in Energy and Combustion Science, 1991. 17(2): p. 135-162.
3. Zenin, A., *HMX and RDX - Combustion Mechanism and Influence and Modern Double-Base Propellant Combustion.* Journal of Propulsion and Power, 1995. 11(4): p. 752-758.
4. Baras, F. and D. Kondepudi, *A multilayer model for self-propagating high-temperature synthesis of intermetallic compounds.* Journal of Physical Chemistry B, 2007. 111(23): p. 6457-6468.
5. Gennari, S., et al., *Self-propagating high-temperature synthesis of intermetallic compounds: A computer simulation approach to the chemical mechanisms.* Journal of Physical Chemistry B, 2003. 107(3): p. 732-738.
6. Arimondi, M., et al., *Chemical mechanism of the Zr+O-2->ZrO2 combustion synthesis reaction.* J. Phys. Chem. B, 1997. 101(41): p. 8059-8068.
7. Rodriguez, M.A., et al., *Single-Crystal Beta-Si_3N_4 Fibers Obtained by Self-Propagating High-Temperature Synthesis.* Advanced Materials, 1995. 7(8): p. 745-747.
8. Mossino, P., *Some aspects in self-propagating high-temperature synthesis.* Ceramics International, 2004. 30(3): p. 311-332.
9. Patil, K.C., S.T. Aruna, and S. Ekambaram, *Combustion synthesis.* Current Opinion in Solid State & Materials Science, 1997. 2(2): p. 158-165.
10. Hunt, E.M., K.B. Plantier, and M.L. Pantoya, *Nano-scale reactants in the self-propagating high-temperature synthesis of nickel aluminide.* Acta Materialia, 2004. 52(11): p. 3183-3191.
11. Aruna, S.T. and A.S. Mukasyan, *Combustion synthesis and nanomaterials.* Current Opinion in Solid State & Materials Science, 2008. 12(3-4): p. 44-50.
12. Rogachev, A.S. and A.S. Mukasyan, *Combustion of heterogeneous nanostructural systems.* Combustion Explosion and Shock Waves, 2010. 46(3): p. 243-266.
13. Wen, Y.X., et al., *Self-propagating high temperature synthesis of LiCoO2 as cathode material for lithium ion batteries.* Journal of Inorganic Materials, 2008. 23(2): p. 286-290.
14. Zhang, X.H., et al., *TiC-Ni functionally gradient material produced by SHS.* Journal of Inorganic Materials, 1999. 14(2): p. 228-232.
15. Miyamoto, Y., et al., *Functionally graded materials: design, processing, and applications.* Materials Technology Series1999, Boston: Kluwer Academic Publishers.
16. Abrahamson, J.T., N. Nair, and M.S. Strano, *Modelling the increase in anisotropic reaction rates in metal nanoparticle oxidation using carbon nanotubes as thermal conduits.* Nanotechnology, 2008. 19(19): p. 195701-195708.

17. Maglia, F., et al., *Computer simulation approach to the chemical mechanisms of self-propagating high-temperature reactions: Effect of phase transitions on the thermite reaction between O-2 gas and Zr powders.* J. Phys. Chem. B, 2002. 106(23): p. 6121-6128.
18. Nair, N. and M.S. Strano, *One-dimensional nanostructure-guided chain reactions: Harmonic and anharmonic interactions.* Phys. Rev. B, 2009. 80(17).
19. Choi, W., et al., *Chemically Driven Carbon Nanotube-Guided Thermopower Waves.* Nature Materials, 2010. 9: p. 423-429.
20. Choi, W.J., et al., *Chemically Driven Carbon Nanotube-Guided Thermopower Waves.* Nature Materials, 2010. 9: p. 423-429.
21. Choi, W., et al., *Carbon Nanotube-Guided Thermopower Waves.* Materials Today, 2010. 13(10): p. 14-25.
22. Khaikin, B.I. and A.G. Merzhanov, *Theory of thermal propagation of a chemical reaction front.* Fizika Goreniya i Vzryva, 1966. 2(3): p. 36-46.
23. Novozhilov, B.V., *Propagation speed of an exothermic reaction front in a condensed phase.* Doklady Akademii Nauk SSSR, 1961. 141(1): p. 151.
24. Gatica, J.E., J. Puszynski, and V. Hlavacek, *Reaction front propagation in nonadiabatic exothermic reaction flow systems.* AIChE Journal, 1987. 33(5): p. 819-833.
25. Weber, R.O., et al., *Combustion waves for gases (Le=1) and solids (L->infinity).* Proceedings of the Royal Society of London Series a-Mathematical Physical and Engineering Sciences, 1997. 453(1960): p. 1105-1118.
26. Please, C.P., F. Liu, and D.L.S. McElwain, *Condensed phase combustion travelling waves with sequential exothermic or endothermic reactions.* Combust. Theor. Model., 2003. 7(1): p. 129-143.
27. Zeldovich, Y.B. and D.A. Frank-Kamenetskii, *The theory of thermal flame propagation.* Zh. Fiz. Khim., 1938. 12: p. 100-105.
28. Fisher, R.A., *The wave of advance of advantageous genes.* Annals of Eugenics, 1937. 7: p. 355-369.
29. Maksimov, É.I. and A.G. Merzhanov, *A theory for the combustion of condensed materials.* Fizika Goreniya i Vzryva, 1966. 1(1): p. 47-58.
30. McIntosh, A.C., R.O. Weber, and G.N. Mercer, *Non-adiabatic combustion waves for general Lewis numbers: Wave speed and extinction conditions.* Anziam Journal, 2004. 46: p. 1-16.
31. Zeldovich, Y.B., et al., *The mathematical theory of combustion and explosions*, ed. A.n. SSSR.1985: Consultants Bureau New York.
32. Williams, M.R. and M.V. Matei, *The decomposition of some RDX and HMX based materials in the one-dimensional time to explosion apparatus. Part 1. Time to explosion and apparent activation energy.* Propellants Explosives Pyrotechnics, 2006. 31(6): p. 435-441.
33. Oyumi, Y., *Melt phase decomposition of RDX and two nitrosamine derivatives.* Propell. Explos. Pyrot., 1988. 13: p. 42-47.
34. Brill, T.B. and K.J. James, *Thermal decomposition of energetic materials. 61. Perfidy in the amino-2,4,6-trinitrobenzene series of explosives.* Journal of Physical Chemistry, 1993. 97(34): p. 8752-8758.
35. Chen, J.K. and T.B. Brill, *Thermal Decomposition of Energetic Materials 50. Kinetics and Mechanism of Nitrate Ester Polymers at High Heating Rates by SMATCH/FTIR Spectroscopy.* Combustion and Flame, 1991. 85: p. 479-488.

Chapter 4

Velocity Oscillations of Carbon-Nanotube-Guided Thermopower Waves: Towards Nanoscale Alternating Current Sources

4.1 Introduction: Thermopower Waves and Oscillating Electrical Generators

Interest is growing in the development of micro- or nano-sized energy storage[1, 2] and harvesting systems[3-9] that are capable of releasing energy at high rates. This is motivated by emerging applications such as so-called "smart dust",[10] micro-electro-mechanical systems,[11] disposable medical diagnostics,[12, 13] and flexible electronic devices.[14] However, power sources capable of the direct conversion of chemical energy to oscillating current do not exist, despite obvious applications of alternating current waveforms such as cardiac defibrillation and pacemaker signals,[12, 15] micro-piezoelectric oscillators,[4] RF identification tags,[16] and micro-mixers.[17] In this chapter, we investigate the nonlinear coupling between exothermic chemical reactions and a nanotube or nanowire with large axial heat conduction, resulting in self-propagating thermal waves guided along the nano-conduit. The resulting reaction wave induces a concomitant thermopower wave of high power density (> 7 W/g) resulting in an electrical current that travels along the same direction. We show that such waves are predicted to demonstrate oscillatory front velocities under certain values of the chemical reaction rate constants and thermal parameters. These oscillations are verified experimentally using a cyclotrimethylene-trinitramine (TNA)/multiwalled carbon nanotube (MWNT) system and find a dominant frequency at approximately 430 Hz. We show that the oscillations and the frequency

dispersion are well described using diffusive heat transfer model with nonlinear source term coupled to a reactive, non-diffusive mass balance along the nano-conduit.

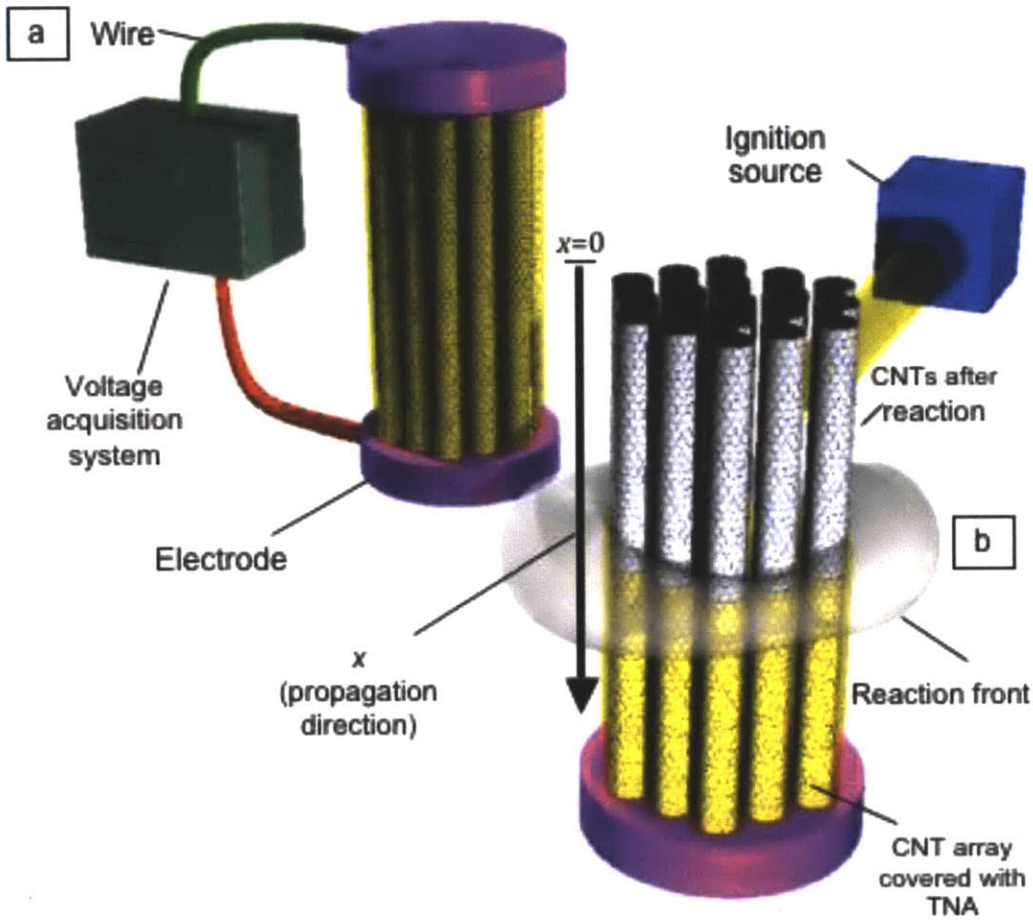

Figure 1: (a) Schematic of the thermopower wave generator. (b) Ignition at one end of a TNA-CNT array results in an exothermic decomposition reaction that propagates along the CNTs *via* its high axial thermal conductivity. The resulting thermal wave develops a concomitant thermopower wave of high power density.

Carbon nanotubes (CNTs) have several advantages for propagating these thermopower waves, despite possessing unexceptional Seebeck coefficients (approximately 80 μV/K at room temperature for individual MWNTs).[18] They remain stable during high-temperature anaerobic reactions, and their axial thermal conductivity is exceedingly high,[19] resulting in large reaction front velocities and therefore large specific power outputs. The surface-to-volume ratios are also large for ordered 2D and 3D arrays

of nanotubes, resulting in sizable heat exchange rates. Conversely, high Seebeck coefficient materials such as Bi_2Te_3 and Sb_2Te_3 are counter-intuitively not favorable for guiding thermopower waves due to their low thermal conductivities.

We use TNA as the fuel source due to its large enthalpy of reaction and strong adhesion to CNTs. CNTs are wrapped in TNA as shown in Figure 1; the reaction occurs at one end of this TNA-CNT system and propagates with the help of CNT conduits. We have previously demonstrated large power densities using TNA-CNT systems.[20] In this chapter, we show that the theory of such self-propagating thermal waves predicts distinct regimes where oscillatory wave front velocities are possible and demonstrate their existence experimentally. Both theory and measurements are in agreement, with oscillations ranging in frequency from 400 to 5000 Hz.

4.2 Theory of Thermopower Wave Oscillations

We consider an annulus of material capable of first-order, exothermic decomposition (such as TNA) surrounding a carbon nanotube. Initiation of the chemical decomposition releases heat that travels much faster along the nanotube than in the annulus, resulting in a reaction wave guided by the CNT. We consider the diffusive transport limit where the reaction zone length exceeds that of the phonon mean free path in the CNT. The coupled thermal diffusion and chemical reaction terms can then be described using a modified Fourier's Law equation with a nonlinear source term to account for the chemical reaction. Under adiabatic conditions, the equation for the temperature of the annulus (T) becomes:

$$\frac{\rho C_p}{M_W}\frac{\partial T}{\partial t} = \chi\frac{\partial^2 T}{\partial x^2} \quad (1)$$

where G_0 is the interfacial conductance between the CNT and TNA, d_M is the outer diameter of the TNA-CNT system, and d_N is the CNT diameter. The parameter χ is the thermal conductivity, ρ is the density,

Q is the enthalpy of reaction, y is the molar concentration of reactive material, k_0 is the Arrhenius prefactor, R is the universal gas constant, E_a is the activation energy of decomposition, and C_p and M_W are the (molar) specific heat and molecular weight of the material, respectively. The second term on the right side accounts for the thermal source of the decomposition reaction, with the mole fraction of unreacted material (y/y_0) decreasing in time and space (according to the spatial profile of T) according to:

$$\frac{\partial y}{\partial t} = -\left(k_o y\right) e^{\left(-E_a / RT\right)} \tag{2}$$

The corresponding equation for the temperature (T_2) evolution in the carbon nanotube includes only terms for the heat transfer from the annulus and thermal diffusion:

$$\frac{\rho_2 C_{p,2}}{M_{W2}} \frac{\partial T_2}{\partial t} = \chi_2 \frac{\partial^2 T_2}{\partial x^2} + G_0 \frac{4}{d_N}\left(T - T_2\right) \tag{3}$$

where the subscript "2" refers to properties of the CNT. Equations 1 through 3 are solved using the following boundary conditions.

$$T_1\left(x, t=0\right) = g \cdot e^{-x^2/w} + T_{ambient}$$

$$T_2\left(x, t=0\right) = g \cdot e^{-x^2/w} + T_{ambient}$$

$$\frac{y}{y_0}\left(x > 0, t=0\right) = 1$$

$$\frac{y}{y_0}\left(x = 0, t\right) = 0.001$$ (to approximate a zero [completed reacted] boundary condition)

The pulse width parameter w is 2×10^{-11} m$^2 \cdot \beta$. $T_{ambient}$ is the temperature of the surroundings, assumed to be 298 K. The parameter grouping $\beta = \frac{C_p E_a}{-QR}$ is the inverse dimensionless adiabatic reaction temperature rise, which is shown to be important for determining wave characteristics. The function $T(x, t = 0)$ is a Gaussian pulse, offset by 298 K, to simulate initiation by a rapid pulse of heat, for

example, from a laser or electrical filament. Here, g is the maximum initial temperature. From numerous simulations we determined empirically that it must be greater than 0.16*exp(0.37β) to initiate a propagating reaction wave. Physically, the magnitude of the temperature initial condition must increase with β since that parameter is proportional to specific heat and activation energy. More energy must be supplied in the initial pulse for larger values of β to overcome specific heat and activation energy and increase the initial reaction rate sufficiently to sustain self-propagation. The initial condition for the composition of the material, y/y_0, corresponds to a completely unreacted annulus, with the exception of the $x = 0$ boundary, which is almost entirely reacted so as to be consistent with the temperature condition, as is necessary for numerical stability. The boundaries of the system are assumed to be adiabatic, and the system is made to be sufficiently long such that the wave is far from the boundaries.

Our work is the first to examine this mathematical system of two coupled heat transport equations in conjunction with chemical reaction. We have studied variants of these equations previously for the case of nanotube-guided nano-thermites.[21] We also note that simplified versions of equations (1) and (2) have been studied historically to describe 1D combustion waves and combustion synthesis.[22-25] Following Zel'dovich and Kamenetskii,[26] we non-dimensionalize the system of equations. A non-dimensional temperature $u = \left(\frac{R}{E_a}\right)T$, time $\tau = \left(\frac{-Qk_oR}{C_pE_a}\right)t$ and space $\xi = x\sqrt{\left(\frac{\rho C_p}{\chi M_W}\right)\left(\frac{-Qk_oR}{C_pE_a}\right)}$ are shown to appropriately scale the system and resulting reaction wave.[23] A conversion η can be defined $\frac{M_W y}{\rho} = 1 - \eta$. Other parameters of importance are the thermal diffusivities $\alpha = \frac{\chi M_W}{\rho C_p}$ of the annulus and of the nanotube, α_2. The resulting equations are:

$$\frac{\partial u}{\partial \tau} = \frac{\partial^2 u}{\partial \xi^2} + (1-\eta)e^{-1/u} - \gamma_1 (u - u_2) \tag{4}$$

$$\frac{\partial u_2}{\partial \tau} = \alpha_0 \frac{\partial^2 u_2}{\partial \xi^2} + \gamma_2 (u - u_2) \tag{5}$$

$$\frac{\partial \eta}{\partial \tau} = \beta (1-\eta) e^{-1/u} \tag{6}$$

where $\alpha_0 = \frac{\alpha_2}{\alpha}$, $\gamma_1 = \frac{4 d_N}{d_M{}^2 - d_N^2} \frac{G_0 \beta M_W}{\rho C_p k_0}$, and $\gamma_2 = \frac{4 G_0 \beta M_{W2}}{d_N \rho_2 C_{p,2} k_0}$. Interestingly, this shows that the only terms affected by the diameter of the thermal conduit or the fuel layer are the interfacial heat exchange terms, γ_1 and γ_2. We have demonstrated with previous modeling work[20, 21] that γ_1 and γ_2 do not affect the propagation of the reaction wave for values above 10^{-3} (corresponding to $G_0 > 10^5$ W/m^2/K); axial thermal transport within the nanotube becomes the limiting factor compared to interfacial conductance. By comparison, the simulations in this chapter used values on the order of 10^3, so diameters have little effect to first order. A central motivation for this work is the fact that oscillatory behavior has been observed in similarly driven, Fourier conduction systems;[23, 27-30] hence we ask if thermopower waves can likewise demonstrate regions of parameter space where oscillations are possible.

For β, α, and α_2, average values over the temperature range of 300 to 1700 K were used. Since β is the non-dimensionalized adiabatic reaction temperature rise, the maximum temperature was iterated until a consistent average β of 10.6 for TNA was reached. Likewise, for dimensional scaling of temperature, we used TNA's activation energy of 127 kJ/mol.[31] Over the same temperature range, α is 4.3×10^{-8} m^2/s, and α_2 is 0.001 m^2/s. Depending on the concentration of defects, the thermal diffusivity of the nanotube, α_2, may at least vary over an order of magnitude. The value chosen here was the median. For all other parameters except k_0, values from the TNA and CNT literature were used.[18, 32-

40] The molecular weight of bulk TNA is 0.22212 kg/mol, its thermal conductivity [32] is 0.2783 W/m/K, and its density[33] is 1820 kg/m^3.

The parameter k_0 affects the scaling of both the reaction wave front velocity (henceforth referred to as velocity) and oscillation frequencies when they are converted from the non-dimensional solutions of equations (4)-(6) through the space and time scaling factors. The velocity and frequency depend on $k_0^{1/2}$ and k_0, respectively. Since k_0 is an *effective* Arrhenius constant, it can include mass and thermal diffusion limitations. We argue that the presence of the nano-conduit may reduce k_0 for the reacting material, TNA. While the MWNTs act as thermal conduits, kinetically they are inert, so their effect on k_0 may be more similar to that of a binder. Oyumi[41] measured k_0 in pure TNA to be 3.75×10^{18} s^{-1}, whereas Williams and Matei[31] found it to be 2.0×10^{11} s^{-1} in a TNA/binder mixture over the range of 180 to 225 °C. Consequently, in order to reproduce the reaction wave velocity in the range of 0.1 to 2 m/s, which was in agreement with the experiments, $k_0 = 3\times10^9$ s^{-1} was chosen. The validity of the choice was further conformed by the excellent agreement between the simulation and measurements signature frequencies, which will be described later.

4.3 Computational Methods

As with previous simulations,[20] we solved equations (1), (2) and (3) using the COMSOL Multiphysics software package with adaptive time steps and at various spatial mesh sizes (8 to 250 nm) over lengths of 2 to 5 mm to check for convergence. The diameter of the nanotube was 22 nm and the surrounding fuel annulus was 7 nm thick, matching the physical system used in this chapter. The amplitude of the initial pulse could be varied by at least 50% without affecting the solution when a nanotube was present. As examples, the dimensional forms of two initial temperature conditions are calculated here. For $\beta = 4$, $g = 11{,}000$ K and $w = 8\text{x}10^{-11}$ m^2. For $\beta = 10.6$, $g = 124{,}000$ K and $w = 2.1\text{x}10^{-10}$ m^2. These pulses have a full width at half maximum of 15 and 24 μm, respectively.

The simulations were carried out for durations sufficient to observe steady waves with multiple periods of oscillation. A Matlab program extracted the temperature data and calculated velocity. Our previous modeling work has shown that convection does not significantly affect velocity in the TNA-CNT system, and that averaging property values such as thermal conductivity, enthalpy of reaction, and specific heat over an appropriate temperature range results in agreement with simulation using temperature-dependent parameters.[20]

4.4 Simulated Wave Velocity Oscillations

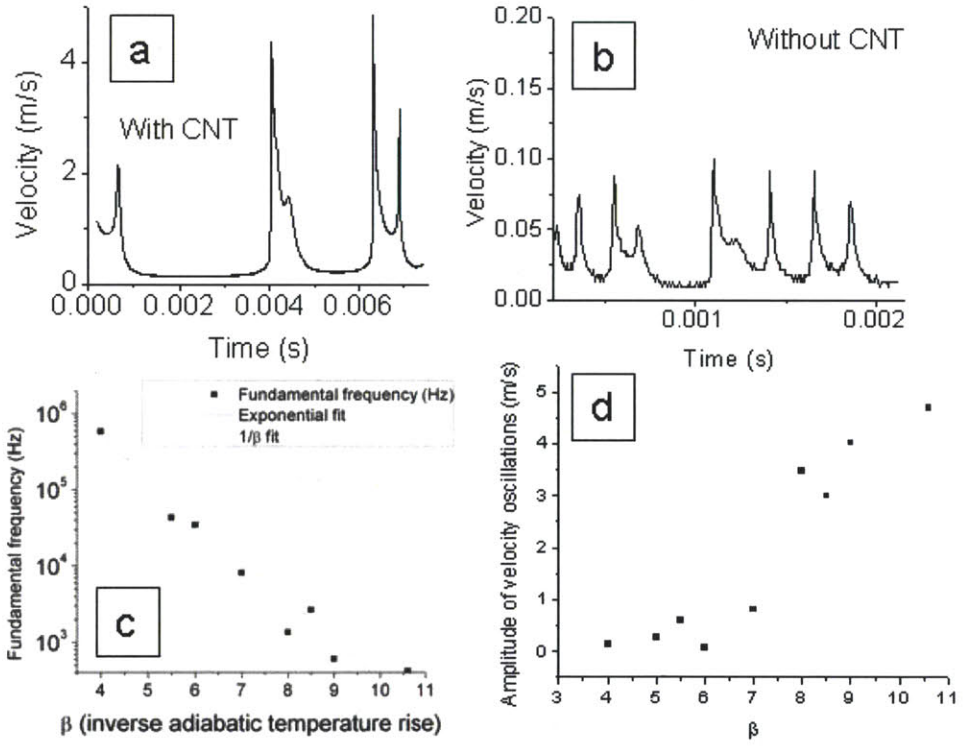

Figure 2: Simulation of the wave front velocity using β=10.6, α = 4.3×10^{-8} m^2/s, and α_2 = 0.001 m^2/s, with a length of 5 mm. The diameter of the nanotube was 22 nm and the surrounding fuel annulus was 7 nm thick. (b) Simulated velocity for the same parameters with no nanotube (α_2 = 0). (c) Fundamental frequency variation with β. The relation is inverse and stronger than simple dimensional scaling (1/θ) would suggest. (d) Amplitude of oscillations for different θ values. Amplitudes are small and relatively constant for θ < 7.

Simulations predict velocity oscillations for the TNA-CNT system. Figure 2a shows the velocity profile, beginning at t = 0.2 ms in order to see the steady-state responses after the initial period, which is more strongly influenced by the initial condition. Velocity is calculated by tracking the position of the point on the reaction temperature profile where non-dimensional temperature is $1/(2\beta)$, which corresponds to 700 K. The average velocity is 0.56 m/s, although the amplitude of the oscillations is as large as 4.7 m/s. The oscillations are not simply sinusoidal, but rather exhibit multiple components at different phase shifts. The mode velocity measured in our previous thermopower experiments was approximately 0.2 m/s,[20] so the simulation agrees reasonably well with our measurements. The over-prediction is likely due to the adiabatic conditions of the simulation, particularly the exclusion of radiation, which will be further explored in future work.

Including a nanoscale thermal conduit increases the average velocity. The simulated velocity for TNA reacting without CNT thermal conduits is shown in Figure 2b. With no conduit, velocity is on average 0.031 m/s, and the amplitude of oscillations is 0.088 m/s. Including a nano-conduit of α_2 = 0.001 m^2/s increases the average velocity by a factor of 18 and amplitude by a factor of 53. The rapid thermal transport in the thermal conduits affects the wave front non-linearly; they accelerate the reaction wave more when it is moving quickly than when it is moving slowly.

The presence of CNT thermal conduits also decreases the fundamental frequency, as measured by Fourier transforms (FTs) of the velocity profiles. We note that our simulation predicts frequencies on the order of kilohertz. For β = 10.6, the fundamental frequency decreases from 2350 to 420 Hz after the addition of a thermal conduit, compared to the case without one (Figure 2a,b). This is proportionately smaller than the increase in velocity. It could be that the non-uniform velocity acceleration from the conduits depletes the total energy of the reacting system such that it then takes more time for energy to build up to enable another rapid propagation phase. Future work will develop comprehensive steady-

state and transient reactive wave theories that will expand upon these results, but such developments are outside of the scope of this work.

The frequency of these velocity oscillations is inversely related to β, but the dependence is stronger than $1/\beta$, which is what would be expected if it were only due to the time dimensional scaling, $t = \left(\frac{\beta}{k_o} \right) \tau$. Figure 2c shows the fundamental frequencies for different β values. As with many properties of the reaction wave, the relation to β appears to be an inverse exponential of the form $Ae^{-Z\beta}$, where A is 6.9×10^7 Hz and Z is 1.23 for the best fit to the simulation results. These simulation results indicate that we may be able to control oscillation frequencies in actual devices by using fuels with different properties, corresponding to different β values.

The amplitude of oscillations also depends on β, but not inversely, as frequency and average velocity do, as can be seen in Figure 2d. For $\beta < 7$, velocity oscillations are so small as to be inconsequential (although they have well-defined frequencies). Above that point, the relationship is approximately linear; velocity oscillation amplitude increases even as the average velocity is decreasing. This is consistent with the idea that CNT thermal conduits accelerate the reaction wave more when it is moving faster.

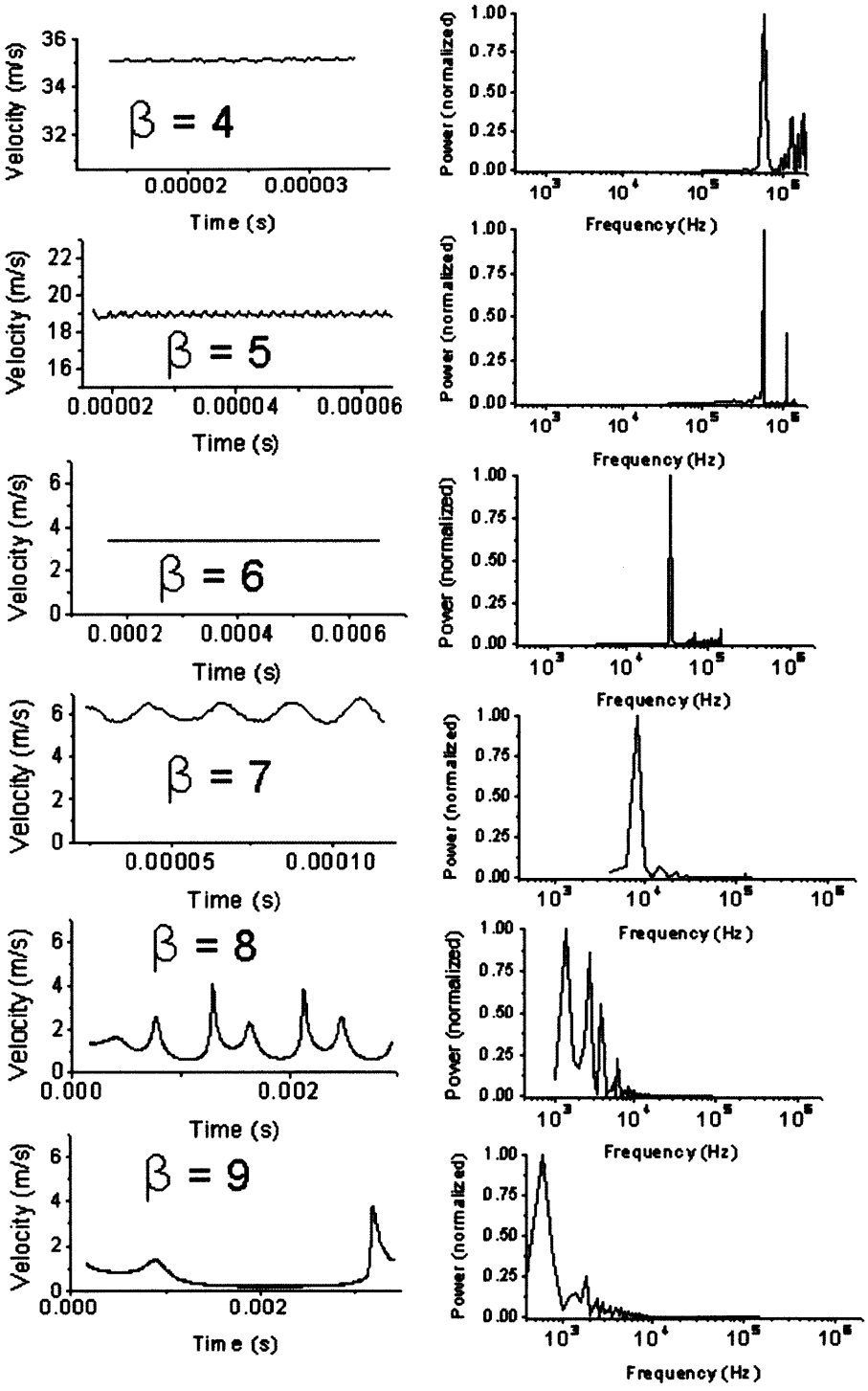

Figure 3: Wave front velocity profiles and frequency spectra for $4 < \beta < 9$. As β increases, so does the amplitude of the oscillations, and for $\beta > 7$ they begin to take on additional structure and complexity. Stronger secondary peaks in the frequency spectra arise at the same point.

The value of β defines two distinct propagation regimes related to oscillations. Figure 3 shows velocity profiles and frequency spectra for $4 < \beta < 9$ at a constant value of $\alpha_2 = 0.001$ m^2/s. Although the average steady-state velocity decreases roughly exponentially from 35 to 0.56 m/s as β increases from 4 to 10.6, the change in oscillations is more complex and transitions from very low amplitude, almost constant velocity profiles to significant oscillations, often with multiple frequency components. This transition occurs between $\beta = 6$ and 7 and is also marked by the appearance of stronger secondary peaks and harmonics in the frequency spectra. Furthermore, we observe a local minimum in average velocity at $\beta = 6$, which coincides with the transition between propagation regimes. For $\beta > 8$, the velocity oscillations are interspersed with regions of very low, nearly constant velocity.

4.5 Convergence Tests for Oscillation Simulations

Within the oscillating region, as β becomes larger the reaction wave front moves more slowly and its period of oscillation becomes longer (the fundamental frequency becomes smaller), resulting in two adjustments. Both total simulation time and length of the spatial domain (ξ) need to be increased manually within COMSOL in order to observe the oscillations. With the larger period, it is not necessary to keep time steps as small as those for smaller β values. For example, $\beta = 5$ might have a time step of 200 (non-dimensional) to a final time of 50,000 while $\beta = 9$ might only need a time step of 500, but need a longer final time of 300,000. "Intermediate" adaptive time-stepping within COMSOL allows the program to calculate solutions at other time points in addition to the specified times to improve numerical stability. However, as the specified time step is made larger, the adaptive steps taken by COMSOL are not as precise, often resulting in an inability to converge a solution. In this event, the size of the specified time steps must be reduced to achieve converged results.

When simulating reaction wave behavior, it is fundamental to verify the accuracy of results, particularly in the oscillating velocity region where a single average solution is insufficient and the

equations are somewhat unstable. In COMSOL, mesh size, here denoted $\Delta\xi$, is the (non-dimensional) size of the finite spatial element over which the model equations are solved numerically. As mesh size is reduced, the precision of the velocity calculation improves; however, the value of the ratio $\frac{\Delta\tau}{\Delta\xi^2}$ increases and, at some point, exceeds the stability criterion of the diffusive heat transport equation. The resulting numerical solution is then incompletely converged and thus inaccurate. With its adaptive time-stepping algorithm, COMSOL can change $\Delta\xi$ to maintain stability during the simulations, but at a price to computation time and memory usage. Therefore, only a certain range of $\Delta\xi$ is practical and accurate for this system.

Within this range, results do not significantly change with mesh size. We simulated reaction for the same β value for $1 < \Delta\xi < 20$ and compared the resulting velocity profiles and frequency. This procedure was repeated for multiple values of β, primarily for those at the boundaries of the oscillating regime and for a few in the middle in order to ensure that they had similar ranges of convergence.

As an example, frequency spectra are shown in Figure 4 for $\beta = 7$ at $\Delta\xi = 1$, 2, 3, 5, and 10. A nearly identical peak can be seen at 8100 Hz for the last three mesh sizes. The slightly less precise peak for $\Delta\xi = 10$ indicates the upper edge of the range of convergence, above which the velocity calculation is insufficiently precise to produce a similar spectrum. For $\Delta\xi < 3$, the frequency spectrum changes dramatically and with no discernable pattern with each finer mesh, signifying that the numerical solution has become unstable.

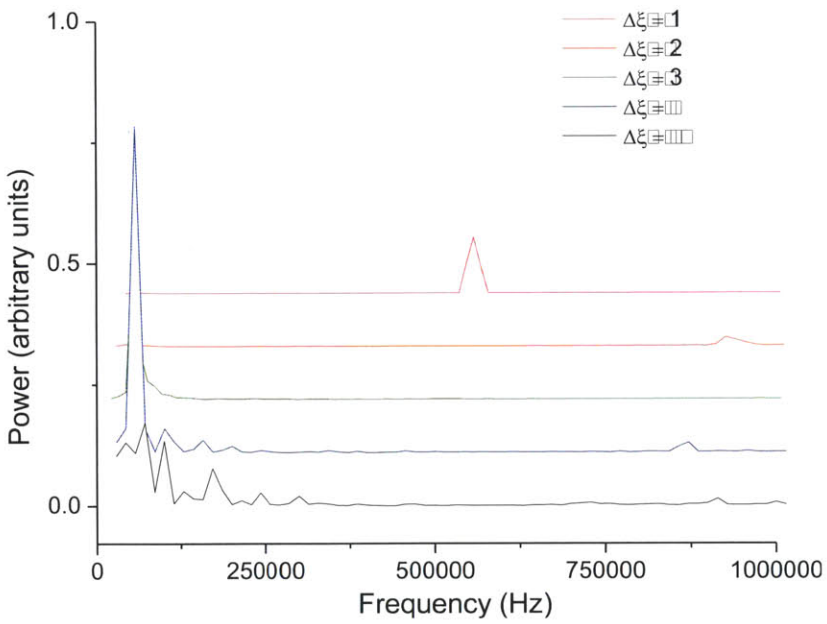

Figure 4: Frequency spectra for $\beta = 7$ at different mesh sizes

Another revealing comparison for the same simulations can be seen in the velocity profiles, plotted in Figure 5. In the middle graph, as $\Delta\xi$ is increased, the start-up time (before the onset of repeated oscillations) fluctuates because the model PDEs are applied over larger discretized segments along the geometry. Thus while the overall period of oscillation is the same (as evidenced by Figure 4), these profiles appear slightly different due to the different times at which the reaction wave begins to move steadily along the carbon nanotube. If a slight phase shift to the left is applied to the $\Delta\xi = 5$ and 10 profiles, all the oscillations very closely match, mirroring the likeness of frequency peaks from Figure 4 above.

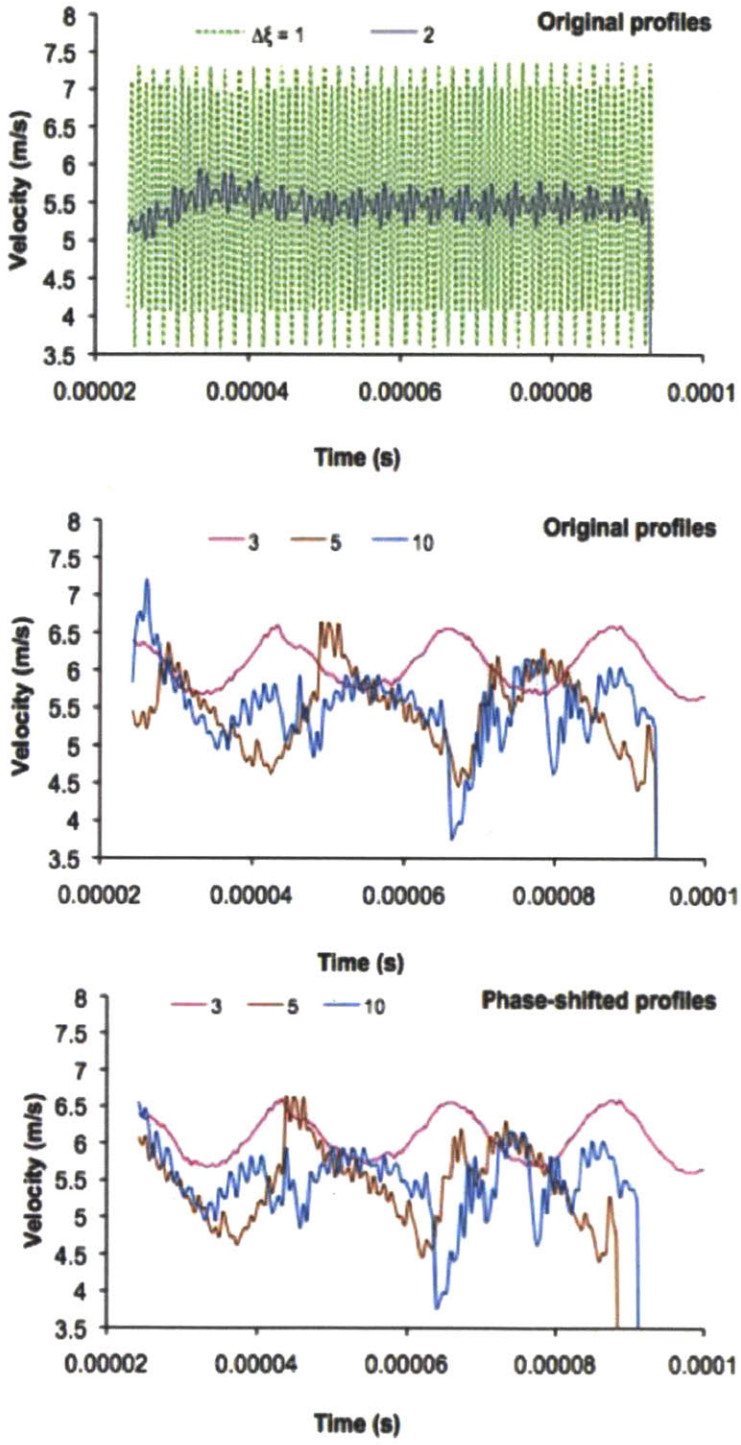

Figure 5: Velocity profiles for θ = 7 at $\Delta\xi$ = 1, 2, 3, 5, and 10. Top, middle: original plots; Bottom: Plot with slight phase shift of $\Delta\xi = 5$ and 10 to the left.

This is confirmed by a comparison of $\Delta\xi = 3$ and 5. As with the frequency spectra, the velocity profiles for $\Delta\xi = 1$, 2, and 10 have greater error, identifying the bounds of convergence.

4.5 Experimental Sample Preparation

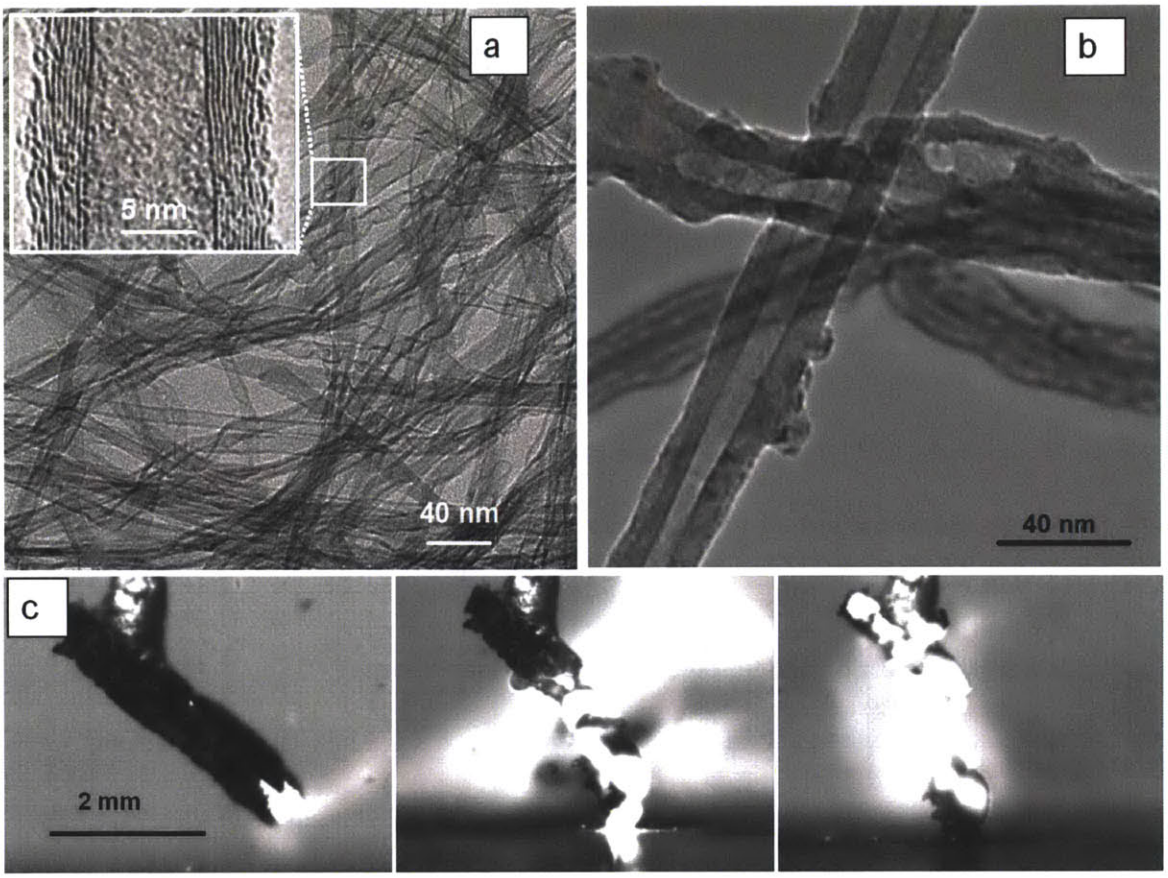

Figure 6: (a) TEM images of MWNTs and (b) TNA-MWNTs after dispersion. (c - left to right) Reaction front photos using a high-speed camera. The length of the TNA-MWNTs is ~3 mm.

For our experiments, we synthesized vertically aligned multi-walled carbon nanotubes (MWNTs) using chemical vapor deposition in a horizontal quartz tube furnace with Fe and Al_2O_3 catalytic layers. Ethylene (C_2H_4), hydrogen, and argon were the carbon source, catalytic and carrier gases, respectively.[42] To coat the MWNT arrays, 200 mg TNA was dissolved in 10 mL acetonitrile and filtered.

This solution was dropped on the arrays and then evaporated under atmospheric conditions for several hours, coating the nanotubes. NaN_3 in aqueous solution (50 mg/mL) was then added to serve as a primary igniter to lower activation energy (40 kJ/mol for NaN_3, in contrast to 127 kJ/mol for TNA). Silver paste was used to make electrical connections between the TNA-MWNT samples and copper tape electrodes. Their resistance ranged from 10 to 100 Ω depending on the size of the TNA-MWNT bundle. Over 100 samples of different masses were prepared and tested, as reported previously.[20]

Vertically aligned MWNTs served as the thermal conduits for the thermopower wave experiments. Figure 6a shows transmission electron micrographs (TEM) of the MWNTs after dispersion. They have, on average, an outer diameter of 22 nm, an inner diameter of 14 nm, and ten walls. The arrays of these MWNTs were 3 to 5 mm tall with porosity of approximately 99% prior to the addition of TNA. Figure 6b shows the MWNTs after they have been coated with TNA; the continuous annuli are on average 7 nm thick and do not disrupt the MWNTs structurally.

4.6 Thermopower Wave Testing and Voltage Oscillation Observations

The samples were ignited at one end of the bundles with a 400 mW laser of wavelength 785 nm. The propagation of the reaction front was measured optically using a high speed CCD camera (CPL-MS70K, Canadian Photonic Labs) with a microscopic lens (Macro 60 mm, f/2.8D micro Nikkor Autofocus lens, Nikon) at up to 90,000 frames per second. Thermal reaction waves propagated rapidly along the aligned MWNT arrays, as depicted in Figure 6c.

The accelerated reaction wave drives a concomitant wave of electrons, which also exhibits oscillations in voltage. As an example, Figure 7 shows voltages measured with an oscilloscope across two samples of different masses (0.2 and 3 mg). Large temperature gradients generate voltages with peak magnitudes in the range of 20 to 150 mV. Oscillations modulated this voltage with amplitudes in the

range of 2 to 20 mV. The maximum specific power exceeded 7 W/g for smaller mass samples, which is substantially larger than that of high-performance Li-ion batteries.

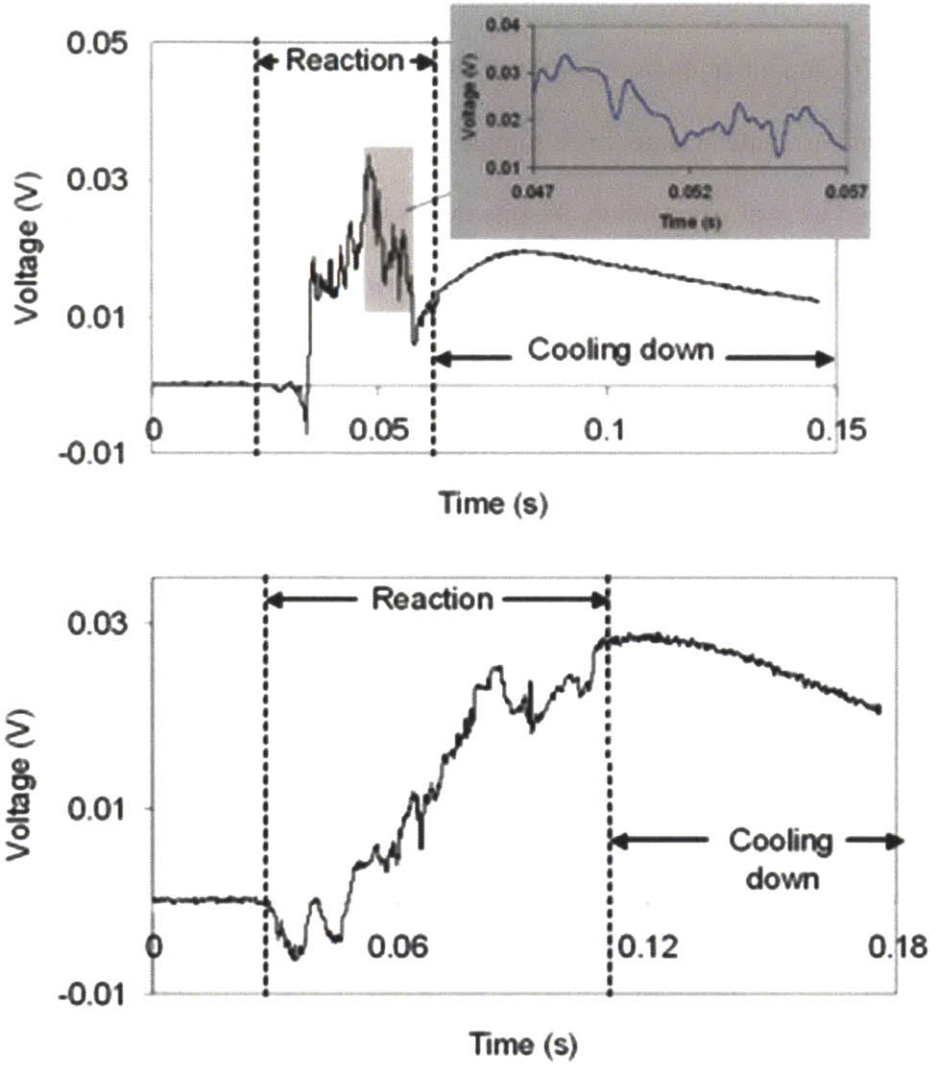

Figure 7: Thermopower voltage signals in reaction (oscillation) and cooling zones for (top) a small (0.2 mg) and (bottom) a large mass (3 mg) sample of TNA-MWNTs. The form is very similar, regardless of mass, except that the reaction time is longer for the larger mass sample.

The voltage profiles in Figure 7 can be divided into two phases: an oscillating reaction phase and a smooth cooling phase. Comparison between high-speed video and the electrical signals shows that the oscillation phase corresponds to the time the reaction waves are propagating. The shape of the voltage profiles appears to depend on the sample mass: the larger the mass, the longer the oscillation phase. The longer voltage rise time in larger mass samples can be ascribed to slower reaction orthogonal to the MWNTs compared to axial propagation. Despite their very large axial thermal conductivity,[43] MWNT arrays' radial thermal conductivities are very low. In a TNA-MWNT system with TNA layers only a few nanometers thick and nanotube wall spacing of less than 1 nm, as well as large voids between nanotubes, phonon scattering in radial directions is substantial.[44]

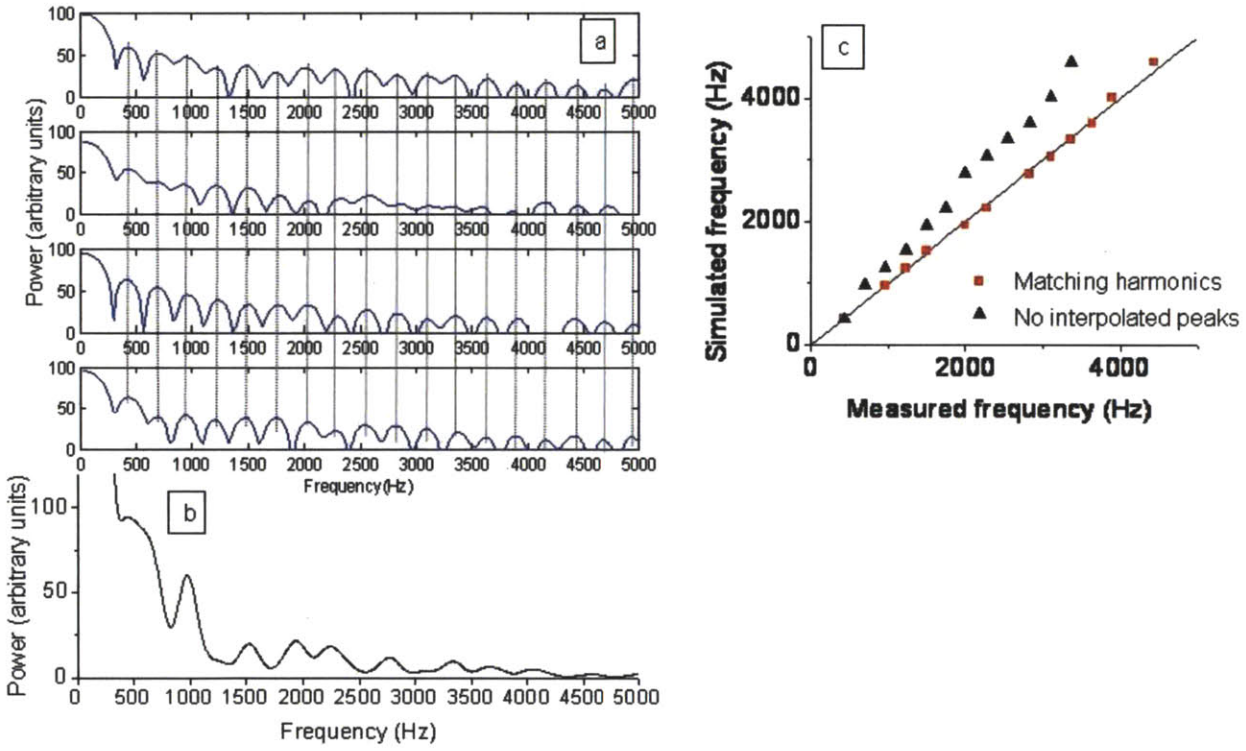

Figure 8: (a) Frequency signatures of reaction region of voltage signals of four samples with different masses (top to bottom: 0.2, 0.9, 1.5 and 3 mg). The dotted lines show the signatures' agreement. Distinct frequency peaks are observed at 430, 700, 960, ... and 4960 Hz. (b) Fourier transform of the simulated velocity. Frequency peaks appear at 420, 970, 1250, ... and 4590 Hz. (c) Parity plot showing agreement between frequency peaks from velocity simulations and voltage measurements. The parameter changing between points is the number of the frequency peak. The agreement improves by matching the harmonics in the two spectra.

In agreement with our simulations, the voltage oscillations spectrum measured likewise covers the frequency range of 0-5000 Hz. The Fourier transforms of voltage signals from the oscillating reaction phases of four different samples of different masses are shown as examples in Figure 8a. Approximately 40% of all samples had similar frequency signatures, whereas the remainder did not exhibit that pattern. The broad peak around zero frequency extends out to 330 Hz. In addition, there are distinct oscillation peaks at 430, 700, 960, 1230, 1490, ... and 4960 Hz. Except for the first two peaks, the peaks are equally spaced by ~260 Hz. These samples came from three different MWNT arrays, had varying cross-sectional areas and masses, and their densities varied up to 20%. But interestingly, they all show similar frequency signatures. Since the same CVD process produced all samples, the MWNT diameter is consistent between samples (as confirmed by TEM), and thus the (per nanotube) thermal diffusivity is similar between samples.

As can be seen in Figure 8b, the FT of the graph of simulated velocity (Figure 2a) has frequency peaks at very similar positions. Some of these peaks are harmonics that have been broadened and shifted due to noise or finite sampling time, but the velocity oscillations also have multiple fundamentals. The peaks appear at 420, 970, 1250, 1530, ... and 4590 Hz, intervals of ~300 Hz, although not all peaks experimentally observed appear in the simulation.

The parity plot in Figure 8c demonstrates the agreement between the frequencies of the calculated velocity oscillations at $\beta = 10.6$ and the frequencies observed in the experimental voltage oscillations. A simple pairing of fundamental peaks and higher harmonics yields less than a 4% error between the simulated and experimental frequencies, corresponding to the "matching harmonics" data set. There appear to be peaks in the experimental FTs that are not reproduced in the simulated frequencies, for example at 700, 1750 and 2540 Hz. If one instead assumes that *all* peaks experimentally observed constitute the harmonics, the error is larger at 20 to 40%, corresponding to the

"no interpolated peaks" data set. There is sufficient evidence to support the former analysis (*i.e.* matching up harmonics). A careful examination of the FT in Figure 8b shows that the 700 Hz harmonic forms the "shoulder" of the 420 Hz peak, and the magnitude of higher frequency harmonics may not be intense enough to detect above the spectrum background. Note that the points in the parity plot are parametric in the numerical order of each peak. With either comparison, however, it is clear that there are discretized frequencies predicted by the Fourier analysis and observed experimentally. This supports the accuracy of the mathematical model, which predicts both average velocity (Figure 2a), 0.56 m/s, as well as the frequency of oscillations. Average velocities measured in thermopower experiments ranged from 0.05 to 1.35 m/s, and a range of values of β and α_2 could reproduce these.[20] It is notable, therefore, that the results of simulations using $\beta = 10.6$, $\alpha_2 = 0.001$ m^2/s, and $k_0 = 3\times10^9$ s^{-1} agreed well with measurements of velocity, as well as with the frequency spectrum of voltage oscillations.

4.7 Implications of Oscillations for the Seebeck Effect in Thermopower Waves

The parity between the frequencies of the velocity oscillations and the induced voltage implies that the wave velocity is the dominant factor in driving the current along the device. In the limit of conventional, steady state thermopower (where wave velocity has no influence) the produced voltage, *V*, is based on the temperature difference alone:

$$V = \kappa\left(T_{rxn} - T_{ambient}\right) \tag{7}$$

Here κ is the Seebeck coefficient and T_{rxn} is the reaction temperature. Note that this expression possesses a Fourier transform that necessarily integrates to zero, since T_{rxn} is approximately constant. The fact that V instead has a non-zero Fourier transform, related to the oscillations of the physical wave front, supports the existence of a velocity component to the generated thermopower. This concept of a velocity component is consistent with our previous observations that samples producing larger velocity (evident in smaller mass samples, for example) generate higher specific power. The origin of the

velocity component is currently under investigation, but one physical picture that is suggestive is that of a carrier entrainment that accompanies the wave propagation. Electron-phonon coupling in nanoscale systems is known to be enhanced, with carbon nanotubes being no exception.[45] One can calculate an order-of-magnitude estimate of such an entrainment current, *J*:

$$J = \frac{V}{R_e} = n \cdot A \cdot v \cdot e \tag{8}$$

where R_e is the resistance of the bundle, *n* is the carrier density of one CNT, *A* is the cross-sectional area of the bundle, and *e* is the elementary charge, and *v* remains the thermopower wave velocity. For a typical current observed from systems experimentally tested to date (0.1 – 1 mA) we calculate a linear carrier density, *nA*, of 0.6 to 6×10^{16} carriers/m, or 0.6 to 6 carriers per nm of nanotube, since there are about 10^7 nanotubes per sample. Given the size of a typical CNT unit cell (< 1 nm) this estimate is reasonable.

In summary, we have both experimentally and theoretically investigated the behavior of the thermopower wave micro-generator. MWNT conduits axially accelerate the highly exothermic decomposition of TNA, generating voltage and current. The maximum DC specific power of the thermopower wave system exceeds 7 W/g, which is larger than any generated by current Li-ion batteries. The system also shows strong auto-oscillatory behavior, described by chemical reaction and heat transfer equations and suitable boundary conditions, and these equations can accurately reproduce measured frequency signatures in the range of 0.4 to 5 kHz. This system represents a new class of micro-scale power sources for applications in which very large power densities are required within limited space.

References

1. van den Berg, A.W.C. and C.O. Arean, *Materials for hydrogen storage: current research trends and perspectives.* Chemical Communications, 2008(6): p. 668-681.
2. Simon, P. and Y. Gogotsi, *Materials for electrochemical capacitors.* Nature Materials, 2008. **7**(11): p. 845-854.
3. Qin, Y., X.D. Wang, and Z.L. Wang, *Microfibre-nanowire hybrid structure for energy scavenging.* Nature, 2008. **451**(7180): p. 809-813.
4. Song, J.H., J. Zhou, and Z.L. Wang, *Piezoelectric and semiconducting coupled power generating process of a single ZnO belt/wire. A technology for harvesting electricity from the environment.* Nano Letters, 2006. **6**(8): p. 1656-1662.
5. Mor, G.K., et al., *A review on highly ordered, vertically oriented TiO2 nanotube arrays: Fabrication, material properties, and solar energy applications.* Solar Energy Materials and Solar Cells, 2006. **90**(14): p. 2011-2075.
6. Shao, Z.P., et al., *A thermally self-sustained micro solid-oxide fuel-cell stack with high power density.* Nature, 2005. **435**(7043): p. 795-798.
7. Strasser, M., et al., *Micromachined CMOS thermoelectric generators as on-chip power supply.* Sensors and Actuators a-Physical, 2004. **114**(2-3): p. 362-370.
8. Mitcheson, P.D., et al., *Energy harvesting from human and machine motion for wireless electronic devices.* Proceedings of the Ieee, 2008. **96**(9): p. 1457-1486.
9. Arnold, D.P., *Review of microscale magnetic power generation.* IEEE Transactions on Magnetics, 2007. **43**(11): p. 3940-3951.
10. Cook, B.W., S. Lanzisera, and K.S.J. Pister, *SoC issues for RF smart dust.* Proceedings of the IEEE, 2006. **94**(6): p. 1177-1196.
11. Cook-Chennault, K.A., N. Thambi, and A.M. Sastry, *Powering MEMS portable devices - a review of non-regenerative and regenerative power supply systems with special emphasis on piezoelectric energy harvesting systems.* Smart Materials & Structures, 2008. **17**(4): p. 043001.
12. Kerzenmacher, S., et al., *Energy harvesting by implantable abiotically catalyzed glucose fuel cells.* Journal of Power Sources, 2008. **182**(1): p. 1-17.
13. Yager, P., et al., *Microfluidic diagnostic technologies for global public health.* Nature, 2006. **442**(7101): p. 412-418.
14. Klauk, H., et al., *Ultralow-power organic complementary circuits.* Nature, 2007. **445**(7129): p. 745-748.
15. Zadeh, A.E. *Nano-power Switched-Capacitor Bandpass Filters for Medical Implantable Pacemakers and Defibrillators*. in *IEEE 2008 51st Midwest Symposium on Circuits and Systems, Vols 1 and 2*. 2008.
16. Pillai, V., et al., *An ultra-low-power long range battery/passive RFID tag for UHF and microwave bands with a current consumption of 700 nA at 1.5 V.* IEEE Transactions on Circuits and Systems I-Regular Papers, 2007. **54**(7): p. 1500-1512.
17. Ottino, J.M. and S. Wiggins, *Introduction: mixing in microfluidics.* Philosophical Transactions of the Royal Society of London Series a-Mathematical Physical and Engineering Sciences, 2004. **362**(1818): p. 923-935.
18. Kim, P., et al., *Thermal transport measurements of individual multiwalled nanotubes.* Physical Review Letters, 2001. **8721**(21): p. 215502-215505.
19. Yu, C.H., et al., *Thermal conductance and thermopower of an individual single-wall carbon nanotube.* Nano Lett., 2005. **5**(9): p. 1842-1846.
20. Choi, W., et al., *Chemically Driven Carbon Nanotube-Guided Thermopower Waves.* Nature Materials, 2010. **9**: p. 423-429.

21. Abrahamson, J.T., N. Nair, and M.S. Strano, *Modelling the increase in anisotropic reaction rates in metal nanoparticle oxidation using carbon nanotubes as thermal conduits.* Nanotechnology, 2008. **19**(19): p. 195701-195708.
22. Xin, J., *Front propagation in heterogeneous media.* Siam Review, 2000. **42**(2): p. 161-230.
23. Weber, R.O., et al., *Combustion waves for gases (Le=1) and solids (L->infinity).* Proceedings of the Royal Society of London Series a-Mathematical Physical and Engineering Sciences, 1997. **453**(1960): p. 1105-1118.
24. Kolmogorov, A.N., I.G. Petrovsky, and N.S. Piskunov, *Etude de l'e´quation de la diffusion avec croissance de la quantit´e de mati`ere et son application `a un prob l `eme biologique, .* Moskow Univ. Math. Bull., 1937 **1**: p. 1-25.
25. Fisher, R.A., *The wave of advance of advantageous genes.* Annals of Eugenics, 1937. **7**: p. 355-369.
26. Zel'dovich, Y.B. and D.A. Frank-Kamenetskii, *The theory of thermal flame propagation.* Zh. Fiz. Khim., 1938. **12**: p. 100-105.
27. Zeldovich, Y.B., O.I. Leypunsky, and V.B. Librovich, *Theory of non-steady powder combustion*1975, Moscow: Izdak. Nauka
28. Bayliss, A. and B.J. Matkowsky, *FROM TRAVELING WAVES TO CHAOS IN COMBUSTION.* Siam Journal on Applied Mathematics, 1994. **54**(1): p. 147-174.
29. Shkadinskii, K.G., B.I. Khaikin, and A.G. Merzhanov, *Propagation of a pulsating exotermic reaction front in condensed phase.* Combustion Explosion and Shock Waves, 1971. **7**(1): p. 15-22.
30. Merzhanov, A.G., A.K. Filonenko, and Y.A. Borovinska, *New phenomena in combustion of condensed systems.* Doklady Akademii Nauk SSSR, 1973. **208**(4): p. 892-894.
31. Williams, M.R. and M.V. Matei, *The decomposition of some RDX and HMX based materials in the one-dimensional time to explosion apparatus. Part 1. Time to explosion and apparent activation energy.* Propellants Explosives Pyrotechnics, 2006. **31**(6): p. 435-441.
32. Parr, T. and D. Hanson-Parr, *RDX ignition flame structure.* Twenty-Seventh Symposium (International) on Combustion, Vols 1 and 2, 1998: p. 2301-2308.
33. Li, S.C., F.A. Williams, and S.B. Margolis, *Effects of 2-Phase Flow in a Model for Nitramine Deflagration.* Combustion and Flame, 1990. **80**(3-4): p. 329-349.
34. Oyumi, Y., *Melt phase decomposition of RDX and two nitrosamine derivatives.* Propell. Explos. Pyrot., 1988. **13**: p. 42-47.
35. Liau, Y.C., E.S. Kim, and V. Yang, *A comprehensive analysis of laser-induced ignition of RDX monopropellant.* Combust. Flame, 2001. **126**(3): p. 1680-1698.
36. Volkov, E.N., A.A. Paletsky, and O.P. Korobeinichev, *RDX flame structure at atmospheric pressure.* Combust. Explo. Shock., 2008. **44**(1): p. 43-54.
37. Richard E. Sonntag, G.J.V.w., *Introduction to thermodynamics: classical and statistical.* 3rd ed ed. 3rd ed., John Wiley & Sons1991: John Wiley & Sons.
38. Li, C.Y. and T.W. Chou, *Modeling of elastic buckling of carbon nanotubes by molecular structural mechanics approach.* Mechanics of Materials, 2004. **36**(11): p. 1047-1055.
39. Begtrup, G.E., et al., *Probing nanoscale solids at thermal extremes.* Physical Review Letters, 2007. **99**(15): p. 155901-155904.
40. Li, C.Y. and T.W. Chou, *Quantized molecular structural mechanics modeling for studying the specific heat of single-walled carbon nanotubes.* Physical Review B, 2005. **71**(7): p. 075409-075414.
41. Oyumi, Y., *Melt phase decomposition of rdx and two nitrosamine derivatives.* Propellants, Explosives, Pyrotechnics, 1988. **13**(2): p. 42 - 47.
42. Xu, Y.Q., et al., *Effects of atomic hydrogen and active carbon species in 1 mm vertically aligned single-walled carbon nanotube growth.* Applied Physics Letters, 2006. **89**(12): p. 123116-123118.

43. Mingo, N. and D.A. Broido, *Carbon nanotube ballistic thermal conductance and its limits.* Physical Review Letters, 2005. **95**(9).
44. Chen, G., *Thermal conductivity and ballistic-phonon transport in the cross-plane direction of superlattices.* Physical Review B, 1998. **57**(23): p. 14958-14973.
45. Pop, E., et al., *Negative differential conductance and hot phonons in suspended nanotube molecular wires.* Physical Review Letters, 2005. **95**(15): p. 155505-155508.

Chapter 5

Thermopower Waves on Nitrobenzene-Functionalized Single-Walled Carbon Nanotubes

5.1 Nanostructured Fuels and Energetic Materials

Engineering materials at the nanometer scale has enabled new technologies, particularly in the area of energy storage and release[1-4]. Nanostructured fuels benefit from increased surface areas, enhancement of chemical reactivity and transport properties, and the ability to form nanocomposites.[5, 6] Nanoenergetic materials[7] may overcome many limitations of conventional energetic materials, for example, incomplete combustion when diffusive mass transport limits reaction.[8] By applying molecular-scale design principles, the energy density of engineered nanoenergetic materials can be increased compared to conventional materials.[7] A particularly interesting case is an exothermic chemical reaction coupled to a highly thermally conductive nano-conduit. For instance, our group recently demonstrated through modeling, as a proof-of-concept, that reaction rates are accelerated anisotropically when a single-walled carbon nanotube (SWNT) is thermally coupled to a metal oxidation reaction surrounding it in an annulus of fuel.[9] In case of Zr metal, reaction velocity increased from 530 to 5100 mm/s in the direction of the nanotube's length. One-dimensional (1-D) nanoenergetic materials such as these may find new interesting applications such as novel propellants and high-energy materials synthesis by focusing energy at the nanoscale.

Experimental endeavors in our group have resulted in the discovery of a new concept for the conversion of chemical energy to electricity: thermopower waves.[10-12] Using 7-nm shells of energetic

material around carbon nanotubes, which have very high axial thermal conductivity, a reaction wave can self-propagate along the length, at a rate amplified by more than 10^4 times the bulk value. Most importantly, this reaction wave produces a concomitant thermopower wave of high power density (>7 W/g), resulting in an electrical current along the same direction. The thermopower wave is generated *via* entrainment of charge carriers by self-sustaining reaction waves in a system where an exothermic fuel is thermally coupled to an anisotropic heat conductor. This emerging concept is expected to overcome the limitations of traditional thermoelectricity and may find use in many unique nanoscale energy sources. Nor is the phenomenon limited to carbon nanotubes; Walia *et al.* recently demonstrated thermopower waves using nitrocellulose as the fuel and a thin film of Bi_2Te_3 sputtered on alumina as the electrical and heat conductors, respectively.[13] Thus, thermopower waves can be realized in layered geometries as well.

Creating new classes of nanoenergetic materials with low dimensionality also stirs interest in the field. One approach is covalently decorating energetic molecules around a nanotube or nanowire, as a 1-D heat conductor (Figure 1). Energy from the chemical reaction at the one end may propagate through the 1-D conductor, initiating reactions in the attached molecules at the propagating wave front. Several questions define the performance and function of such systems: (1) how much energy can be stored and released, and how fast can it occur? (2) Are tunable 1-D nanoenergetic materials possible (for example, SWNTs decorated with mono-, di-, or trinitroaromatics)? (3) After initiation of a reaction in the system, can the reaction wave self-propagate? (4) Can the system support thermopower waves? If so, what are the effects of covalent functionalization of the thermal/electrical conduit? The answers to the above questions will further the understanding of thermopower waves.

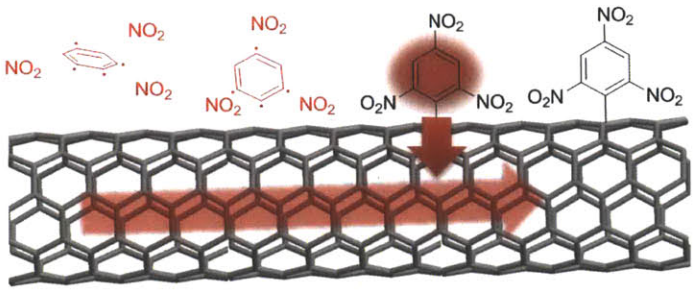

Figure 1. Schematic representation of reaction propagation on a single-walled carbon nanotube decorated with energetic molecules (trinitrobenzenes). Reprinted with permission from Reference [14] (courtesy of Changsik Song).

This chapter describes the synthesis of a series of nitrophenyl-decorated SWNTs using diazonium functionalization chemistry. These energetically decorated SWNTs are explored as a nanoscale energy source. Self-propagating reaction waves were launched on the covalently decorated nanoenergetic SWNTs to test thermopower wave generation.

5.2 Synthesis of Nitrophenyl-functionalized SWNTs

Source and Preparation of Materials: SWNTs were purchased from Unidym (Menlo Park, CA; high-pressure CO decomposition synthesis [HiPCO]), or from Nano-C (Westwood, MA; combustion-based synthesis). SWNTs were suspended at initial concentration ~0.4 g/L in Milli-Q water with 1% sodium dodecyl sulfate (SDS) as surfactant. Next, the suspension was homogenized for 1 h at 6500 rpm, sonicated in a cup-horn for 10 min at 90% power, and ultracentrifuged at 30000 rpm for 4 hrs to separate individual SWNTs from bundles. The solvent anhydrous acetonitrile (CH_3CN) was purchased from Aldrich in Sure-Seal Bottles and used as received. 4-nitroaniline and 2,4-dinitroaniline were purchased from Sigma-Aldrich (St Louis, MO), whereas 2,4,6-trinitroaniline was synthesized using Rosevear and Wilshire's procedure.[15] All other chemicals described were reagent grade and used as received.

As depicted in Scheme 1, mono-, di-, and trinitroaniline were diazotized to yield the corresponding diazonium salts. For 4-nitroaniline and 2,4-dinitroaniline, nitrosonium tetrafluoroborate ($NOBF_4$) in CH_3CN was sufficient for this reaction, and mono- and dinitrobenzenediazonium salts (MNP-$N_2^+BF_4^-$ and DNP-$N_2^+BF_4^-$, respectively) could be isolated as pure solids.[16] However, the additional nitro group of 2,4,6-trinitroaniline comparatively weakens its basicity,[17] so to diazotize it the strong acid nitrosylsulfuric acid was generated *in situ* adapting a method by Matsui and coworkers.[18] Although this reaction succeeded, the diazonium salt (TNP-$N_2^+HSO_4^-$) was still too unstable to survive purification, so the diazonium salt solution was used as prepared in subsequent steps.

Scheme 1. Synthesis of Nitrophenyl-SWNTs *via* Diazonium Reactions

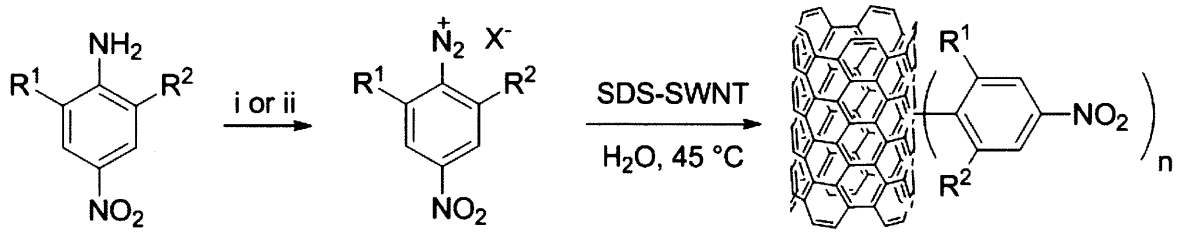

$X = BF_4^-$, $R^1 = R^2 = H$ **MNP-SWNT**

$X = BF_4^-$, $R^1 = H$, $R^2 = NO_2$ **DNP-SWNT**

$X = HSO_4^-$, $R^1 = NO_2$, $R^2 = NO_2$ **TNP-SWNT**

i) $NOBF_4$, acetonitrile, 0 °C, 4 h (for MNP- and DNP-SWNTs). ii) $NOHSO_4$ ($NaNO_2 + H_2SO_4$), H_2O, 25 °C, 3 h (for TNP-SWNTs).

Diazonium Functionalization of SWNTs with Nitrophenyls (NP-SWNTs): While stirring at 50 °C, nitrobenzenediazonium tetrafluoroborate (5 mM, 47 mg for mono- or 56 mg for dinitro-) was added incrementally to a suspension of SWNTs in SDS/H_2O (40 mL) over 2 h. For 2,4,6-trinitrophenyl-SWNTs, an acidic solution of TNP-$N_2^+HSO_4^-$ (5 mM, 0.2 mL) was added drop-wise over 2 h. The electron-rich SWNTs have a strong affinity for the electrophilic diazonium group, which is displaced as N_2 gas as the benzene ring forms a stable sp^3 bond to the SWNT sidewall.[19] The nitro groups are also electron-withdrawing,

so each one further increases the reactivity of the diazonium salt towards the SWNTs,[20] but also for other pathways. Thus, the stability of the diazonium salts decreases proportionally to the number of nitro groups (mono- < di- < tri-), and the SWNT functionalization reaction becomes less effective for an equimolar concentration of diazonium.

Another issue arises for stability of TNP-SWNTs: the strong acid destabilizes the SDS micelles suspending the SWNTs. Thus, the functionalization only proceeds so far before the TNP-SWNTs flocculate. To achieve a desired level of TNP functionalization, the flocculated TNP-SWNTs must then be filtered and re-dispersed with fresh SDS (aq) before repeating the functionalization.

After reaction, the mixture cooled to room temperature, then 40 mL acetone was added to ease filtration through a PTFE membrane. After washing with water (40 mL, twice) and acetone (40 mL) to remove surfactant, byproducts, and excess reagents, the product NP-SWNTs were dispersed in 20 mL dimethylformamide by gentle sonication for 10 min. The filtration and washing process was repeated on the dispersed product to ensure purity, and then the NP-SWNTs were dried at ambient conditions.

Raman spectroscopy verified covalent attachment of nitrophenyl groups to SWNTs (Figure 2), and Fourier transform infrared (FTIR) spectroscopy confirmed the composition of the groups. A Horiba Jobin Yvon LabRAM HR800 with a microscope measured Raman spectra using 785-nm laser excitation. FTIR spectra were obtained using a Thermo Nicolet 4700 spectrometer with an ATR (attenuated total reflectance) accessory. The covalent bonding of nitrobenzenes to the SWNT sidewalls increased the amplitude of the D-peak at ~1320 cm^{-1} in the Raman spectra relative to the G-peak at ~1590 cm^{-1}, which correspond to disordered and graphitic carbon bonding, respectively (Figure 2a). The D/G ratio can be tuned by adjusting the initial concentration of diazonium salt. Asymmetric and symmetric NO_2 stretching modes are visible in the FTIR spectra of all three varieties of nitrophenyl-SWNT films (Figure 2b).

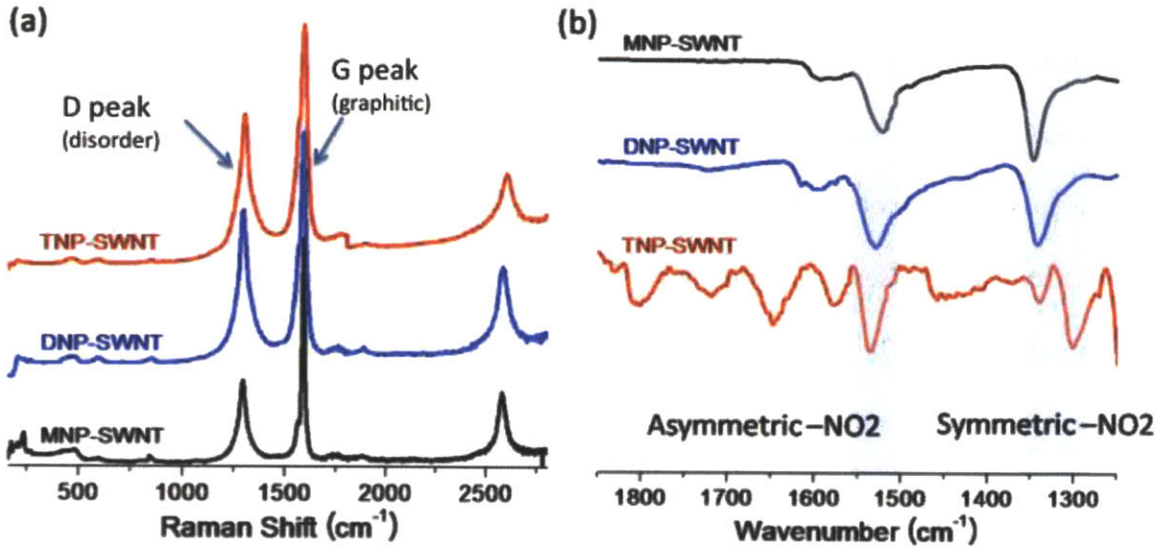

Figure 2. Raman and FTIR spectra of energetic nitrophenyl-SWNTs. (a) Disorder modes increased in the Raman spectra after covalent functionalization, showing introduction of defects from covalent bonds. (b) FTIR spectra show nitro groups are present. MNP-, DNP-, and TNP-SWNTs represent mono-, di-, and trinitrophenyl-functionalized SWNTs, respectively. Reprinted with permission from Reference [14] (courtesy of Changsik Song).

5.3 Differential Scanning Calorimetry

Differential scanning calorimetry (DSC) (Figure 3a) [21-23] demonstrated the exothermic properties of these nitrophenyl-functionalized SWNTs. 0.5 – 0.6-mg samples were loaded on an aluminum pan, and the temperature was scanned from 150 to 385 °C at 10 °C/min under nitrogen using a TA Instrument Q100. Negative peaks indicate exothermic heat flows.

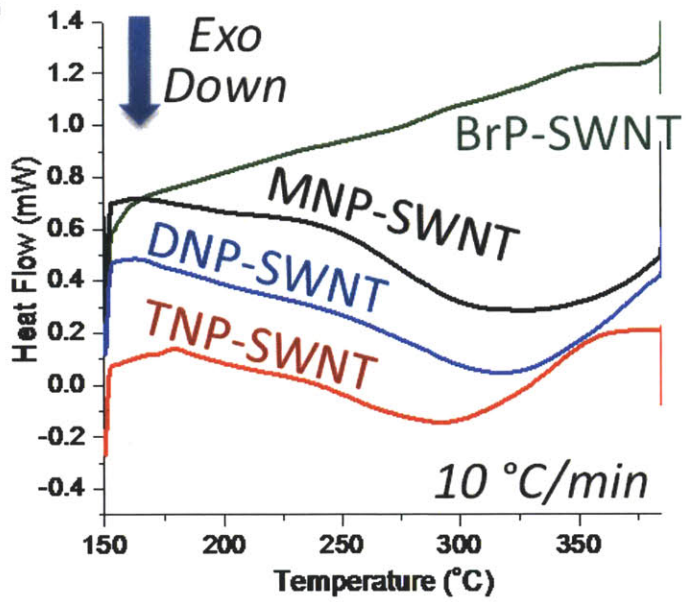

Figure 3. DSC heat flow (exo down) scanned at 10 °C/min under nitrogen for BrP-, MNP-, DNP-, and TNP-SWNTs. All the nitrophenyl-SWNTs react and release heat whereas the BrP-SWNTs do not. Reprinted with permission from Reference [14] (courtesy of Changsik Song).

For comparison, SWNTs functionalized with a non-energetic 4-bromophenyl group (BrP-SWNTs) were examined under the same conditions. When the non-energetic BrP-SWNTs were scanned, no appreciable variation from the baseline was observed. In contrast, energetically decorated SWNTs generate considerable heat when decomposing at high temperatures. As shown in Figure 3a, MNP-, DNP-, and TNP-SWNTs show exothermic peaks between 300 and 330 °C. Thus, energetically decorated SWNTs could serve as thermally induced heat-releasing elements.

The energy released by reaction depends on the total number of nitro groups, which in turn depends upon the type of moiety and the level of functionalization. Integrating the area between each DSC peak and its baseline (Figure 3a) gives energy densities of 780, 600, and 440 J/g for MNP-, DNP-, and TNP-SWNTs, respectively (including the SWNT mass). It should be noted that MNP-SWNTs can often achieve greater functionalization compared to either DNP-SWNTs or TNP-SWNTs. Thus heat release can

be controlled through the level of functionalization and types of energetic molecules on SWNTs, although the level of functionalization plays a bigger role here.

Another notable feature is the shift of the exothermic peak to lower temperatures as the number of nitro groups increases. This shift corresponds to the decreasing activation energy for thermal decomposition; more nitro groups progressively destabilize the molecule.[22] However, thermal decomposition begins around 170 °C regardless of the number of attached nitro groups per benzene ring. The onset temperatures for NP-SWNT thermal decomposition are somewhat lower than that of related small nitroaromatics; for example, 2,4,6-trinitroaniline (also known as picramide) begins to decompose at 258 °C and finishes by 278 °C.

NP-SWNTs could not support self-sustaining reaction waves without additional fuel coating, despite their energetic properties. After initiation of films of these molecules with a laser (785 nm, 40 mW) and with microwave irradiation, Raman spectroscopy observed de-functionalization of nitrophenyl groups from SWNTs in the vicinity of the irradiation spot. However, those reactions did not propagate farther, mainly due to the heat loss to the environment; suspending NP-SWNT films resulted in longer-traveling reactions (albeit still incomplete) than those on a substrate (which acts as a heat sink). In order to overcome the heat loss, either complete thermal isolation or much higher grafting density of energetic molecules is necessary.

5.4 Thermopower Wave Generator Preparation

However, DNP-SWNTs could support self-propagating reaction waves with additional solid fuel physically adsorbed to the SWNTs. The design of thermopower wave generators (TWGs) is described conceptually in the Introduction. Picramide (PA) (15 g/L in acetonitrile) and sodium azide (10 or 20 g/L in water) solutions were dropped on the fibers in turn, allowing several hours for solvent evaporation after addition of each solution. NaN_3 is an initiator to decrease activation energy of the reaction. Each

thermopower wave generator (TWG) was loaded with about three times as much PA as SWNTs by mass and one to two times as much NaN_3 as SWNTs. Applied at both ends of a SWNT fiber, silver paste flows around and among SWNTs before drying, forming strong, highly conductive electrical connections to copper tape electrodes. TWG resistances ranged from 1.5 to 162 Ω depending on length and width of the SWNT fibers.

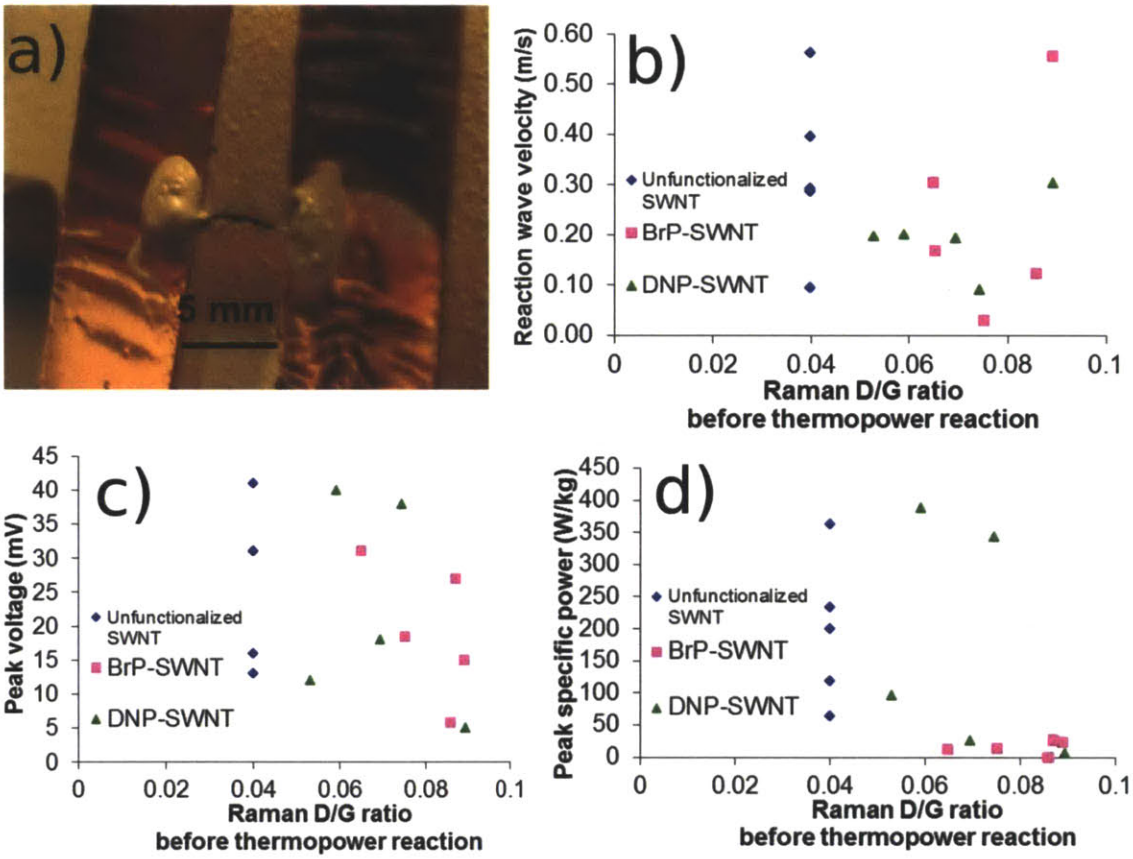

Figure 4: Thermopower waves on covalently functionalized SWNTs. a) A typical thermopower wave generator using bulk-scale SWNT fibers that have been functionalized. b) Average velocity of thermopower waves for three different SWNT types. All supported waves with velocities between 0.03 and 0.56 m/s, regardless of level of functionalization as measured by Raman spectroscopy. c) Peak voltage and d) specific power of thermopower waves. Again, functionalization did not significantly affect the generation of electricity. Reprinted with permission from Reference [14].

Dinitrophenyl-Functionalization of Single-Walled Carbon Nanotube Fibers (DNP-SWNTs)

Unfunctionalized and functionalized SWNT fibers were fueled with PA and incorporated in TWGs, as depicted in the image of Figure 4a. The fibers, obtained from KH Chemicals, contain individual SWNTs with diameters of 1.0 – 1.3 nm and lengths of 5 – 50 μm. Each fiber contains millions of SWNTs and thus is several millimeters long but does not have a well-aligned internal structure.

Similar to the previous procedure for dispersed SWNTs, SWNT fibers (~0.5 mg each) were placed in 1 % sodium dodecyl sulfate in water (~1 mL). Dinitrobenzenediazonium tetrafluoroborate (DNP-$N_2^+BF_4^-$, 1.35 mg, 5 mM) was added to the solution. The mixture was gently stirred at 45 °C for 6 h, at which time the functionalized SWNT fibers were washed three times each in acetone and water successively to remove any adsorbed reagents and SDS. The functionalized SWNT fibers were dried in air and characterized. BrP-SWNTs were produced in the same fashion using BrP-$N_2^+BF_4^-$. Because of heterogeneities in the SWNT fibers, the Raman spectrum of each thermopower wave generator was measured in three different locations and the resulting D/G ratios averaged.

Thermopower Wave Generator Testing: Effects of Functionalization

A digital oscilloscope (Yokogawa DL 1735E) measures voltage generated during the reaction. Current and power then can be calculated based on the known resistances of the TWGs and the oscilloscope circuit. The progress of the reaction wave is monitored visually at 4000 frames/second using a high-speed camera from Canadian Photonic Labs Inc. (Mega Speed, CPL-MS70KS2B90) with a Nikon, AF Micro-NIKKOR 60 mm f/2.8D macro lens. For these experiments, thermopower waves were initiated with a fine-tip butane torch.

The presence of functional groups and the level of functionalization did not affect the average velocity of these reaction waves. Figure 4b compares average velocities of reaction waves in picramide guided by DNP-, BrP-, and unfunctionalized SWNTs. Average velocity during reaction ranged from 0.03 to 0.56 m/s for all three types of SWNTs. This is less than the velocities measured for cyclotrimethylene-

trinitramine (TNA) on multiwalled carbon nanotubes (MWNTs), which ranged from 0.15 to 2.0 m/s.[10] TNA has very similar energetic properties to picramide, [24-29] but the SWNTs are shorter and not as well aligned as the MWNTs. Hence, the difference can be attributed to decreased thermal diffusivity of the SWNT mass since it has orders of magnitude more junctions between nanotubes, which slow thermal transport. The properties and performance of MWNTs and SWNTs (functionalized and unfunctionalized) are compared in Table 1.

Likewise, functionalization did not significantly affect electrical generation from thermopower waves. Figures 4c and 4d show the peak voltage and peak specific power, respectively, from thermopower wave generators using the three different SWNT materials. In each series, peak voltage ranged from about 5 to 40 mV, and peak specific power ranged from 5 to 400 W/kg. The BrP-SWNTs all produced < 30 W/kg peak specific power but not because of the functional groups. Rather, the fabrication of those generators resulted in large contact and internal resistance. The fact that BrP-SWNTs generated peak voltages in the same range as the other SWNT materials supports tracing the problem to resistance.

Table 1: Energetic Properties of Thermopower Wave Materials

Fuel / Conduit	*Voltage, V (max)*	*Specific Power, W/kg (max)*	*Activation Energy, kJ/mol*	*Wave Velocity, m/s (max)*	*Energy Density, J/g (max)*
TNA/MWNT[10]	210	7000	127 [29]	2.0	3870 [27]
PA/SWNT	41	360	134 [26]	0.56	2380
PA/BrP-SWNT	31	30	134 [26]	0.56	2840
PA/DNP-SWNT	40	390	134 [26]	0.30	2650
DNP-SWNT	---	---	96±56	---	600

Energy density calculated based on reaction enthalpy of fuel, including mass of fuel, initiator (NaN_3), and conduit. The mass ratio of TNA to MWNT is 9:1. The calculations for DNP-SWNT are based on Figure 3.

Based on the ratio of the intensity of D and G peaks, Raman spectroscopy shows that the level of functionalization is lower for the DNP- or BrP-SWNT fibers (Figure 4) than for functionalized dispersed SWNTs (Figure 2a). Nevertheless, both DNP- and BrP-SWNT fibers have larger D/G ratios than unfunctionalized fibers, confirming that covalent functionalization occurs. The covalent bonds between DNP or BrP moieties and nanotube sidewalls create electronic defects in the nanotube lattice, which should scatter phonons and electrons, decreasing SWNT conductivity. But these defects do not significantly disrupt the thermal or electrical conduction of thermopower waves, since neither reaction velocity nor specific power decreases measurably with functionalization, at least within the range of this study. This may allow SWNTs to be assembled into more complex nanostructures using covalent linker molecules[30] without disrupting their ability to conduct thermopower waves. However, Raman spectroscopy showed that, after thermopower waves on the SWNTs, D/G ratios decreased to less than their level immediately after covalent functionalization (but before thermopower wave reaction) (Supporting Information). This analysis indicates that thermopower waves break the bonds attaching the functional groups to the SWNTs without significantly damaging the SWNTs.

The energy content of the functional groups also did not affect the propagation of thermopower waves. DNP has a higher enthalpy of decomposition than BrP (Figure 3), so it might be expected to lend extra energy to a thermopower wave, increasing its velocity and/or power. However, no such enhancement was measured for this loading of energetic functional groups.

5.5 Conclusions

Single-walled carbon nanotubes can be decorated with energetic molecules – a series of nitroaromatics – via diazonium chemistry, and investigated their energy-releasing properties by DSC. The covalent functionalization was confirmed by Raman spectroscopy and the presence of nitro groups

was observed in the FT-IR spectroscopy. Energetically decorated SWNTs release heat when thermally excited, whereas non-energetic BrP-SWNTs demonstrated no energy output. Mono-, di-, and trinitrobenzene-functionalized SWNTs had energy densities of 780, 600, and 440 J/g, respectively, indicating that the increase in energy density per moiety with increasing number of nitro groups is not as influential as the efficiency of the functionalization reaction to overall energy density. Thermopower waves propagated on decorated SWNTs with the same velocity and power as on unfunctionalized nanotubes, showing that electronic defects do not necessarily disrupt wave propagation. These highly promising nanoenergetic materials demonstrate 1-D reaction propagation and directional energy release, and they can serve as on-demand nanoscale energy sources that can be remotely activated.

References

1. Arico, A.S., et al., *Nanostructured materials for advanced energy conversion and storage devices.* Nat Mater, 2005. **4**(5): p. 366-377.
2. Liu, J., et al., *Oriented Nanostructures for Energy Conversion and Storage.* ChemSusChem, 2008. **1**(8-9): p. 676-697.
3. Baxter, J., et al., *Nanoscale design to enable the revolution in renewable energy.* Energy & Environmental Science, 2009. **2**(6): p. 559-588.
4. Rolison, D.R., et al., *Multifunctional 3D nanoarchitectures for energy storage and conversion.* Chemical Society Reviews, 2009. **38**(1): p. 226-252.
5. Kotov, N.A., ed. *Nanoparticle Assemblies and Superstructures*. 2006, CRC Press: Boca Raton.
6. Rao, C.N.R., A. Muller, and A.K. Cheetham, eds. *The Chemistry of Nanomaterials: Synthesis, Properties and Applications*. 2004, Wiley-VCH: Weinheim.
7. Dlott, D.D., *Thinking big (and small) about energetic materials.* Materials Science and Technology, 2006. **22**(4): p. 463-473.
8. Armstrong, R.W., et al., *Enhanced Propellant Combustion with Nanoparticles.* Nano Letters, 2003. **3**(2): p. 253-255.
9. Abrahamson, J.T., N. Nitish, and M.S. Strano, *Modelling the increase in anisotropic reaction rates in metal nanoparticle oxidation using carbon nanotubes as thermal conduits.* Nanotechnology, 2008. **19**(19): p. 195701.
10. Choi, W., et al., *Chemically driven carbon-nanotube-guided thermopower waves.* Nature Materials, 2010. **9**(5): p. 423-429.
11. Choi, W., et al., *Carbon nanotube-guided thermopower waves.* Materials Today, 2010. **13**(10): p. 22-33.
12. Abrahamson, J.T., et al., *Wavefront Velocity Oscillations of Carbon-Nanotube-Guided Thermopower Waves: Nanoscale Alternating Current Sources.* ACS Nano, 2010: p. ASAP.
13. Walia, S., et al., *Oscillatory Thermopower Waves Based on Bi2Te3 Films.* Advanced Functional Materials, 2011. **21**(11): p. 2072-2079.

14. Abrahamson, J.T., et al., *Synthesis and Energy Release of Nitrobenzene-Functionalized Single-Walled Carbon Nanotubes.* Chemistry of Materials, 2011. **23**(20): p. 4557-4562.
15. Rosevear, J. and J. Wilshire, *A comparison of the reactions of some ethyl N-Arylcarbamates with those of the corresponding acetanilides. I. Nitration.* Australian Journal of Chemistry, 1985. **38**(5): p. 723-733.
16. Graff, R.A., T.M. Swanson, and M.S. Strano, *Synthesis of nickel-nitrilotriacetic acid coupled single-walled carbon nanotubes for directed self-assembly with polyhistidine-tagged proteins.* Chemistry of Materials, 2008. **20**(5): p. 1824-1829.
17. Smith, L.I. and J.H. Paden, *Studies on the Polymethylbenzenes. X. Reaction with Aromatic Diazonium Compounds1.* Journal of the American Chemical Society, 1934. **56**(10): p. 2169-2171.
18. Takagishi, I., Y. Hashida, and K. Matsui, *DIAZOTIZATION OF AROMATIC PRIMARY AMINES OF WEAK BASICITY .2. REDUCTION OF ARENEDIAZONIUM SALTS WITH ALKYLBENZENE DERIVATIVES.* Bulletin of the Chemical Society of Japan, 1979. **52**(9): p. 2635-2639.
19. Usrey, M.L., E.S. Lippmann, and M.S. Strano, *Evidence for a Two-Step Mechanism in Electronically Selective Single-Walled Carbon Nanotube Reactions.* Journal of the American Chemical Society, 2005. **127**(46): p. 16129-16135.
20. Nair, N., et al., *A Structure-Reactivity Relationship for Single Walled Carbon Nanotubes Reacting with 4-Hydroxybenzene Diazonium Salt*
doi:10.1021/ja068018i. Journal of the American Chemical Society, 2007. **129**(13): p. 3946-3954.
21. Long, G.T., B.A. Brems, and C.A. Wight, *Autocatalytic thermal decomposition kinetics of TNT.* Thermochimica Acta, 2002. **388**(1-2): p. 175-181.
22. Brill, T.B. and K.J. James, *Kinetics and mechanisms of thermal decomposition of nitroaromatic explosives.* Chemical Reviews, 1993. **93**(8): p. 2667-2692.
23. Cohen, R., et al., *Mechanism of thermal unimolecular decomposition of TNT (2,4,6-trinitrotoluene): A DFT study.* Journal of Physical Chemistry A, 2007. **111**(43): p. 11074-11083.
24. Brill, T.B. and K.J. James, *Thermal decomposition of energetic materials. 61. Perfidy in the amino-2,4,6-trinitrobenzene series of explosives.* Journal of Physical Chemistry, 1993. **97**(34): p. 8752-8758.
25. Liau, Y.C., E.S. Kim, and V. Yang, *A comprehensive analysis of laser-induced ignition of RDX monopropellant.* Combust. Flame, 2001. **126**(3): p. 1680-1698.
26. Maksimov, Y.Y. and E.N. Kogut, Russian Journal of Physical Chemistry, 1978. **52**: p. 805.
27. Volkov, E.N., A.A. Paletsky, and O.P. Korobeinichev, *RDX flame structure at atmospheric pressure.* Combust. Explo. Shock., 2008. **44**(1): p. 43-54.
28. Parr, T. and D. Hanson-Parr, *RDX ignition flame structure.* Twenty-Seventh Symposium (International) on Combustion, Vols 1 and 2, 1998: p. 2301-2308.
29. Williams, M.R. and M.V. Matei, *The decomposition of some RDX and HMX based materials in the one-dimensional time to explosion apparatus. Part 1. Time to explosion and apparent activation energy.* Propellants Explosives Pyrotechnics, 2006. **31**(6): p. 435-441.
30. Song, C., et al., *Controllable Synthesis of Single-Walled Carbon Nanotube Framework Membranes and Capsules.* Nano Letters, 2009. **9**(12): p. 4279-4284.

Chapter 6

The Origin of Voltage Pulse Polarity during Thermopower Wave Propagation

6.1 Introduction

Thermopower waves are a promising new electricity generation technology, allowing high-density power generation from chemical fuels.[1, 2] Their power density approaches the level of supercapacitors,[3-5] and their ultimate energy densities could be higher than either supercapacitors or batteries because the energy is stored in chemical bonds, rather than electrochemically. Moreover, this mechanism allows energy to be stored stably for long periods (months to years) with nearly zero losses.

Thermopower waves generate voltage from a rapidly moving thermal gradient created by an exothermic chemical reaction along a thermally and electrically conductive conduit. Figure 1 depicts a thermopower wave on single-walled carbon nanotubes (SWNTs) as example one-dimensional conduits. The conduits have a higher thermal diffusivity than the fuel coating them, so they conduct heat from the reaction forward, ahead of the reaction front, heating more fuel and initiating new reactions. Thus the thermal reaction wave is accelerated, and it drives a current in its propagation direction. However, the extent to which the electrical properties of these waves can be explained conventionally by the thermoelectric Seebeck coefficient, Γ, measured as the ratio of voltage generated per (steady-state) temperature difference, has been unclear to date.

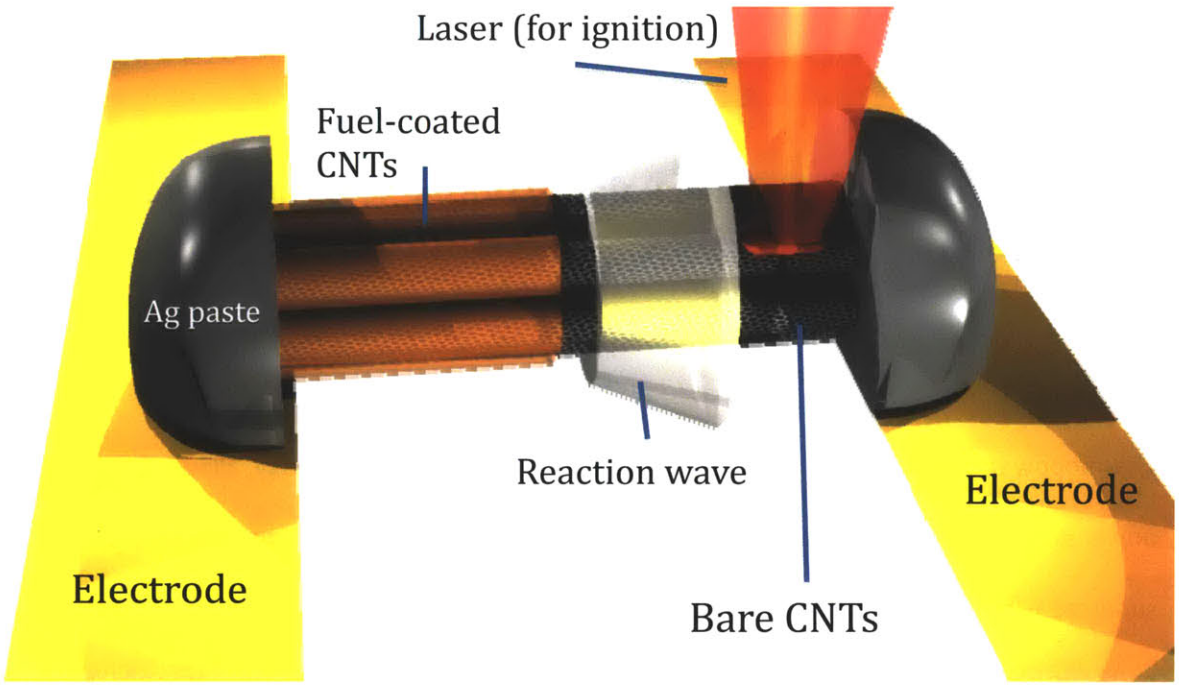

Figure 1: Schematic of thermopower wave generator. A solid fuel coats the thermal and electrical conduits (prototypically carbon nanotubes [CNTs]), which are connected to electrodes with silver paste. The fuel reacts in a self-propagating thermopower wave when ignited (*via* laser here), which produces an electrical pulse.

For rapid waves initiated at one end of a macrostructure (*i.e.* an array, fiber, or yarn) of carbon nanotubes, the voltage profile is, unusally, almost always of the form of a single-polarity pulse. With cooling behind the wave front, thermoelectric theory predicts that a second pulse of opposite sign should begin when the wave reaches the other end of the system and the gradient reverses; the front is the region of highest temperature. Another indication that thermopower wave voltage is generated by more than the temperature difference between the two contacts is the large magnitude of the voltage peak: up to 220 mV for cyclotrimethylene-trinitramine on multiwalled carbon nanotubes (MWNTs).[1] By contrast, the average Seebeck coefficient between 300 and 1400 K is -10 μV/K for aligned MWNTs,[6] which would only predict a peak voltage of 11 mV. Even a more conventional thermoelectric material, thin-film Bi_2Te_3 ($\Gamma \sim 300$ μV/K) , generates up to 150 mV when nitrocellulose reacts at ~600 K in thermopower waves, compared to the Seebeck prediction of 90 mV.[7] Finally, thermopower waves

exhibit voltage oscillations with frequency spectra closely matching those of wave velocity oscillations modeled by thermal transport equations.[8]

Despite their large electrical conductivities, individual SWNTs have a useful Seebeck coefficient at room temperature – about 40 μV/K.[6, 9] In SWNT macrostructures the larger Seebeck coefficients have been attributed to loose contacts between individual nanotubes and bundles; [6] that is, junction resistance plays a significant role. However, in individual SWNTs phonon drag effects are important to thermoelectricity, [10, 11] beyond carrier diffusion processes alone. Quantum-confined materials such as nanotubes enhance phonon drag because the motion of phonons and charge carriers is more aligned, so phonon momentum can be efficiently transferred to charge carriers.[12, 13] For more information about the basic thermoelectric properties of carbon nanotubes, readers may consult the review from Rao *et al.* [14]

Other measurements have revealed unusual thermoelectric properties in carbon nanotubes. For example, interactions with metal catalyst nanoparticles left over from the growth process can contribute to a large peak in the Seebeck coefficient from the Kondo effect. [15] However, the temperature range of this peak, 70 to 100 K, is far below the reaction temperatures of thermopower waves (> 1000 K).

Still, thermopower in carbon nanotubes is very environmentally sensitive; the sign of the Seebeck coefficient can reverse when nanotubes are depressurized or thermally annealed. This effect is attributed to the removal of ambient oxygen, which *p*-dopes SWNTs. [16, 17] Other adsorbed molecules, particularly aromatic hydrocarbons, can shift the Seebeck coefficient of SWNTs by as much as 8 μV/K with only monolayer coverage.[18] Sumanasekera *et al.* say the adsorbates create a new scattering channel for carriers. It is well known that carriers in SWNTs can couple strongly to π states in adsorbed molecules, enhancing their effects. This system had lower overall $|\Gamma|$ (< 10 μV/K) compared to later measurements of SWNTs, [9, 19] probably because of the initial vacuum conditions.

Beginning with the energy balance for thermopower waves, this work models adiabatic and large thermal loss scenarios and predicts characteristic bipolar voltage pulses for non-adiabatic waves. Using end-point temperature measurements of thermopower waves, we compare the expected voltage from literature models of the Seebeck coefficient of SWNTs and find that these models tend to overestimate the magnitude of secondary voltage peaks of opposite sign and often underestimate the first voltage peak. Adding a potential term from doping differences between fuel-coated and bare regions of the SWNTs can better describe experimental voltages and indicates a new approach to enhancing the unique properties of thermopower waves.

6.2 Theoretical Predictions of Voltage Profiles from Self-Propagating Reaction Waves

Previously we developed models for the temperature and chemical profiles of thermopower waves [8, 20] and demonstrated their accuracy. However, these models did not address the resulting electrical transport. To predict voltage from temperature data, we may start with the charge transport (sometimes called drift-diffusion) equation.[21]

$$J = -\sigma_h (E + \frac{\nabla \mu}{e}) - L_{12} \nabla T \quad (1)$$

J is current density, σ is electrical conductivity, E is electric field, μ is chemical potential, e is the elementary charge, L_{12} is an Onsager coupling coefficient, and T is temperature. Here properties are written in terms of holes as the majority carrier, as is the case for SWNTs in ambient conditions,[9, 19, 22] although it is simple to write an additional equation for electrons by changing the sign before σ. These quantities can be expressed as multi-dimensional vectors and tensors, but in a large-aspect-ratio (>10) system of carbon nanotubes, a one-dimensional representation is reasonable. When current is small enough to neglect (often the case for oscilloscope measurements), one can solve for E and integrate between two contacts (at positions x_L and x_R) to obtain an equation for voltage.

$$V = -\int_{x_L}^{x_R} \frac{\nabla \mu}{e} - \frac{L_{12}}{\sigma_h} \nabla T \mathrm{d}x \tag{2}$$

Since chemical potential can not be measured separately from electrochemical potential (E + μ/e), the Seebeck coefficient is defined as $\Gamma = \frac{E + \nabla \mu / e}{\nabla T} = \frac{L_{12}}{\sigma}$. Introducing a chemical potential gradient, *e.g.* through doping, can affect charge transport in addition to the effects of a temperature gradient. Most measurements of thermoelectricity in carbon nanotubes do not include a deliberate chemical or doping gradient, so we can define a reference coefficient Γ_{ref} for $\nabla \mu = 0$ to mathematically consider doping effects separately. By applying a change of variables, one can simplify the previous integral.

$$V = -\int_{\mu_L}^{\mu_R} \frac{1}{e} \mathrm{d}\mu + \int_{T_L}^{T_R} \Gamma_{ref} \mathrm{d}T = \frac{1}{e}(\mu_L - \mu_R) + \int_{T_L}^{T_R} \Gamma_{ref} \mathrm{d}T \tag{3}$$

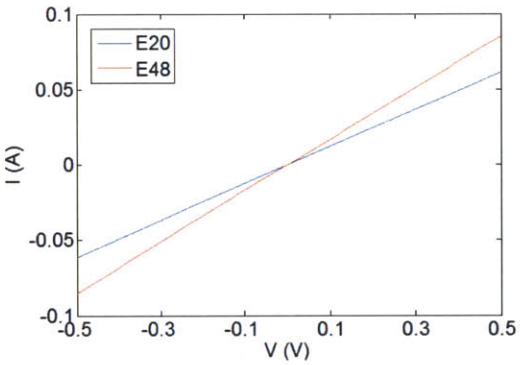

Figure 2: Current-voltage traces for two SWNT thermopower wave generators (after fueling). The constant resistance across the measurement indicates the contacts to silver are Ohmic.

In a real circuit, a counter-voltage develops through the electrodes and wires in response to the opposite ΔT in that direction. However, for our contact materials at room temperature (Fig. 1), the Seebeck coefficient of the electrodes is negligible, so this counter-voltage can be neglected. Silver has Γ = 1.51 μV/K, and copper has Γ = 1.83 μV/K.[23] With the same materials on both sides, $\Delta\mu$ = 0 in this way as well. Furthermore, SWNT-silver contacts do not exhibit rectification (*i.e.* they are Ohmic contacts)

because the work function of randomly oriented silver particles (4.26 eV) [23] is less than that of SWNTs (4.5 eV). I-V measurements of thermopower wave generators, shown in Figure 2, confirm this fact.

For a fiber of mixed semiconducting and metal SWNTs, the Seebeck coefficient has a form as measured recently by Hewitt *et al.*[19]

$$\Gamma_{ref} = aT + bT^{1/2} \exp[-(T_1 / T)^{1/(1+d)}] \quad (4)$$

Here, *a* and *b* are coefficients defining the weight of metallic and semiconducting contributions, respectively, T_1 is a constant related to the energy barrier for carrier hopping between SWNTs, and *d* is the dimensionality factor describing the density of junctions (= 2 for loosely connected SWNT macrostructures forming a percolation network, as typical of the fibers used in thermopower wave generators).[24, 25] Here *T* is in K, and Γ_{ref} has units of μV/K. From the measurements of Hewitt *et al.* for a static thermal gradient across mixed SWNTs, we obtain a = -0.022 μV/K^2, b = 2.0, T_1 = 20 K. The opposite signs of the metallic and semiconducting contributions indicate that fibers made from only semiconducting SWNTs, enabled by recent high-volume separation and sorting advances,[26] should be the best conduits for thermopower waves, as with conventional thermoelectric materials.

Describing the evolution of the temperature profile over time is crucial for thermopower waves, as it allows one to predict, through the Seebeck effect, the general shape of the voltage profile in time. In the simplest case, that of the adiabatic, steadily propagating reaction wave, during the time of reaction T_R and T_L are constant, as shown by example in Figure 3a. Thus, a square, unipolar voltage pulse (Figure 3b) results from an adiabatic reaction wave according to equation (3) (assuming $\Delta\mu = 0$ between the two ends).

However, real reaction waves have thermal losses from radiation, convection, and conduction and therefore will diverge from the logistic adiabatic wave temperature and voltage profiles. In particular, radiation should be the most significant factor because of its fourth-order temperature

dependence and the reaction temperatures exceeding 1000 K. The energy balance for the reacting fuel, including radiation, is

$$\rho C_p \frac{\partial T}{\partial t} = \chi \frac{\partial^2 T}{\partial x^2} - (\Delta H k_0 Y) \mathrm{e}^{-\frac{E_a}{RT}} - \frac{\varepsilon \sigma_B S}{V}(T^4 - T_{amb}{}^4) \tag{5}$$

where t is time, x is distance, χ is thermal conductivity, ρ is density, ΔH is the enthalpy of reaction, C_p is the specific heat (mass basis), Y is the concentration of fuel (mass basis), k_0 is the Arrhenius prefactor, R is the universal gas constant, E_a is the activation energy, S/V is the exterior surface-area-to-volume ratio, ε is the emissivity, σ_B is the Stefan-Boltzmann constant, and T_{amb} is the temperature of the surroundings.

The corresponding first-order reaction kinetics equation for solid fuel (no mass diffusion) is

$$\frac{\partial Y}{\partial t} = -(k_0 Y) e^{(-E_a/RT)} \tag{6}$$

Readers interested in further details of the development of the adiabatic equations may consult Reference [8]. These equations can then be non-dimensionalized as demonstrated in previous modeling work [8, 20]: temperature $u = \left(\frac{R}{E_a}\right) T$, time $\tau = \left(\frac{-\Delta H k_0 R}{C_p E_a}\right) t$, space $\xi = x\sqrt{\left(\frac{\rho C_p}{\chi}\right)\left(\frac{-\Delta H k_0 R}{C_p E_a}\right)}$, and concentration $y = \frac{Y}{\rho}$. The resulting equations are

$$\frac{\partial u}{\partial \tau} = \frac{\partial^2 u}{\partial \xi^2} + y e^{-1/u} - w\left(u^4 - u_{amb}{}^4\right) \tag{7}$$

$$\frac{\partial y}{\partial \tau} = -\beta y e^{-1/u} \tag{8}$$

with $w = \left(\frac{S}{V}\right)\left(\frac{\epsilon \sigma \beta}{\rho k_0 C_p}\right)$ and $\beta = \frac{C_p E_a}{-\Delta H R}$.

For thermopower waves, the inclusion of highly thermally conductive nano-conduits with large aspect ratios (such as carbon nanotubes) accelerates the reaction wave along their lengths. As

shown previously, [1, 27] heat transfer between fuel annuli and the conduits around which they are wrapped is not limiting, so both attain the same temperature profile moving with a velocity determined by the thermal diffusivity of the conduit. This effect can be incorporated in Equation (3) by multiplying the thermal diffusion term by the ratio of conduit to fuel thermal diffusivities, α_2/α. For this case, w uses the exterior S/V for the whole composite to avoid the complications of representing radiation within the structure.

Equations (7) and (8) were solved numerically with the commercial COMSOL 4.1 package. Using adiabatic boundary conditions and a sufficiently large initial Gaussian temperature pulse $(u = ge^{-\xi^2/w_i} + u_{amb})$ as described previously [8] ensures self-sustaining wave propagation. To match recent experiments, the system was initialized at 350 K with un-reacted fuel (y = 1) everywhere. Reaction and thermal parameter values were taken from picramide, the fuel used in experiments, except for thermal diffusivity (α_2/α), which was set by the SWNT thermal conduits as described above: C_p = 2424 J/kg/K, ρ = 1762 kg/m^3, E_a = 121 kJ/mol, k_0 (Arrhenius prefactor) = 1.6x10^7 s^{-1}, α_2/α = 25,000. Other parameters, related to radiation, are defined based on values typical to SWNT fibers used in experiments: ε = 0.9, S/V = 2900 m^{-1}.

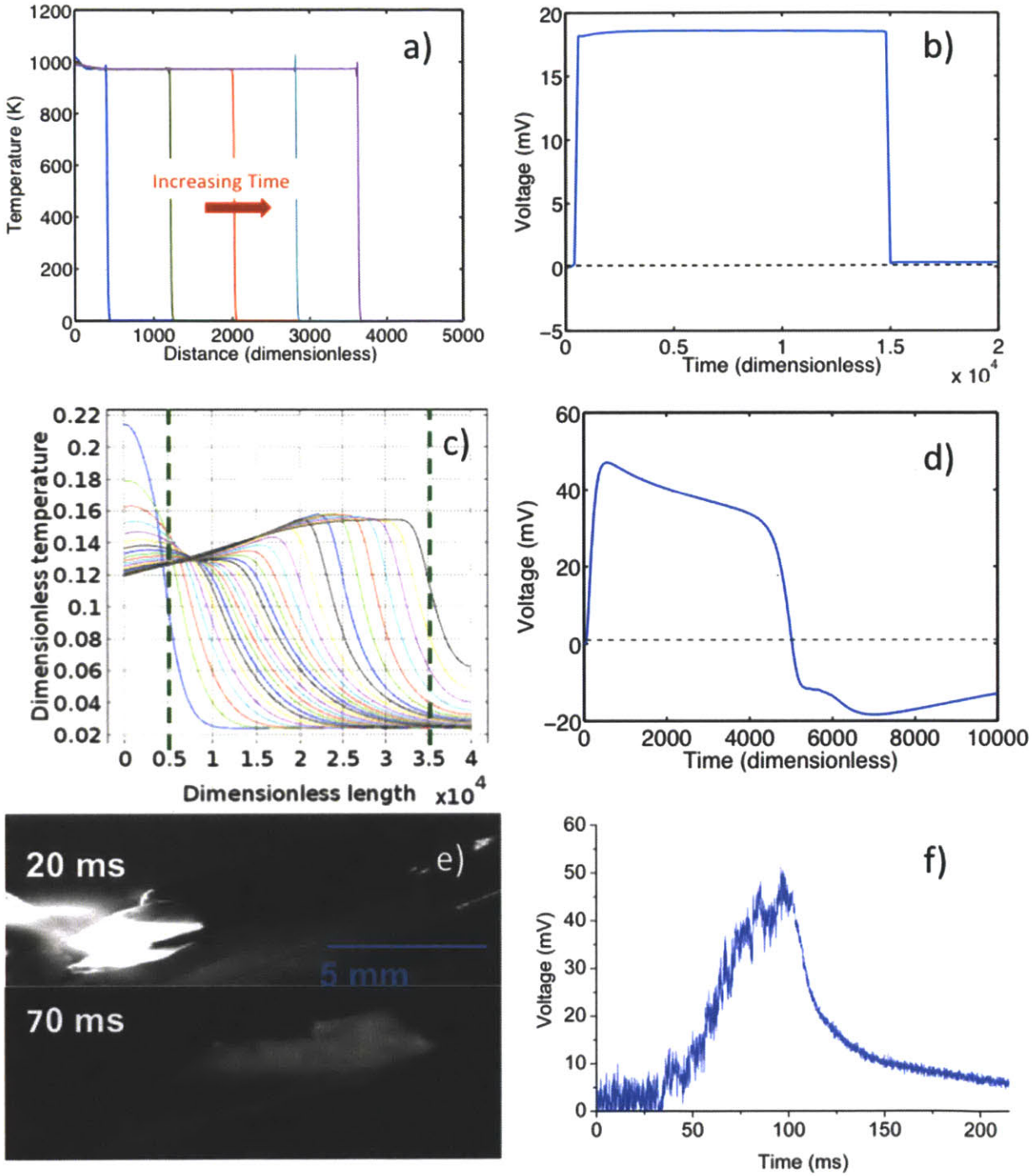

Figure 3: Theoretical predictions and experimental data for voltage polarity. a) Simulated temperature profiles of an adiabatic reaction wave. t = 2,000:4,000:18,000. β = 3, E_a = 24 kJ/mol. b) Voltage profile for the wave in a), based on contacts at 100 and 3,000. c) Simulated temperature profiles for a wave with losses from radiation and conduction losses to the contacts. β = 8, radiation coefficient $w = 5.3 \times 10^{-5}$, and boundary conduction coefficient q = 0.34. d) Voltage profile for wave in c), based on contacts at 5,000 and 35,000 (dashed lines). e) Example thermopower wave images, showing cooling behind the wave front. f) Voltage measurement from wave in e), which is unipolar despite the non-adiabatic nature of the wave.

Thermal conduction to the electrodes is another likely major thermal loss mode. In thermopower wave experiments, silver paste forms contacts between the SWNTs and copper tape electrodes. These contacts have high interfacial surface area and are generally quite massive compared to the fuel-coated nanotubes (at least fifty times larger), so they can act as large thermal reservoirs. Mathematically, such reservoirs can be represented as a Neumann boundary condition.

$$\frac{\alpha_2}{\alpha}\left(\frac{\partial u}{\partial \xi}\right) = q(u_{amb} - u) \tag{9}$$

Here q is termed the thermal flux coefficient, scaling the rate of heat loss through the boundary, which is proportional to the temperature difference between the SWNTs and the reservoir.

Thermal losses significantly affect the wave temperature profile shapes. Figure 3c shows temperature profiles for a wave with $\beta = 8$, radiation losses ($w = 5.3 \times 10^{-5}$, derived from experimental values described above), and conduction to the contacts ($q = 0.34$), which requires $g = 7$ to initiate propagation. The velocity is about 8% of the adiabatic wave in Figure 3a, for which $\beta = 3$, $w = 0$, $q = 0$, and $E_a = 24$ kJ/mol to attain temperatures in the range of those measured. The wave initiation period is visible as the ignition pulse dies down and the front spreads forward. The wave then accelerates and attains the adiabatic reaction temperature ($1/\beta + u_{amb}$) at the front, while cooling about 25% behind it. This temperature decrease leads to a proportional decrease in voltage after the peak (Figure 3d). When the right contact ($\xi = 35{,}000$) reaches reaction temperature, the thermal gradient reverses, creating the second V peak of opposite polarity – a bipolar voltage pulse. Thus, non-adiabatic thermopower waves should exhibit bipolar voltage pulses according to Seebeck coefficient models of the literature.

Thermopower waves are clearly non-adiabatic, with cooling behind the front made visible as decreased thermionic emission, as shown in the example of Figure 3e. These images show a thermopower wave from picramide and NaN_3 reacting on SWNTs. However, the accompanying voltage pulse is unipolar (Figure 3f). Another important difference between these measurements and the

theoretical predictions is that the maximum voltage occurs when the wave reaches the opposite contact, rather than the time of maximum ΔT. For the simulations, the peak voltage occurs when the wave begins propagation at the left end of the domain.

COMSOL employs adaptive time-stepping to improve the stability of its calculations, and we confirmed convergence of the simulations by comparing results at several spatial mesh sizes. Figure 3a-d was created with mesh size $\Delta\xi = 1$, and Figure 4 shows temperature profiles for three other mesh sizes with $\beta = 4$ and $w = 2.7 \times 10^{-5}$. Wave shape and speed do not change over $0.5 < \Delta\xi < 4$. The simulation initiation parameters were g (initial Gaussian amplitude) = 2.1 and w_i (Gaussian peak width parameter) = 5000.

6.3 Experimental Methods

As demonstrated in previous experiments,[28] picramide (PA) and sodium azide together form a good fuel mixture for thermopower waves, providing high-temperature reaction and reliable ignition. SWNT fibers from KH Chemicals (South Korea) are easy-to-use macrostructures with lengths 5 – 20 mm and widths 0.5 – 2 mm. Each fiber thus contains millions of SWNTs (individuals or small bundles) with diameters of 1.0 – 1.3 nm and lengths of 5 – 50 μm. The fuel compounds physically adsorb to the SWNTs after deposition from their respective solutions (PA: 20 g/L in acetonitrile; NaN_3: 20 or 50 g/L in water). The solvents evaporate for 1 and 4 h, respectively, after addition of each solution. The masses of PA and of NaN_3 should be at least as much as the mass of SWNTs for successful reaction.

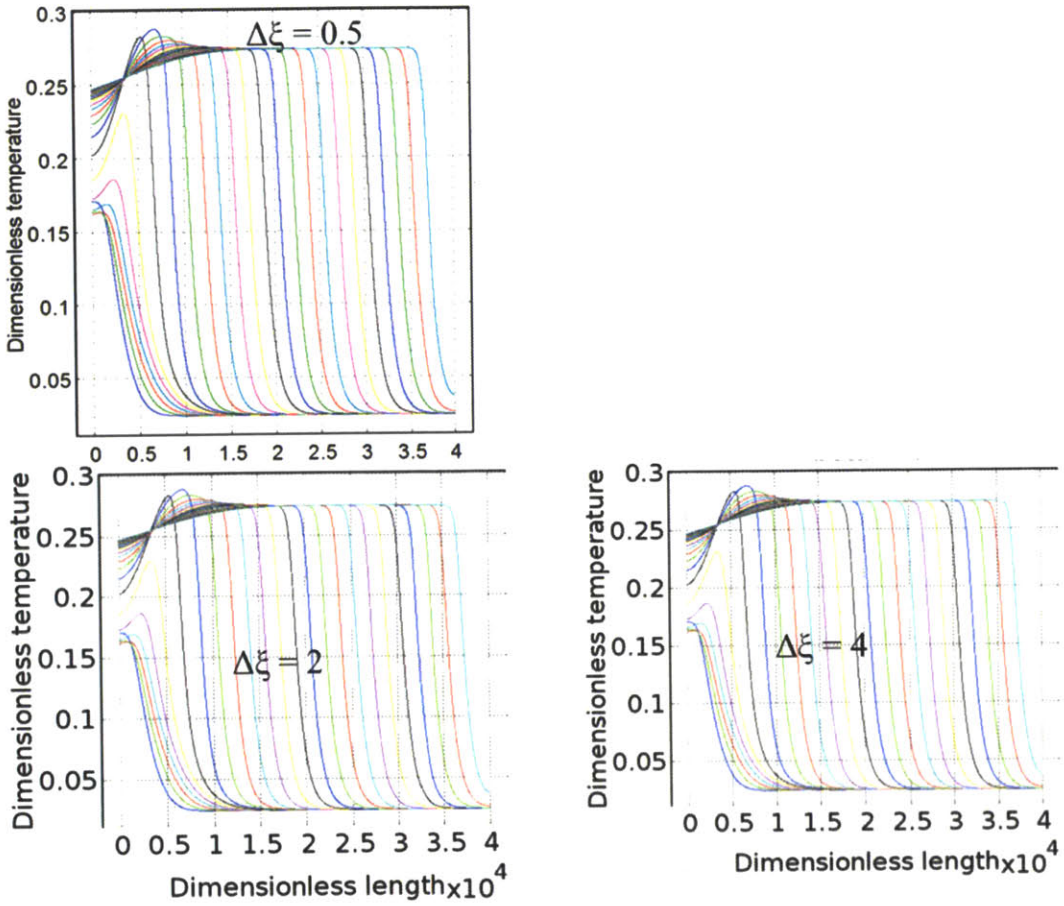

Figure 4: Verifying convergence for numerical simulations. Example temperature profiles for a propagating reaction wave with radiative cooling and adiabatic boundaries, $\beta = 4$, $w = 2.7 \times 10^{-5}$.

A digital oscilloscope (Yokogawa DL 1735E or 2000) measured voltage from thermopower waves. A high-speed camera recorded the wave propagation at 1000 – 4000 frames/second (Canadian Photonic Labs, CPL-MS70KS2B90) with a Nikon, AF Micro-NIKKOR 60 mm f/2.8D macro lens. Two pyrometers (Raytek MM1MH and Omega OS4000) measured temperature at the left and right ends, respectively, of each SWNT fiber. The Raytek measures spectral response at 1 μm with a semiconductor photodetector and calculates temperature assuming (emissivity-adjusted) blackbody emission (accuracy: ± 0.3% + 1 K, range: 540 ˚C < T < 3000 ˚C). The Omega uses an InGaAs photo detector (spectral response: 1.2 to 2.6 μm, accuracy: ±1%, 350 ˚C < T < 1500 ˚C). Since carbon nanotubes are nearly blackbody emitters with little wavelength dependence in their emission, this approach is valid.

Moreover, we measured the temperature-dependent emissivity of these SWNT fibers by comparing temperatures recorded by a type K thermocouple and a thermal camera (FLIR 7650). ε ranges from 0.82 to ~1 from ambient to reaction temperatures, and is ≥ 0.98 above 800 K, so it is nearly constant for the pyrometers.

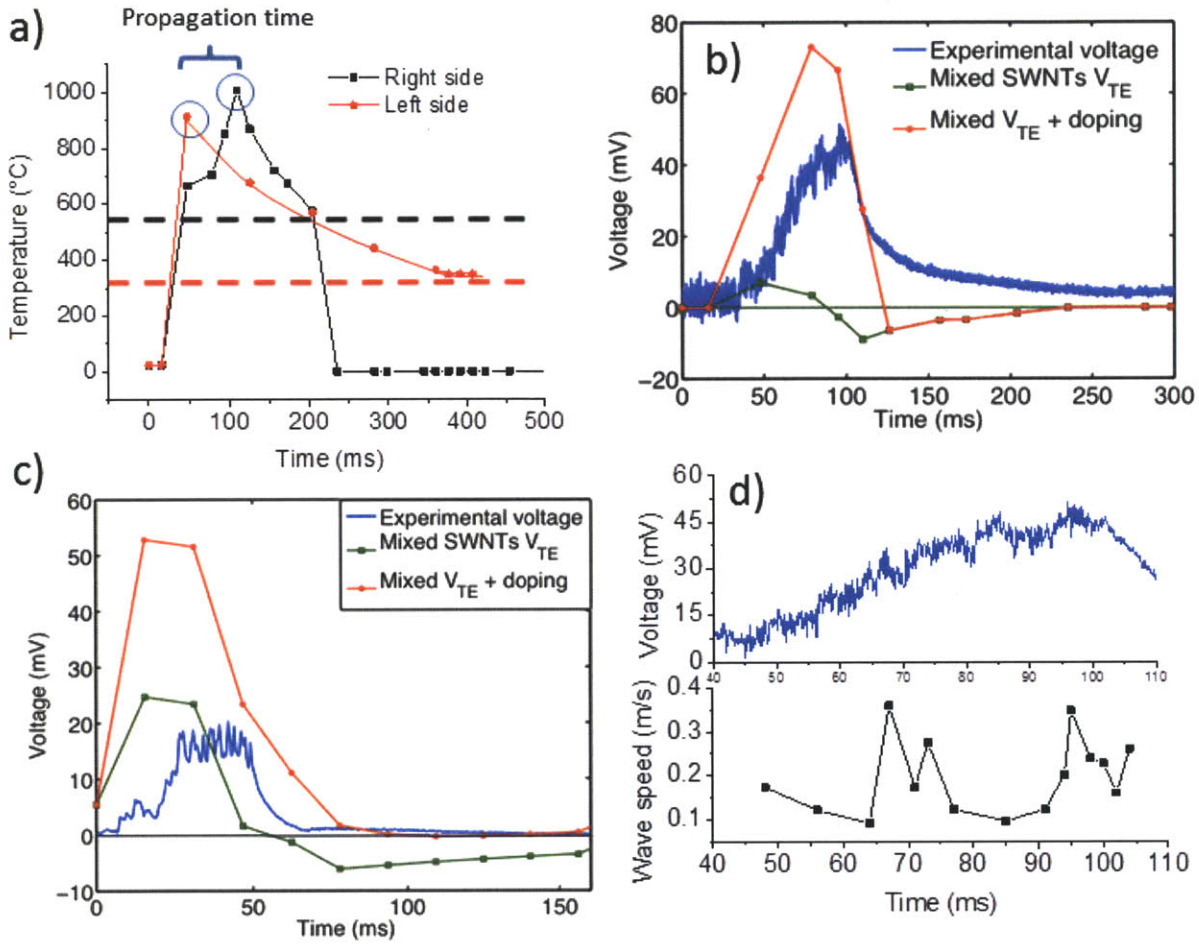

Figure 5: Synchronized voltage, temperature, and velocity measurements of thermopower waves. a) Temperature measurements. The two pyrometers have different spectral ranges, so their lower measurement bounds (indicated by the dashed lines) differ. b) Voltage for wave in a), with predictions based on measured temperatures using models of thermoelectricity in SWNTs, with and without additional doping contributions. c) Voltage profile for a different wave with smaller magnitude peak, compared to models from temperature measurements. d) Speed of wave in a) compared to voltage during propagation time.

A 785-nm, 100-ms laser pulse (300 mW, spot size <1 mm^2) initiated thermopower waves after preheating to 50 – 80 ˚C with a small 10-W resistance heater (silicone-covered to avoid current leakage into thermopower measurement circuit). Control samples with no reaction (only laser and preheating)

showed voltage changes < 3 mV. A 5 V TTL pulse from a custom control circuit board triggered the instruments to start with the laser pulse and stop synchronously. Synchronization can be checked by comparing the timing of temperature peaks at the left and right sides to the timing of brightest reaction at each side observed with the camera.

6.4 Measurements of Thermopower Wave Voltage and Temperature

As is often the case for thermopower waves, even with significant cooling the voltage pulse is unipolar. Figure 5a shows the temperature measurements for the wave of Fig. 3f, confirming monotonic cooling after the wave passes. The maximum temperature during the reaction is very high – about 1000 °C. However, the voltage peak is greater than 50 mV and unipolar (Figure 5b). This experiment used 0.53 mg each of picramide and NaN_3 deposited on a SWNT fiber (0.118 mg, 12 mm long), and the internal resistance of the generator was 8 Ω after attachment to contacts.

Figure 5b compares the measured voltage to two different voltage models based on the temperatures in Fig. 5a. (The pyrometers record more slowly than the oscilloscope, yielding the discrete points of the predicted voltage curves.) The Seebeck coefficient for mixed SWNTs from Hewitt *et al.*, Γ_{ref}, predicts the curve denoted V_{TE}, but it under-predicts the peak voltage by about 30 mV. Moreover, it predicts a bipolar pulse with a negative peak of almost -10 mV.

Since Γ_{ref} was measured under static thermal gradients and uniform doping, the contributions of $\Delta\mu$ would have been negligible in equations (2) and (3). However, dynamic chemical potential differences from doping could play a role for thermopower waves. Ahead of the front, the SWNTs are coated with fuel, which could dope that region of the SWNTs, as observed in steady-state adsorption experiments from the literature,[16-18] relative to the region behind the front, where the fuel has desorbed and/or reacted. Since the chemical potential is equivalent to the Fermi energy, E_F, changes in μ can be described in terms of changes in carrier density, n_l, according to the density of states for metals

(subscript '*m*') and semiconductors (subscript '*s*') near the Fermi level, which are determined by their respective Fermi velocities, v_F.[29] The carrier density is in linear terms (#/length) due to the 1D nature of the SWNTs.

$$\frac{\partial \mu}{\partial t} = \frac{\partial E_F}{\partial t} = p_m \left(\frac{\partial n_{l,m}}{\partial t} h v_{F,m} \right) + p_s \left(\frac{\partial n_{l,s}}{\partial t} h v_{F,s} \right) \tag{10}$$

Here h is the Planck constant, and p_m and p_s are coefficients representing the fractions of metallic and semiconducting SWNTs, respectively, in the fiber, about 1/3 and 2/3 for the unsorted SWNTs of these experiments. Equation (10) is written for electrons as the majority carrier; increases in carrier concentration raise the Fermi level.

From this hypothesis, the carrier concentration will change with the desorption/reaction rate of the fuel, which should be a zero-order, temperature-activated process. [30] In this case the rate will be equal for m- and s-SWNTs, assuming the fuel binds equally to them.

$$\frac{\partial n_l}{\partial t} = \pm m k_d e^{-\Delta H_d/(RT)} \tag{11}$$

Here m is the number of electrons donated per molecule desorbed (on the order of 1), k_d is the desorption rate constant, and ΔH_d is the enthalpy of desorption binding the fuel to the SWNTs. The sign of the rate is positive for p-doping fuels (such as picramide, with strongly electronegative NO_2 groups) and negative for n-doping fuels.

Using equations (10) and (11) to calculate μ_L and μ_R over time, we can use the full form of equation (3) to better describe thermopower wave voltage, as shown in the doping models of Figure 5b and 5c. Picramide and NaN_3 react most rapidly after desorption, so k_d is set as the geometric mean of the Arrhenius prefactors of the two compounds, 2.6 x 10^8 1/s. [31, 32] Shen *et al.* measured ΔH_d for several nitroaromatic molecules (1,3-dinitrobenzene, m-nitrotoluene, p-nitrophenol, and nitrobenzene) on CNTs to be on the order of 40 kJ/mol,[30] and Figure 5b and 5c use a value of 42±3 kJ/mol.

Adding the $\Delta\mu$ term to account for differential doping can thus largely or completely cancel the negative peak of the V_{TE} model. For waves with large peak voltage (> 40 mV) such as in Figure 5b, the model with doping contributions also better matches the main peak magnitude, even though Figure 5c used a smaller value of *m* (0.28) according to the relatively lower fuel loading on that sample. This generator used 0.046 mg picramide and 0.069 mg NaN_3 on a 0.046-mg SWNT fiber (9 mm long; internal resistance = 26 Ω). The variability in doping contributions may stem from differences in internal structure and density of junctions in the SWNT fibers, which have linear densities ranging from 3 to 35 mg/m. Accordingly, fuel coating of SWNTs may very, as well as the junction density parameter *d*. To the extent that the SWNTs are not individually dispersed within the fiber (*i.e.* some may be inside bundles), they will not all be accessible to fuel doping. Thus, the actual doping is likely to be less than the model prediction, which would bring the theoretical curves closer to the experimental voltage pulses.

Previous discussion of the large voltages of thermopower waves focused on the large wave velocities (up to 2 m/s) observed.[1] We posited these effects as"electron [or hole] entrainment" to phenomenologically describe charge carriers caught up in and accelerated by the rapidly moving reaction front. However, Figure 5d shows no strong correlation between |V| and instantaneous wave velocities measured synchronously. While the velocity fluctuates between 0.09 and 0.36 m/s, a factor four difference, the amplitude of V oscillations is at most 10 mV.

6.5 Conclusions

The first synchronous measurements of temperature, voltage, and velocity of thermopower waves have yielded new insights into the physics underlying their power generation. Simulation of thermopower waves with thermal losses from radiation and conduction to large contacts shows that non-adiabatic waves should produce bipolar voltage pulses, based on literature Seebeck coefficients for mixed SWNT macrostructures under static thermal gradients. However, measured voltage pulses are often unipolar,

despite significant thermal losses. Including an extra chemical potential difference, unipolar in time, between the bare SWNTs behind the wave front and the fuel-coated SWNTs can cancel the opposite potential of the secondary voltage peak, yielding a unipolar pulse. This chemical potential difference also explains the large magnitude of primary voltage peaks, in excess of theoretical predictions, by adding to the primary thermoelectric peak.

References

1. Choi, W., et al., *Chemically Driven Carbon Nanotube-Guided Thermopower Waves.* Nature Materials, 2010. **9**: p. 423-429.
2. Choi, W., et al., *Carbon Nanotube-Guided Thermopower Waves.* Materials Today, 2010. **13**: p. 22-33.
3. Pech, D., et al., *Ultrahigh-power micrometre-sized supercapacitors based on onion-like carbon.* Nat Nano, 2010. **5**(9): p. 651-654.
4. Kang, B. and G. Ceder, *Battery materials for ultrafast charging and discharging.* Nature, 2009. **458**(7235): p. 190-193.
5. El-Kady, M.F., et al., *Laser Scribing of High-Performance and Flexible Graphene-Based Electrochemical Capacitors.* Science, 2012. **335**(6074): p. 1326-1330.
6. Baxendale, M., K. Lim, and G. Amaratunga, *Thermoelectric power of aligned and randomly oriented carbon nanotubes.* Physical Review B, 2000. **61**: p. 12705-12708.
7. Walia, S., et al., *Oscillatory Thermopower Waves Based on Bi2Te3 Films.* Advanced Functional Materials, 2011. **21**(11): p. 2072-2079.
8. Abrahamson, J.T., et al., *Wave Front Velocity Oscillations of Carbon Nanotube-Guided Thermopower Waves: Nanoscale Alternating Current Sources.* ACS Nano, 2011. **5**(1): p. 367–375.
9. Yu, C.H., et al., *Thermal conductance and thermopower of an individual single-wall carbon nanotube.* Nano Lett., 2005. **5**(9): p. 1842-1846.
10. Scarola, V.W. and G.D. Mahan, Physical Review B, 2002. **66**: p. 205405.
11. Vavro, J., et al., Physical Review Letters, 2003. **90**: p. 065503.
12. Tsaousidou, M., *Theory of phonon-drag thermopower of extrinsic semiconducting single-wall carbon nanotubes and comparison with previous experimental data.* Phys. Rev. B, 2010. **81**(23).
13. Pop, E., et al., *Negative differential conductance and hot phonons in suspended nanotube molecular wires.* Physical Review Letters, 2005. **95**(15): p. 155505-155508.
14. Rao, A.M., X. Ji, and T.M. Tritt, *Properties of Nanostructured One-Dimensional and Composite Thermoelectric Materials.* MRS Bulletin, 2006. **31**: p. 218-223.
15. Grigorian, L., et al., *Giant thermopower in carbon nanotubes: A one-dimensional Kondo system.* Physical Review B, 1999. **60**: p. R11309-R11312.
16. Hone, J., et al., Physical Review Letters, 1998. **80**: p. 1042.
17. Sumanasekera, G.U., et al., *Effects of Gas Adsorption and Collisions on Electrical Transport in Single-Walled Carbon Nanotubes.* Physical Review Letters, 2000. **85**(1096-1099).
18. Sumanasekera, G.U., et al., *Giant thermopower effects from molecular physisorption on carbon nanotubes.* Physical Review Letters, 2002. **89**(16): p. 166801.

19. Hewitt, C.A., et al., *Varying the concentration of single walled carbon nanotubes in thin film polymer composites, and its effect on thermoelectric power.* Applied Physics Letters, 2011. **98**(18): p. 183110-3.
20. Abrahamson, J.T. and M.S. Strano, *An Analytical Solution to Coupled Chemical Reaction and Thermally Diffusing Systems: Applicability to Self-Propagating Thermopower Waves.* Journal of Physical Chemistry Letters, 2010. **1**(24): p. 3514–3519.
21. Zhang, Z.M., *Nano/microscale heat transfer.* Nanoscience and Technology Series2007, New York: McGraw-Hill. 479.
22. Bradley, K., et al., *Is the Intrinsic Thermoelectric Power of Carbon Nanotubes Positive?* Physical Review Letters, 2000. **85**: p. 4361-4364.
23. Lide, D.R., ed. *CRC Handbook of Chemistry and Physics*. 92 ed. 2012, CRC Press: Boca Raton.
24. Kaiser, A., G. Düsberg, and S. Roth, *Heterogeneous model for conduction in carbon nanotubes.* Physical Review B, 1998. **57**(3): p. 1418-1421.
25. Carroll, D.L., R. Czerw, and S. Webster, *Polymer–nanotube composites for transparent, conducting thin films.* Synthetic Metals, 2005. **155**(3): p. 694-697.
26. Liu, H., et al., *Large-scale single-chirality separation of single-wall carbon nanotubes by simple gel chromatography.* Nat Commun, 2011. **2**: p. 309.
27. Abrahamson, J.T., N. Nair, and M.S. Strano, *Modelling the increase in anisotropic reaction rates in metal nanoparticle oxidation using carbon nanotubes as thermal conduits.* Nanotechnology, 2008. **19**(19): p. 195701-195708.
28. Abrahamson, J.T., et al., *Synthesis and Energy Release of Nitrobenzene-Functionalized Single-Walled Carbon Nanotubes.* Chemistry of Materials, 2011. **23**(20): p. 4557-4562.
29. Paulus, G.L.C., et al., *Charge Transfer in Junctions of Single Layer Graphene and Metallic Single Walled Carbon Nanotubes.* submitted, 2012.
30. Shen, X.-E., et al., *Kinetics and thermodynamics of sorption of nitroaromatic compounds to as-grown and oxidized multiwalled carbon nanotubes.* Journal of Colloid and Interface Science, 2009. **330**(1): p. 1-8.
31. Mohan, V.K. and V.R.P. Verneker, *ROLE OF CRYSTAL IMPERFECTIONS IN THERMAL-DECOMPOSITION OF SODIUM AZIDE.* Journal of Physical Chemistry, 1976. **80**(2): p. 119-122.
32. Maksimov, Y.Y. and E.N. Kogut, Russian Journal of Physical Chemistry, 1978. **52**: p. 805.

Chapter 7

Excess Thermopower and Thermopower Waves

7.1 Introduction

Thermopower waves have already demonstrated their use as high-power electrical generators with stable energy storage in chemical bonds. These properties make them competitive with batteries[1-5], and chemical energy storage offers another possible advantage in terms of energy density. The maximum energy density available from chemical fuels is an order of magnitude larger than electrochemical storage in batteries. For example, ethanol has specific energy storage of 26.8 MJ/kg, whereas lithium-ion batteries can only store 0.720 MJ/kg, about 2.7% of ethanol. [5, 6] However, to make the most of the fuel's energy density, the generator must react it and extract electricity efficiently. In this sense, the comparison to batteries is problematic; although the Coulombic efficiency (the fraction of available energy delivered during discharge) can exceed 99%, this figure does not include the efficiency of the process that generated the electricity used to charge the battery originally. In this way, it is rather the charging of batteries that faces similar thermodynamic limitations to efficiency to a chemical-based system like a thermopower wave generator (TWG).

Some of the first TWGs produced surprisingly large voltage pulses (up to 220 mV) and peak power (up to 7 W/g).[7] However, without temperature measurements, it was unclear what portion of this voltage and power derived from the Seebeck effect and how much might be linked to the reaction wave (*i.e.* carrier entrainment) or to other processes. Even though power and wave speed are positively correlated, simply reacting the same energy equivalent of fuel in a shorter time (i.e. a faster wave) would create larger peak power to some degree.

With new temperature measurements, this work confirms that many thermopower waves generate voltage and power in excess of the Seebeck effect predicted for mixtures of semiconducting and metallic single-walled carbon nanotubes (SWNTs). The excess voltage and power increase with reaction temperature and wave speed. This excess is despite the non-adiabatic nature of TWGs. This work also quantifies experimental radiative losses and examines device designs that decrease thermal losses to boost reaction temperature, voltage, and electrical conversion efficiency.

7.2 Energy Balance for Thermopower Waves

We may begin by expanding the adiabatic energy balance for reaction waves developed in previous work.[8, 9]

$$\rho C_p \frac{\partial T}{\partial t} = \chi \frac{\partial^2 T}{\partial x^2} + \Delta H k_o Y \exp\left(-\frac{E_a}{RT}\right) \quad (1)$$

Here T is temperature, t is time, x is distance, χ is thermal conductivity, ρ is density, ΔH is the enthalpy of reaction, C_p is the specific heat (mass basis), Y is the concentration of fuel (mass basis), k_0 is the Arrhenius prefactor, R is the universal gas constant, and E_a is the activation energy. We now add terms for convection losses, conduction to the contacts, and the energy input required for ignition (E_{ignite}) and making explicit the energy output as electricity ($E_{electric}$). In this form the control volume for the balance encloses the conduits (prototypically SWNTs) and the fuel between the contacts.

$$\rho C_p \frac{\partial T}{\partial t} - \frac{E_{electric}}{V} = \Delta H k_o Y \exp\left(-\frac{E_a}{RT}\right) - \frac{\varepsilon \sigma_B S}{V}(T^4 - T_{amb}^{\ 4}) - \frac{h_c S}{V}(T - T_{amb}) - \frac{q_D A_{\text{int}}}{V}(T - T_{contact}) - \frac{E_{ignite}}{V} \quad (2)$$

The new variables used here are S/V, the exterior surface-area-to-volume ratio, ε, the emissivity, σ_B, the Stephan-Boltzmann constant, T_{amb}, the temperature of the surroundings, h_c, the convective heat transfer coefficient, q_D, the dimensional thermal boundary conduction coefficient (similar to dimensionless q), A_{int}, the interfacial area between the conduits and the contacts (typically silver), and $T_{contact}$, the temperature of the contacts, which may be assumed = T_{amb} if the contacts are very large

compared to the mass in the control volume (*i.e.* thermal reservoirs). Practically speaking, the conduits can be suspended between contacts to eliminate any other conduction pathways.

To prepare TWGs with SWNT thermal conduits, we used fibers from KH Chemicals (South Korea), easy-to-use macrostructures with lengths 5 – 20 mm and widths 0.5 – 2 mm. These commercially available fibers are longer than multiwalled carbon nanotube (MWNT) arrays (which must be custom grown) and have a smaller extent of variation in electrical and other properties with growth conditions. They are acid-treated to remove leftover metal catalyst from the CVD process, and each fiber contains millions of SWNTs (individuals or small bundles) with diameters of 1.0 – 1.3 nm and lengths of 5 – 50 μm.

Picramide (PA) and sodium azide together form a good fuel mixture for thermopower waves. PA provides large ΔH for high-temperature, whereas NaN_3 lowers overall E_a, increasing reliability of ignition. The fuel compounds physically adsorb to the SWNTs after deposition from their respective solutions (PA: 20 g/L in acetonitrile; NaN_3: 20 or 50 g/L in water). The solvents evaporate for 1 and 4 h, respectively, after addition of each solution. The masses of PA and of NaN_3 should be at least equal to the mass of SWNTs for successful reaction.

The production of TWGs introduces some subtleties to the energy balance; less than the entire ΔH is available for electricity generation. First, attaching fueled SWNTs to contacts requires some length of the SWNTs (~1 mm on either side with present manual fabrication) to be covered by silver paste in order to form a secure, low-resistance contact to copper tapes. The fuel on these SWNTs is then unavailable to the reaction wave due to the massive thermal sink surrounding it. Most current TWGs "lose" 20-30% of their energy this way, although improved contact fabrication and/or longer devices could decrease this fraction significantly. Additionally, due to sample imperfections, sometimes the reaction wave may not propagate the entire length of the sample, leaving some fuel un-reacted. The un-

reacted length may be 10 – 50% of the sample, making incomplete reaction another culprit in decreased efficiency.

7.3 Preheating and ignition energy

The first demonstrations of thermopower waves,[7] were ignited with a 300-mW fiber optic laser emitting at 785 nm. However, the laser was handheld and required variable lengths of time on the order of seconds to ignite reactions while it neared the samples. Moreover, this approach only succeeded for about two-thirds of samples and made it impossible to quantify the true ignition energy requirements for thermopower waves. When the laser system was automated to produce spatially controlled (spot size <1 mm^2) 100-ms pulses (to match the time scale of the waves), reaction waves did not ignite. Therefore, some element of preheating (supplied by the spatially diffuse heating during the approach period in the original laser experiments) is needed to controllably ignite thermopower waves.

To decouple preheating and laser ignition, a small 10-W electrical resistance heater suffices. Raising the initial temperature of the whole TWG to 50 – 80 °C (as measured by type K thermocouple) successfully ignites waves >90% of the time (provided the laser system lens is focused and clean). The preheater must contribute 70 J/g, or about 4% of the activation energy of NaN_3, the initiator compound. In practical terms, the preheat requirement could mean that TWGs are better suited for environments with higher ambient temperatures (e.g. near engines). Laser ignition pulses on the order of 100 ms contribute 35 mJ with the present system. With the reaction enthalpy of the fuel, one can calculate the thermopower wave efficiency threshold theoretically needed to ignite a new reaction and thus sustain an indefinite series of waves with net positive energy output. Based on the reaction enthalpies of picramide (-1450 J/g) and NaN_3 (-340 J/g), and using a typical 4:1 picramide/NaN_3 fuel composition, this threshold is about 6%, well within the thermodynamic limits of such high-temperature reactions.

When testing TWGs, a digital oscilloscope (Yokogawa DL 1735E or 2000) measures voltage, and a high-speed camera records the wave propagation at 1000 – 4000 frames/second (Canadian Photonic Labs, CPL-MS70KS2B90) with a Nikon, AF Micro-NIKKOR 60 mm f/2.8D macro lens for sample magnification. Two pyrometers (Raytek MM1MH and Omega OS4000) measure temperature at the left and right ends, respectively, of each SWNT fiber. The Raytek measures spectral response at 1 μm with a semiconductor photodetector and calculates temperature assuming (emissivity-adjusted) blackbody emission (accuracy: ± 0.3% + 1 K, range: 540 °C < T < 3000 °C). The Omega uses an InGaAs photo detector (spectral response: 1.2 to 2.6 μm, accuracy: ±1%, 350 °C < T < 1500 °C). Since carbon nanotubes are nearly blackbody emitters with little wavelength dependence in their emission, this approach is valid. Moreover, we measured the temperature-dependent emissivity of these SWNT fibers by comparing temperatures recorded by a type K thermocouple and a thermal camera (FLIR 7650). ε ranges from 0.82 to ~1 from ambient to reaction temperatures, and is $\geq$ 0.98 above 800 K, so it is nearly constant for the pyrometers.

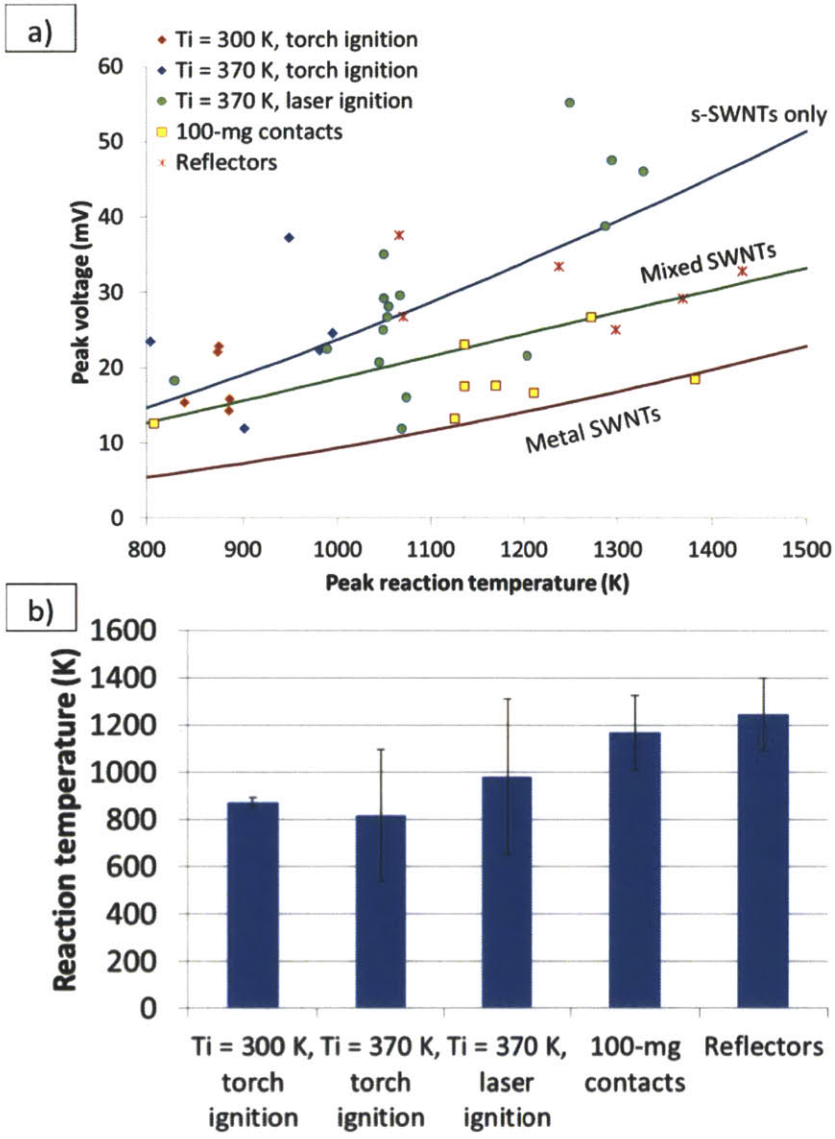

Figure 1: Peak voltage (absolute value) and reaction temperature for different ignition schemes and generator designs. a) Comparison of peak voltage with peak reaction T for PA-SWNT TWGs. Preheating and using a laser (rather than a butane torch) to ignite reaction can increase reaction temperature and voltage. The lines indicate Seebeck effect predictions for various mixtures of metallic and semiconducting (s-) SWNTs, assuming opposite-side T = 370 K. Default contact mass for other devices not specified is 200 mg; 100-mg-contact TWGs and TWGs with reflectors were also preheated to 370 K and laser-ignited. b) Reaction temperature for different TWG designs. By decreasing thermal losses from conduction and radiation, respectively, smaller contacts and reflectors can increase the reaction temperature of the picramide/NaN_3 mix, although not necessarily leading to larger voltages.

TWGs can generate larger peak voltage than the Seebeck effect predicts for a mixed SWNT fiber. Figure 1a compares absolute peak voltage to Seebeck predictions for several possible SWNT fiber compositions, based on the parameters described above and assuming the opposite temperature is 370

K (the preheat temperature). The Seebeck coefficient, Γ, depends on many factors in SWNT materials, including temperature,[10, 11] electronic type (*i.e.* metal or semiconductor), structural morphology (for example, alignment and void fraction),[12] and doping from adsorbed species.[13-15] A good model for SWNT macrostructures (like films or fibers) of mixed electronic type comes from Hewitt *et al.*'s measurements.[10]

$$\Gamma = aT \pm bT^{1/2} \exp[\pm(T_1/T)^{1/(1\pm d)}] \quad (3)$$

Here, *a* and *b* are coefficients defining the weight of metallic and semiconducting contributions, respectively, T_1 is a constant related to the energy barrier for carrier hopping between SWNTs (~20 K), and *d* is the dimensionality factor for the density of SWNT-SWNT junctions (= 2 for interconnected SWNT macrostructures where conduction is *via* percolation). Based on Hewitt *et al.*'s data, we calculate *a* = -0.022 and *b* = 2.0 for *T* in units of K and Γ in μV/K; thus, metallic and semiconducting SWNTs have opposite influence on the overall Seebeck coefficient. SWNTs in the KH fibers are not well aligned or sorted, and thus their Seebeck voltage is expected follow the trends of the two-component model of Hewitt *et al.* described above, the middle curve of Figure 1a.

Based on measured temperatures, one can predict peak voltage between the contacts at positions x_L and x_R using the Seebeck equation (3) for SWNTs.

$$V = \pm\int_{x_L}^{x_R} \Gamma \frac{\partial T}{\partial x} dx = \int_{T_R}^{T_L} \Gamma dT \quad (4)$$

After the change of variables, T_L and T_R denote the temperatures at those respective ends of the SWNTs. Since $|a| < b$ in equation (3), the prediction for m-SWNT (metals, with $b = 0$) is the lowest, and substantially under-predicts thermopower wave voltage. On the other hand, a fiber of only semiconducting SWNTs (s-SWNTs) would have $a = 0$ and therefore a larger magnitude Seebeck coefficient than a mixed fiber. Almost 50% of preheated, laser-ignited TWGs actually exceed the

predictions for s-SWNTs, despite the unsorted nature of the source SWNTs, suggesting that the thermopower wave can boost voltage over static thermal gradient limits.

On the other hand, increasing reaction temperature alone does not increase voltage beyond Seebeck predictions. Figure 1b compares reaction temperatures for different device designs and ignition methods. The standard TWG contact mass is about 200 mg; halving that with smaller copper strips and using a minimal amount of Ag paste does tend to increase reaction temperature but without boosting voltage. Independent of other factors (*i.e.* insulation design), the reaction temperature should be about equal across generators since they all used the same PA/NaN_3 mix for fuel and similar amounts of fuel relative to the mass of SWNTs. 100-mg-contact devices achieved higher temperatures (1200 ± 160 K, compared to 1000 ± 340 K for the standard laser-ignition TWGs). Lighter contacts have smaller thermal mass, and therefore $T_{contact}$ should increase more quickly as the reaction progresses, decreasing the flux through the contacts. These devices were also preheated to 370 K and laser-ignited.

Enclosing TWGs with broadband reflectors (particularly for the IR spectrum) could also decrease thermal losses; radiation should be a major mechanism because temperature is so high. Section 7.6 expands on this idea, calculating bounds for radiative fluxes from TWGs. The reflectors described in Figure 1 are stainless steel semi-cylinders smoothly coated with an Ag film *via* evaporation; Ag has >96% reflectance for light from 600 to 2000 nm, making it a highly effective thermal reflector. These TWGs used the standard 200-mg contacts and preheater-laser ignition. Although the reflectors have a higher average peak voltage than the 100-mg-contact devices (Figure 1a), they still do not measurably outperform TWGs without insulation. Devices with reflectors do reach higher reaction temperatures, 1200 ± 150 K, than un-insulated TWGs, however. This disconnect from voltage may suggest that the limiting factor for thermopower wave electricity generation is often not thermal losses but instead a thermal or electrical material property.

Besides increasing precision, the new preheater-laser ignition system also increases TWG voltage and temperature. The preheater has little effect on TWGs ignited with a fine-tip butane torch (Fig. 1), likely because the torch emits >100 W, making the preheater redundant. By contrast, the laser-ignited samples can react at temperatures up to 400 K higher with nearly double the peak voltage, although performance varies considerably. Note also that the increase in reaction temperature (Figure 1b) far exceeds the increase in initial temperature from preheating (70 K). Since preheating and laser ignition do not change thermal loss pathways relative to torch ignition and ΔH for the preheated samples is calculated at the preheat temperature, we may conclude that this ignition system increases the effectiveness of the chemical reaction, possibly the fraction of fuel reacted. It could also be that the torch raises the overall system temperature quite a bit more than 70 K because of its imprecision, which would decrease the magnitude of ΔT and therefore Seebeck voltage. The pyrometers can not measure T < 632 K, so any preheating from the torch below that level would not be detected.

7.4 Excess voltage and power

Based on the Seebeck predictions for SWNTs, one can calculate the excess voltage and power for TWGs. We define excess voltage as $V_{xs} = V_{out} - V_{TE}$, where V_{out} is the voltage produced by the generator and V_{TE} is the predicted thermoelectric (Seebeck) voltage. Excess power can likewise be defined.

$$P_{xs} = P_{out} - P_{TE} = \frac{V_{out}^2}{R_c} - \frac{V_{TE}^2}{R_c} \quad (5)$$

R_c is the circuit resistance, which is approximately the internal resistance of the SWNT fiber in the low-current limit of the experimental system. V_{TE} can be calculated according to equations (3) and (4) to provide values of P_{xs} for SWNT fibers of varying compositions, corresponding to different values of a and b in equation (3).

$$P_{xs} = \frac{V_{out}^2}{R_c} \square \frac{\left(\int_{T_L}^{T_R} \Gamma dT\right)^2}{R_c} \quad (6)$$

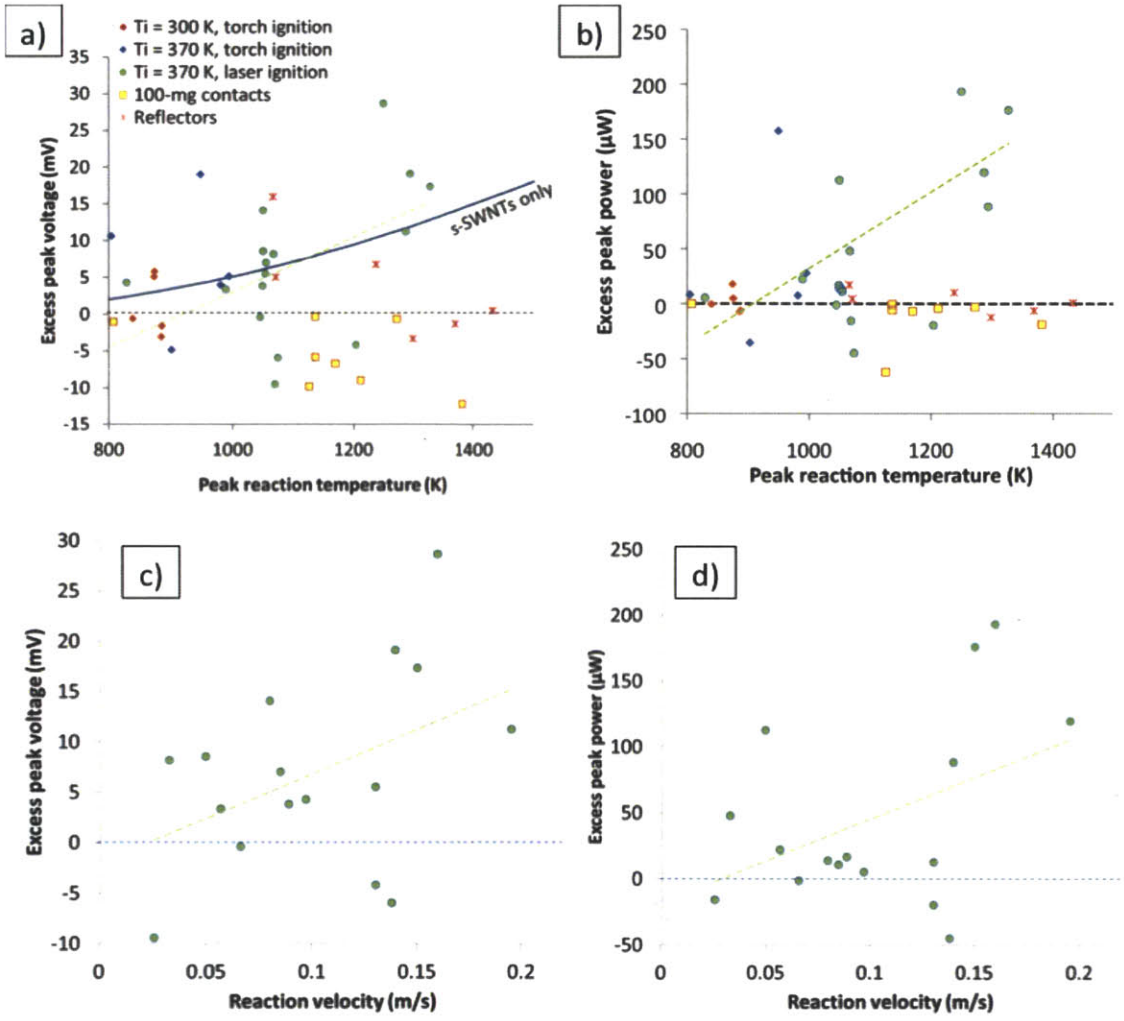

Figure 2: Voltage and power in excess of Seebeck predictions for mixed-type SWNTs. a) Of five device designs tested, only the preheated, laser-ignited, un-insulated TWGs had an average excess V > 0, increasing with reaction temperature. b) In standard laser-ignited, preheated devices excess peak power also increases with T, although more sharply than is the case for voltage. The dashed green line is included to guide the eye. c, d) Excess V and power, respectively, compared to reaction wave velocity for the best-performing TWGs as described above. The dashed lines are again guides to the eye. Excess V and power increase with increasing wave speed.

Figure 2 compares V_{xs} and P_{xs} in terms of reaction temperature and reaction wave velocity. The best-performing TWGs (preheated, laser-ignition, 200-mg contacts) do show a significant excess voltage and power that increases with reaction temperature and wave speed (Figure 2b-d), and often surpasses

predictions for s-SWNTs. Figure 3a reinforces this point by plotting P_{xs} when V_{TE} is calculated with Γ for s-SWNTs. Peak power varies more than voltage because of variable internal resistance, R_{int}, of TWGs, but P_{xs} is a significant fraction of the total peak power, as Figure 3b shows, 30 to 80%.

The increase in excess voltage and power with T could mean that the Seebeck coefficient of SWNTs increases more rapidly at high T than would be expected from Hewitt *et al.*'s data. In this case, the trend with increasing wave speed (Fig. 2d) would be simply a correlation and not causative. Modeling work has shown that, in non-dimensional terms, wave velocity c depends on the inverse adiabatic reaction temperature, $\beta = \frac{C_p E_a}{-\Delta HR}$,[8, 9, 16, 17] a trend that also holds for non-adiabatic waves.[18]

$$c \approx e^{-\beta/2} = \exp\left[\frac{-E_a}{2RT_{rxn}}\right] \tag{7}$$

T_{rxn} is the adiabatic reaction temperature, which should be approximately the peak reaction temperature measured. Although TWGs are not adiabatic, the thermal losses occur behind the front and decrease the temperature after the wave passes. The dimensional scaling factors for space and time are $\xi = x\sqrt{\left(\frac{\rho C_p}{\chi}\right)\left(\frac{k_o}{\beta}\right)}$ and $\tau = \left(\frac{k_o}{\beta}\right)t$, respectively. Thus, the temperature dependence for velocity v is

$$v = \sqrt{\frac{k_0 \chi}{\beta \rho C_p}} \exp\left[\frac{-E_a}{2RT_{rxn}}\right] = \sqrt{\frac{k_0 \chi RT_{rxn}}{\rho C_p E_a}} \exp\left[\frac{-E_a}{2RT_{rxn}}\right] \tag{8}$$

This model can reasonably predict the speed of thermopower waves using the peak reaction temperature as T_{rxn}, as Figure 3c shows. Since the SWNTs accelerate and guide the wave, we use thermal diffusivity $\alpha = \frac{\chi}{\rho C_p} = \alpha_i T^j$ of SWNTs fit to the the measurements and models of Li and Chou[19], Yu *et al.*[20] and Berber *et al.*[21] to determine the upper predictive bound, the limit of the SWNTs with best thermal properties. Here α_i = 6.95 m^2/s and j = -1.328 for T in K. NaN_3 should determine E_a, as the

initiator, so we use its value of 119 kJ/mol.[22] However, picramide will influence the overall reaction rate, so we use an arithmetic mean of the k_0 values for PA[23] and NaN_3,[24] corresponding to the ~1:1 ratio of these compounds in the fuel mixture. The conductivity of SWNT fibers from the experiments varied by a factor of 8.5, so the lower bound derives from scaling α_i to 0.82 m^2/s.

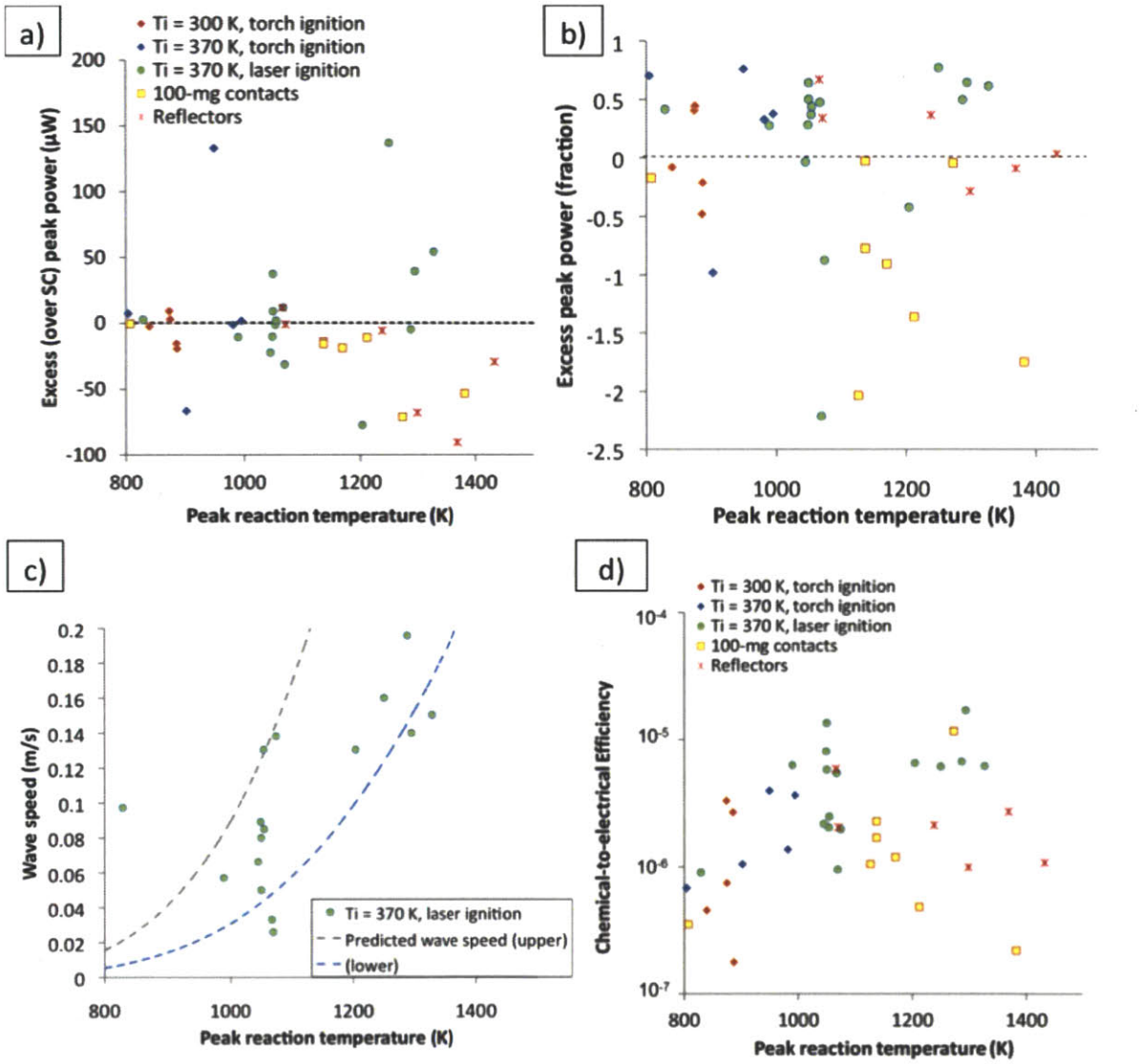

Figure 3: a) Excess thermopower as compared to predictions for s-SWNTs. Even this much larger Seebeck coefficient falls short of explaining the peak power of the best generators. b) The excess thermopower can be 30 to 80% of the total peak power magnitude in successful generators (green circles). c) Wave velocity increases with temperature; although experimental variations are significant, the values are in the range predicted by theory for one-dimensional solid reaction waves. Bounds are calculated from the range of SWNT thermal diffusivities in experiments. d) Chemical-to-electrical efficiency (*i.e.* the fraction of fuel energy converted to electricity). Preheating and using a laser rather than a butane torch to ignite reaction can increase efficiency by an order of magnitude by boosting reaction temperature (note the logarithmic vertical scale).

Notably, these TWGs still generate excess voltage despite the great material differences between the SWNT fibers (length <50 μm, many tube-tube junctions, low alignment) and the MWNT arrays used as thermal conduits in the first TWGs (length = 4 mm, high alignment).[7] The high degree of alignment and porosity of the arrays should cause the MWNTs to behave like many individuals generating thermopower in parallel. The Seebeck coefficient of an individual MWNT at 300 K is 80 μV/K, increasing linearly with temperature as expected from its metallic electronic nature.[25]

TWGs (excluding the 100-mg devices) range from R_{int} = 4 to 56 Ω (averaged over the temperature range of each reaction) with an average of 15 Ω, whereas the 100-mg devices range from 6 to 160 Ω with an average of 48 Ω. While setting up 100-mg devices, the internal resistance could vary as much as 50% depending on the strain on the SWNT fibers. SWNT resistance is very strain-sensitive, and shear stress on the contacts could also easily increase resistance. Thus, if stronger small contacts could be fabricated, it could stabilize R_{int} for these generators and allow them to utilize the higher reaction temperatures from decreased conduction losses, which could lead to higher power and efficiency.

Although the designs intended to decrease thermal losses (*e.g.* smaller contacts, reflectors), do not increase voltage or power, they could still increase efficiency of the reaction by prolonging the voltage pulse at equivalent magnitude, as might be expected from a more slowly cooling system. Specifically, we examine chemical-to-electrical efficiency (*i.e.* the fraction of fuel energy converted to electricity), based on the entire fuel enthalpy (no subtractions for fuel buried under contacts or un-reacted as detailed earlier), so the values could be higher with more precise TWG construction. Figure 3d shows, however, that these insulation designs do not significantly increase efficiency.

In Figure 3d the benefit of the preheater-laser system is clear again, as the efficiency of those TWGs is an order of magnitude greater than equivalent devices without preheat (initial temperature = 300 K) or ignited with the torch. This increase, in percentage terms, is actually larger than the increase in

the Carnot efficiency bounds. For the torch-ignited samples without preheat, the maximum temperature is 910 K, giving maximum efficiency of 67%, whereas the limit for laser-ignited samples is 72% (conservatively based on preheating to 380 K and maximum reaction temperature of 1350 K).

7.5 Chemical potential gradient from adsorbed fuel

To explain the excess thermopower, we may return to the drift-diffusion equation describing carrier motion.

$$J_e = \sigma \left(E - \frac{\nabla \mu}{e}\right) - L_{12} \nabla T \tag{9}$$

J is current, E is electric field, σ is electrical conductivity, μ is chemical potential, e is the elementary charge, and L_{12} is an Onsager coupling coefficient. Here properties are written in terms of electrons as the majority carrier.When current is small enough to neglect, one can solve for E and integrate between two contacts (at positions x_L and x_R) to obtain an equation for voltage.

$$V = \int_{x_R}^{x_L} \frac{\nabla \mu}{e} \mathrm{dx} - \int_{T_R}^{T_L} \Gamma \mathrm{dT} \tag{10}$$

With $\nabla \mu = 0$, the Seebeck coefficient is equivalent to $\pm L_{12}/\sigma$, with the sign the opposite of the majority charge carrier, and indeed thermoelectric materials are normally modeled this way because they are not differentially doped. Moreover, the doping does not change over time in static thermoelectric systems. However, for thermopower waves on nanostructures, μ could change dynamically during the reaction. In dispersed SWNTs, for example, all atoms are at the surface, so the molecular electronic states can be highly influenced by surrounding molecules, such as the adsorbed fuel molecules, if their electronegativity is sufficiently different. Thus, the chemical potential term could account for V_{xs} with different μ in the fuel-coated and bare SWNTs. Δμ is equivalent to the Fermi level shift, ΔE_F, which may be related to changes in carrier concentration, Δn_l, by the quantum capacitance, which is different for m- and s-SWNTs according to their respective Fermi velocities, v_F.

$$\Delta\mu = \Delta E_F = \frac{1}{3}\Delta n_{l,m} h v_{F,m} + \frac{2}{3}(\Delta n_{l,m} h v_{F,s}) \quad (11)$$

Here h is the Planck constant, and the factors of 1/3 and 2/3 account for the relative abundances of m- and s-SWNTs, respectively, in mixed fibers.

Raman spectroscopy can measure changes in carrier concentration (with units of carriers/length for 1D systems such as SWNTs) according to the shifts of peaks in the G^- band of SWNTs.[26, 27] Farhat *et al.* measured individual m- and s-SWNTs doping through a top-gate electrolyte, relating the shift in G^- to gate voltage, V_G. One can convert these experiment-specific measurements to a general relation between G^- peak position and n_l knowing that, in such experiments, V_G is proportional to n_l, with contributions from geometric and quantum capacitances.

$$V_G = \frac{n_l e}{C_G} + \frac{\Delta E_F}{e} \quad (12)$$

C_G is the geometric capacitance for Farhat *et al.*'s system. The G^- peak position shifts significantly with doping in m-SWNTs but much less for s-SWNTs, and Farhat correlated the two with his measurements Thus, one can calculate n_l changes for m- and s-SWNTs separately and combine them as in equation (11) to obtain the total $\Delta\mu$.

Both picramide and NaN_3 up-shift the G^- peak, indicating p-doping. Figure 4a shows this effect based on spectra from 50 locations on a bare SWNT fiber that we subsequently dosed with equal masses of PA and NaN_3. The average peak center shifts from 1553 cm^{-1} (bare SWNTs) to 1555 cm^{-1} with the addition of picramide, and then to 1558 cm^{-1} after NaN_3 addition. Although the individual shifts vary, the p values for the PA and NaN_3 distributions are 2×10^{-4} and $p = 5 \times 10^{-11}$, respectively, far less than 0.05 threshold, indicating they are statistically different from the bare SWNTs distribution. Control measurements with acetonitrile or water on a SWNT fiber showed no shift in the G^- peak, indicating that the fuel solvents do not contribute to doping.

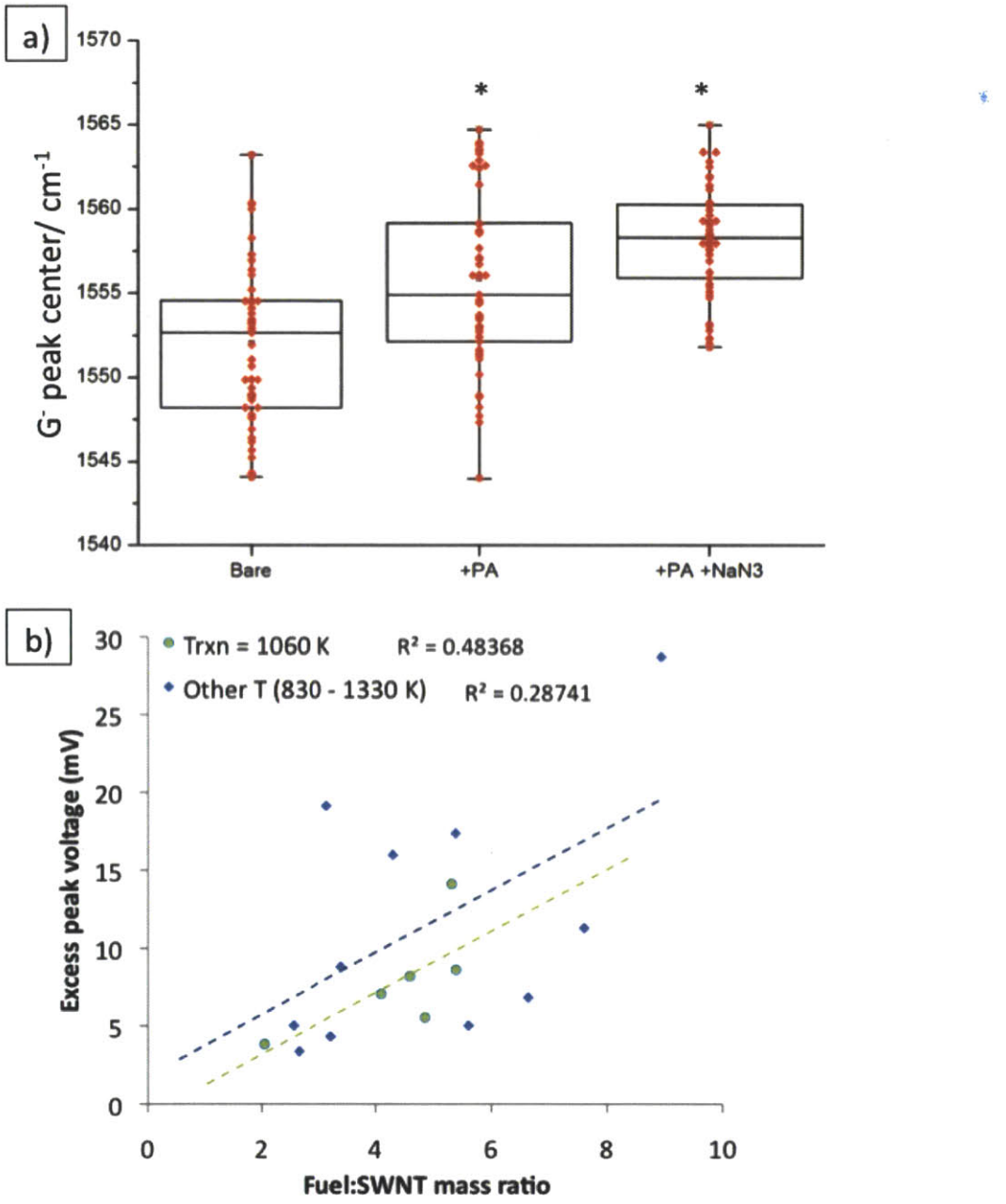

Figure 4: Doping from adsorbed fuel and excess voltage. a) Position of the Raman G⁻ peak shifts to higher wavenumbers as fuel is added to bare SWNTs. The boxes indicate the standard deviation of the measurements, and the central line is the average. The masses of PA and NaN_3 added were equal to that of the SWNT fiber. Graph courtesy of Bernat Sempere. b) From TWGs with excess voltage, the excess increases with proportion of fuel on the SWNTs. The correlation is stronger, controlling for ΔT (green points and line), as expected from a model like equation (10), summing contributions from doping and the Seebeck effect.

Using equation (12) and Farhat *et al.*'s Raman shift measurements, the 5 cm^{-1} shift from after PA and NaN_3 addition corresponds to Δn_l of 25 holes/μm (stated on the length scale of the SWNTs). This

change is equivalent to 10^{15} cm^{-3}, which can be a significant doping level, by analogy to bulk semiconductors. On the molecular level, the NO_2 groups of PA are strongly electron-withdrawing, which fits with the observed p-doping. As for NaN_3 the Na^+ ion is smaller and more stable than the azide anion, so it may tend to stay adsorbed somewhat more than N_3^-, leading to a net p-doping.

The chemical potential levels for bare and fueled SWNTs are thus 0.67 eV and 0.57 eV, respectively. Ambient atmospheric conditions will dope SWNTs to some degree, but the Fermi level of Farhat *et al.*'s SWNT at $V_G = 0$ sets the baseline for μ values. Regardless of the baseline, this difference shows that a reaction wave can create Δμ of 100 mV across the SWNTs, a value large enough to account for all experimental V_{xs} (maximum value 29 mV).

100 mV should represent an upper limit for Δμ in the PA-NaN_3-SWNTs system, and the actual devices may not reach it for several reasons. First, SWNTs in the fibers are not dispersed to the individual level, so fuel will not coat all surfaces equally, leading to incomplete electron transfer to fuel molecules. Figure 4b shows that increasing the fuel loading on the SWNTs tends to increase V_{xs}, which supports this idea. The trend is stronger among TWGs with the same reaction temperature (1060 K; R^2 correlation of 0.48, compared to 0.29 for all TWGs with $V_{xs} > 0$); this case minimizes variation in the second term (V_{TE}) of equation (10) to more clearly show the effects of Δμ. It is also possible that the reaction does not reach completion across the entire fiber, so μ behind the front could be < 0.67 eV. Overall, the distribution of Raman shifts (Figure 4a) indicates that different SWNTs can experience different doping levels, which will lead to some variability in V_{xs}.

7.6 Thermal losses from TWGs: Radiation

Because of its fourth-order temperature dependence, radiation is expected to be a major thermal loss mode for thermopower waves. Indeed, the fact that a (visible wavelength) camera can track the waves speaks to massive thermionic emission, as one can see in the reaction images of Figure 5a. Tracking the

wave front position allows a simple way of approximating radiative losses; by calculating the area behind the front (approximated as a rectangle) at each point in time, one can calculate a radiation rate from the sample for a given temperature distribution. The optically measured temperature can be corrected for increased accuracy using the temperature-dependent emissivity, $\varepsilon = f(T)$, also described previously, which includes surface roughness effects.

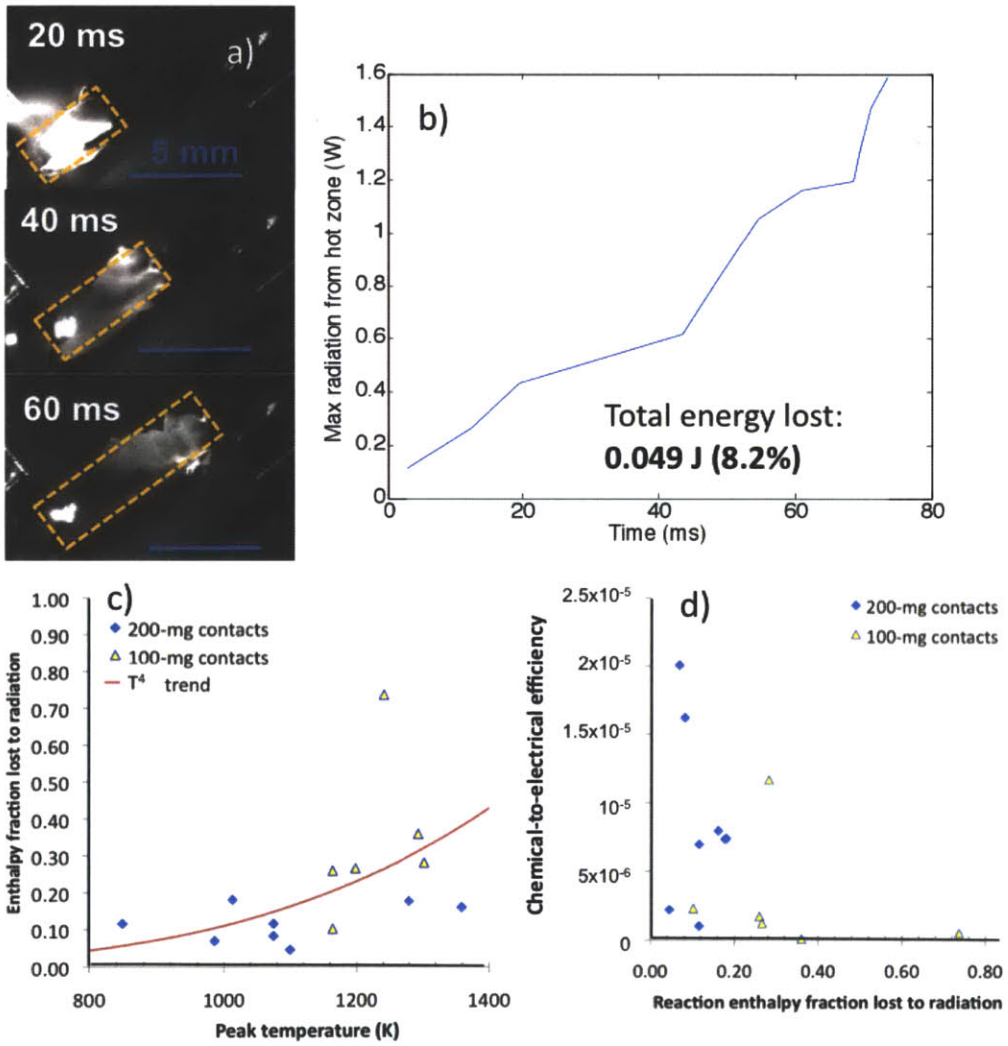

Figure 5: Calculating maximum radiation losses from thermopower waves. a) Example photos of a thermopower wave propagating on SWNTs. The laser ignition spot is visible in the lower left of each frame. b) Based on wave front position, one can calculate the hot zone surface area, and from there, the maximum thermal radiation rate (which assumes the entire hot zone is at T_{max}). Radiation continues to increase as the hot zone expands across the full length of the sample, varying with the speed of the wave. c) Total energy lost to radiation for each experiment, compared here to the total reaction enthalpy. The losses generally follow the expected T^4 dependence (trend line calculated for a median surface area). d) The most efficient reactions have the lowest radiation losses.

Assuming the whole area behind the front (the "hot zone") is at the peak temperature measured by the pyrometers yields the upper bound for radiation rate. Figure 5b shows an example of such a calculation, automated by a custom Matlab program. Since the wave speed is not constant, the rate of increase of radiation varies over the course of the reaction but is on the order of 1 W. Integrating the area under this curve yields the maximum energy that can be lost to radiation for a given reaction, which will depend, naturally, on the total amount of fuel available. Thus, Figure 5c is presented in terms of energy lost to radiation, normalized by the total reaction enthalpy for each sample. As expected, radiation energy loss generally follows the T^4 trend, although with one major outlier that had much larger surface area.

As one might expect, radiation losses are inversely related to the efficiency of electricity generation. Figure 5d shows this trend for the two sizes of contact explored in this work. Intuitively, if more energy is radiated away, less will be available to push charge carriers and generate thermopower. Thus, even with other major thermal loss mechanisms discussed in this work like hot product gases and conduction to the contacts, restricting radiation should be effective at increasing efficiency. However, Figure 3 shows that this is not the case for the particular design of semi-cylindrical reflectors.

7.7 Convection restriction and low pressure experiments

The enthalpy of reaction generally is calculated at a constant temperature. Using this isothermal value for efficiency calculations implies that the enthalpy of reaction products cooling to the initial temperature is available to the system for electricity generation. However, the products of these fuels are largely hot gases that can expand away before return that energy to the conduits. Based on measured reaction temperatures of 900 to 1100 K and published stoichiometry,[22, 28, 29]

thermodynamic analysis of the reactions of picramide and NaN_3 shows that up to 50 – 80% of the fuel enthalpy could be lost in the hot product gases. Nevertheless, design strategies to reduce convective thermal losses could also be effective in slowing the expansion of products such that they return more of their enthalpy to the system, which would be indicated by an increase in reaction temperature. Together, these three loss mechanisms can sap more than 90% of the available fuel energy; thus, design improvements should be able to boost efficiency by up to two orders of magnitude.

The remaining thermal loss mechanism to be explored is convection. A vacuum probe station allows testing of TWGs under low-pressure conditions to reduce or eliminate convection while maintaining electrical connections to measure voltage and to power the preheater. Less drastic measures to reduce convection, such as confining gas flow by covering the TWG with a glass slide to trap air between it and the preheater, still permit reaction but do not increase temperature or efficiency. The graph of Figure 6 includes these measurements, plus the standard preheated, laser-ignited TWGs described in earlier paragraphs for comparison. The glass slide ought to likewise restrict the expansion of hot product gases and keep more of their enthalpy available to the system, but with no change in reaction temperature, their enthalpy must be deposited elsewhere. A likely candidate is the slide itself, which is still much more massive than the fuel or SWNTs, so it would be a substantial thermal sink.

The next step would be to surround the TWGs with insulation, leaving only the contacts exposed. Carbon felt (slightly less porous than aerogel, but mechanically stronger) provided by Aspen Aerogels and ceramic alumina fiber mats are high-temperature insulators that do not easily react in air and therefore are good candidate materials. However, the insulation obstructed laser ignition, leaving the butane torch as the only available mechanism. A pyrometer can still measure temperature if aimed at an acute angle relative to the plane of the TWG, allowing it to measure under the edge of the insulation.

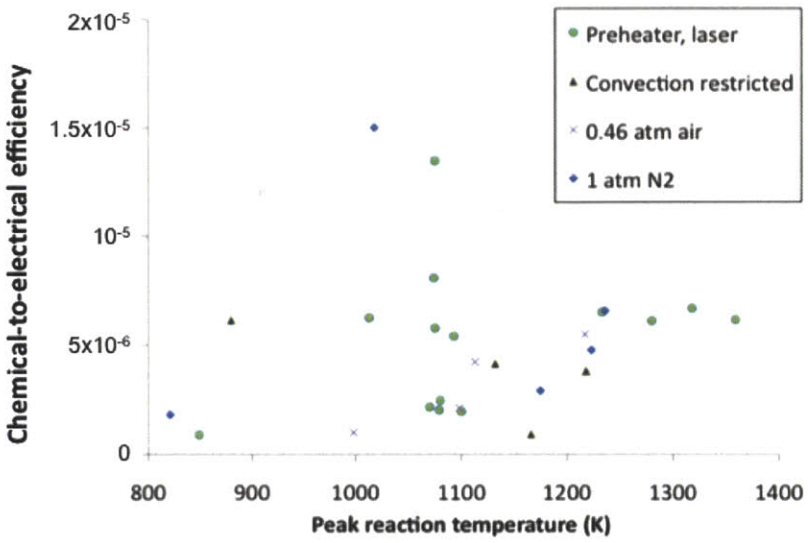

Figure 6: Effects of atmospheric conditions on efficiency. Neither decreasing pressure nor replacing the atmosphere with nitrogen increased reaction temperature or efficiency. Another approach to decreasing convection, by enclosing the generator with a glass slide to block gas flow, was likewise ineffective.

Generators covered with carbon felt reached 1100 ± 150 K, comparable to the standard un-insulated samples, whereas TWGs using ceramic insulation reacted at 930 ± 40 K. Again, efficiency did not measurably increase. Here the reason may be that thermopower waves do not propagate when the insulation contacts the generator, even using the relatively porous carbon felt or if one side of the generator is exposed to air. The insulation is again much more massive than the generators, so its capacity as a thermal sink is more influential than its convection blocking characteristics.

Thermopower waves can propagate without oxygen with picramide as a fuel, verified with reactions in a N_2 atmosphere. These TWGs had equivalent efficiency to generators reacting in air (Figure 6), but also exhibited voltage peaks of the same sign as reactions in air. This fact indicates that the doping of the SWNTs does not shift prior to reaction, as would be expected if O_2 desorbed during the evacuation of air (to 40 mTorr) before re-pressurization with N_2. It is likely, therefore, that the layers of picramide and NaN_3 on the SWNTs restrict the mass transfer of O_2, essentially trapping it on the SWNTs.

At 40 mTorr, no thermopower waves could be initiated with a laser (with or without preheating), despite its higher intensity (7 W/mm^2) than the system used in initial demonstrations of thermopower waves.[6] However, control experiments show that picramide degrades rapidly with preheating at these pressures, as one can see in the images of Figure 7a (tested at 525 Torr). The preheater is the orange rectangle beneath the picramide sample. The fact that TWGs preheated (to 100 ˚C) at pressures below 200 Torr would not react subsequently at atmospheric pressure supports this analysis. Sublimation of picramide at elevated temperatures is possible, but a small factor; its vapor pressure is only 1 mTorr, even at 100 ˚C. [30] The degradation reaction would be an undesirable side pathway that is insufficiently exothermic to sustain a self-propagating reaction wave.

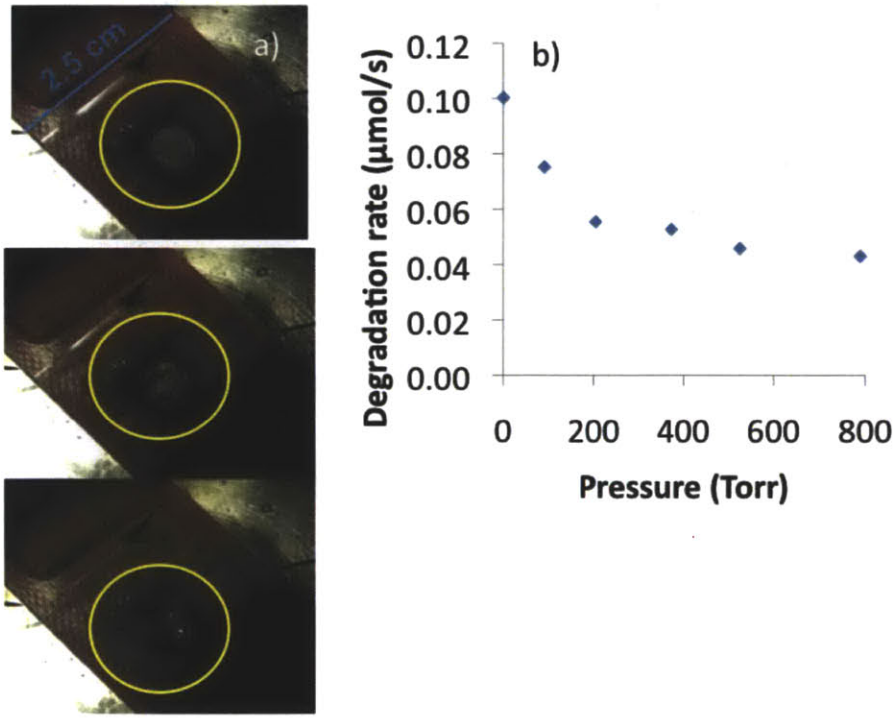

Figure 7: Degradation of picramide at lower pressures. a) Example photos of picramide degrading at 525 Torr, taken over the first minute of preheating (reaches 80 ˚C). The initial spot of fuel crystals changes color and no longer reacts after this heating. b) Degradation rates (measured visually) from ambient pressure down to 0.7 Torr.

Thermopower wave reactions with picramide are unlikely below 200 Torr because degradation takes about 30 seconds, about the same time needed to preheat (to 50 ˚C) successfully for reaction.

Figure 7b shows the results of additional picramide degradation controls at other pressures. The rapid rate of fuel degradation could offset any decrease in convection at lower pressures, explaining the results of tests at 0.46 atm (360 Torr) (Figure 6), where efficiency is not significantly different than tests at 1 atm. Another possible factor is that hot gases (products or preheated air) will expand away from the system more rapidly with less opposing pressure, leading to greater enthalpy losses.

7.8 Conclusions

When ignited precisely with a laser and preheated in a controlled manner to ~370 K, thermopower wave generators produce voltage and power in excess of the predictions of the Seebeck effect for SWNTs of mixed electronic type, 30 – 80% more. This excess voltage and power scales with temperature but also with the proportion of fuel loaded on the SWNTs. Raman analysis of fueled SWNTs shows an up-shift in the G^- peak of 5 cm^{-1}, equivalent to a doping of of 25 holes/μm, which can create a chemical potential difference of up to 100 mV. Fundamentally, since chemical potential differences can also drive carrier motion, differential doping between the reacted and un-reacted ends of the SWNTs can explain excess voltage. This work opens a new design space for thermoelectric devices, through intentional design of through doping. If the thermoelectric conduits are nanostructures, the adsorbed fuel creating the thermal gradient can also dynamically increase the potential gradient and output voltage of the generator during its reaction.

References

1. Albano, F., et al., *A fully integrated microbattery for an implantable microelectromechanical system.* Journal of Power Sources, 2008. **185**: p. 1524-1532.
2. Dudney, N.J., *Solid-state thin-film rechargeable batteries.* Materials Science and Engineering B Thin Films and Nanomaterials for energy Conversion and Storage, 2005. **116**(3): p. 245-249.
3. Kang, B. and G. Ceder, *Battery materials for ultrafast charging and discharging.* Nature, 2009. **458**(7235): p. 190-193.

4. Lee, S.W., et al., *High-power lithium batteries from functionalized carbon-nanotube electrodes.* Nat Nano, 2010. **5**(7): p. 531-537.
5. Armand, M. and J.-M. Tarascon, *Building better batteries.* Nature, 2008. **451**: p. 652-657.
6. Thomas, G., *Overview of Storage Development DOE Hydrogen Program*, 2000, Sandia National Laboratories: Livermore, CA.
7. Choi, W., et al., *Chemically Driven Carbon Nanotube-Guided Thermopower Waves.* Nature Materials, 2010. **9**: p. 423-429.
8. Abrahamson, J.T., et al., *Wave Front Velocity Oscillations of Carbon Nanotube-Guided Thermopower Waves: Nanoscale Alternating Current Sources.* ACS Nano, 2011. **5**(1): p. 367–375.
9. Abrahamson, J.T. and M.S. Strano, *An Analytical Solution to Coupled Chemical Reaction and Thermally Diffusing Systems: Applicability to Self-Propagating Thermopower Waves.* Journal of Physical Chemistry Letters, 2010. **1**(24): p. 3514–3519.
10. Hewitt, C.A., et al., *Varying the concentration of single walled carbon nanotubes in thin film polymer composites, and its effect on thermoelectric power.* Applied Physics Letters, 2011. **98**(18): p. 183110-3.
11. Zhang, H.L., et al., *Electrical and thermal properties of carbon nanotube bulk materials: Experimental studies for the 328-958 K temperature range.* Phys. Rev. B, 2007. **75**(20): p. 205407-205415.
12. Baxendale, M., K. Lim, and G. Amaratunga, *Thermoelectric power of aligned and randomly oriented carbon nanotubes.* Physical Review B, 2000. **61**: p. 12705-12708.
13. Bradley, K., et al., *Is the Intrinsic Thermoelectric Power of Carbon Nanotubes Positive?* Physical Review Letters, 2000. **85**: p. 4361-4364.
14. Sumanasekera, G.U., et al., *Effects of Gas Adsorption and Collisions on Electrical Transport in Single-Walled Carbon Nanotubes.* Physical Review Letters, 2000. **85**(1096-1099).
15. Sumanasekera, G.U., et al., *Giant thermopower effects from molecular physisorption on carbon nanotubes.* Physical Review Letters, 2002. **89**(16): p. 166801.
16. Please, C.P., F. Liu, and D.L.S. McElwain, *Condensed phase combustion travelling waves with sequential exothermic or endothermic reactions.* Combust. Theor. Model., 2003. **7**(1): p. 129-143.
17. Weber, R.O., et al., *Combustion waves for gases (Le=1) and solids (L->infinity).* Proceedings of the Royal Society of London Series a-Mathematical Physical and Engineering Sciences, 1997. **453**(1960): p. 1105-1118.
18. McIntosh, A.C., R.O. Weber, and G.N. Mercer, *Non-adiabatic combustion waves for general Lewis numbers: Wave speed and extinction conditions.* Anziam Journal, 2004. **46**: p. 1-16.
19. Li, C.Y. and T.W. Chou, *Quantized molecular structural mechanics modeling for studying the specific heat of single-walled carbon nanotubes.* Physical Review B, 2005. **71**(7): p. 075409-075414.
20. Yu, C.H., et al., *Thermal conductance and thermopower of an individual single-wall carbon nanotube.* Nano Lett., 2005. **5**(9): p. 1842-1846.
21. Berber, S., Y.-K. Kwon, and D. Tománek, *Unusually High Thermal Conductivity of Carbon Nanotubes.* Physical Review Letters, 2000. **84**(20): p. 4613-4616.
22. Potvin, H. and M.H. Back, *Study of Decomposition of Sodium Azide Using Differential Thermal-Analysis.* Canadian Journal of Chemistry-Revue Canadienne De Chimie, 1973. **51**(2): p. 183-186.
23. Maksimov, Y.Y. and E.N. Kogut, Russian Journal of Physical Chemistry, 1978. **52**: p. 805.
24. Mohan, V.K. and V.R.P. Verneker, *ROLE OF CRYSTAL IMPERFECTIONS IN THERMAL-DECOMPOSITION OF SODIUM AZIDE.* Journal of Physical Chemistry, 1976. **80**(2): p. 119-122.
25. Kim, P., et al., *Thermal transport measurements of individual multiwalled nanotubes.* Physical Review Letters, 2001. **8721**(21): p. 215502-215505.
26. Paulus, G.L.C., et al., *Charge Transfer in Junctions of Single Layer Graphene and Metallic Single Walled Carbon Nanotubes.* submitted, 2012.

27. Farhat, H., et al., *Phonon Softening in Individual Metallic Carbon Nanotubes due to the Kohn Anomaly.* Physical Review Letters, 2007. **99**(14): p. 145506.
28. Sonntag, R.E. and G.J.V. Wylen, *Introduction to thermodynamics: classical and statistical.* 3rd ed ed. 3rd ed., John Wiley & Sons1991: John Wiley & Sons.
29. Brill, T.B. and K.J. James, *Thermal decomposition of energetic materials. 61. Perfidy in the amino-2,4,6-trinitrobenzene series of explosives.* Journal of Physical Chemistry, 1993. **97**(34): p. 8752-8758.
30. Rosen, J.M. and C. Dickison, *VAPOR PRESSURES AND HEATS OF SUBLIMATION OF SOME HIGH MELTING ORGANIC EXPLOSIVES*, 1969, US Naval Ordnance Laboratory: White Oak, MD.

Chapter 8

Conclusions and Outlook

This thesis has developed thermopower waves as a novel and useful way of generating electricity from chemical fuels. Thermopower waves result when a thermal reaction wave self-propagates in a layer of fuel surrounding a thermal and electrical conduit with a high aspect ratio and large surface area, such as the prototypical carbon nanotube (CNT). The rapidly moving thermal gradient drives charge carriers, generating voltage and current. The second chapter develops a model to explain why interfacial thermal conductivity between fuel and conduit does not limit wave propagation speed. In the third chapter, this work shows a new analytical solution method for the kinetics and energy balance equations for a self-propagating reaction wave in a solid fuel. This method predicts wave velocity and temperature profile shape for a range of fuel properties. Chapter 4 expands this model with numerical solution to predict the frequency and amplitude of wave velocity oscillations, based on the chemical and thermal properties of the fuel and the conduit. These oscillations match the frequency spectra of voltage oscillations observed from thermopower waves.

This work also contains important experimental advances. Chapter 5 describes the testing of thermopower waves on fibers of CNTs functionalized with aromatic groups. Electronic defects from covalent bonding do not disrupt wave propagation or electricity production for all degrees of functionalization tested. Raman spectroscopy verifies low degrees of damage to the CNTs from thermopower waves, meaning they can be refueled for multiple reactions. With an innovative high-speed synchronized instrumental design, Chapter 6 reports the first simultaneous measurements of temperature, voltage, and wave position/velocity of thermopower waves. These data offer sufficient

detail to predict expected voltage pulses based on the Seebeck coefficient; doping shifts related to fuel desorption from CNTs and reaction behind the wave front help to explain why thermopower waves often produce unipolar voltage pulses, despite their non-adiabatic nature. With new temperature measurements, Chapter 7 confirms that many thermopower waves generate voltage and power in excess of the Seebeck effect predicted for mixtures of semiconducting and metallic single-walled carbon nanotubes (SWNTs). The excess voltage and power increase with reaction temperature and the ratio of fuel mass to mass of SWNTs, and the magnitude is of the order predicted for the chemical potential difference between fueled and bare regions according to Raman spectroscopy information about carrier concentration.

Improving efficiency is key to make thermopower wave generators a more practical energy technology. Chapter 7 also examines approaches to reduce energy losses on five fronts (conduction, convection, radiation, product enthalpy, and ignition). Of these, improving the precision of ignition with an electrical preheater and a focused 785-nm laser improves overall system efficiency. About 70 J/g of preheat energy is needed for successful laser ignition. For a typical 4:1 picramide/NaN_3 fuel composition, this threshold would require a 6% device efficiency to break even on continuous thermopower wave operation, where energy from one wave would start the next. Decreasing electrode mass does decrease conduction losses, as increased reaction temperature indicates, but also increases contact resistance, leading to no net efficiency gain.

Decreasing thermal losses in thermopower wave generators (TWGs) is a sizeable engineering challenge with numerous efficiency trade-offs. One could surround TWGs with layers of insulation, but this could limit fuel choices to those that do not require oxygen. Moreover, in a classic heat transfer problem, for approximately one-dimensional structures smaller than 1 mm in diameter that operate at high temperature, the increase in diameter from insulation actually increases radiation heat losses by

increasing the surface area. Thus, future efforts may focus more on material properties to increase thermoelectric conversion efficiency, rather than keeping more thermal energy in the system.

Chapter 6 indicates that SWNT fibers with a greater fraction of semiconductors would have a greater increase in Seebeck coefficient with temperature, increasing the voltage from thermopower waves. According to Hewitt *et al.*'s measurements on mixed SWNT films,[1] semiconductors contribute more strongly to SWNT thermoelectricity, and this relation holds for thermopower wave generators as well. Thus, with advances in SWNT sorting and separation,[2] fibers or yarns of purely semiconducting SWNT could be manufactured. Using macrostructures like yarns[3] also offers advantages for scale-up of TWGs, since they can be spun to meters in length.

Exploring dopants to maximize chemical potential differences will be a major area of thermopower wave research, since the dynamic carrier density difference created by the wave front is the source of the waves excess thermopower. A recent report showed a substantial increase in conductivity of double-walled carbon nanotube cables by the adsorption of iodine, where the best cables now exceed the specific conductivity of copper and aluminum.[4] With variations in CNT material preparation due to doping, electronic type, or porosity, screening CNT yarns based on thermal and electrical properties (before attaching them to contacts) could increase consistency of TWG performance.

On another front, thermopower wave "fuel cells" would also represent a big step past the first TWGs because they could generate power continuously with repeated liquid fuel injection cycles; previous devices could only make electrical pulses shorter than a second. With fuels like formic acid and methanol that can be biologically derived, TWGs could use renewable energy sources. Preliminary experiments have demonstrated that liquid fuels like formic acid, ethanol, hexane, or toluene will not ignite to produce self-propagating thermopower waves. However, the addition of catalysts such as Au nanoparticles lowers the activation energy, leading to the demonstration of thermopower waves using

formic acid and methanol. The fuel cell research community has explored the properties and catalysis of these fuels. [5, 6]

Nanoparticles of noble metals such as Au, Ag, Pt, or Pd are known to catalyze the decomposition of formic acid and small alcohols[7-9] and can be grown on CNTs by electrodeposition[10] or synthesized separately in solution and then deposited on the nanotubes.[11-13] Initial experiments have measured peak power generation of 0.1 – 0.3 mW, which can be repeated over at least 13 cycles. The velocity, as measured by high-speed camera, along the generator's length averages 0.6 mm/s fairly consistently over the cycles, two orders of magnitude slower than in the solid fuel picramide.

Reactions with liquid fuels add additional complexity to the system. Reactions occur in liquid and gas phases; oxygen is required to extract the full energy value (so the kinetics are not necessarily unimolecular); mass transport is non-negligible and, instead of the kinetics, may limit reaction rates. While these considerations may preclude a general analytical solution for wave propagation, it should still be possible to numerically simulate such systems using COMSOL and MATLAB.

The choice of catalyst(s) must optimize the activation energy; too low and the fuel will react spontaneously without being controlled by the nanotubes, too high and the required initiation energy will be too large, sapping the efficiency. Additionally, although metals like Pt, Ru, and Pd are the most active, they are also quite rare and therefore expensive. Thus, for liquid-fueled-TWGs to be practical, it would help to use more common metals like Au, Fe, or Cu[14] if their activity is sufficient. The formation of the metal formate species on the catalyst surface is generally the limiting step in formic acid decomposition.[9]

Overall, formic acid decomposition proceeds by one of two pathways: dehydrogenation (producing H_2 and CO_2, ΔG = -48.4 kJ/mol) or dehydration (products H_2O and CO, ΔG =-28.5 kJ/mol).[7, 15] The dehydrogenation reaction is more thermodynamically favorable but is actually endothermic at 300 K (+32 kJ/mol). Only when oxygen is then available to react with the H_2 is the overall reaction

(dehydrogenation plus combustion) exothermic: -210 kJ/mol, or -4570 J/g. Thus, for the most efficient reaction, oxygen must be supplied in excess, but the catalyst must also be carefully selected such that dehydrogenation is kinetically favored (since the decomposition is essentially irreversible).

The activation energy of the fuel could be determined not only by the composition of the nanoparticles, but also potentially by their form and their amount relative to the mass of CNTs and of fuel. The shape of nanoparticles, in the sense of crystal structure and which facets are exposed, is often critical to catalyst activity. The amount of catalyst could be a limiting factor if fuel molecules must diffuse too far to reach a catalyst particle. Finally, different catalysts could be deposited, together or subsequently, to obtain mixtures with precisely tuned average properties.

Ultimately, a self-contained TWG will likely require electrical reaction initiation; it appears to be the best way to integrate fabrication towards the goal of on-chip power sources. To make joule heating more efficient in TWGs, the electrical heater circuit should be built into the encapsulation or substrate such that it is very close (<1 mm) to the generator for the most efficient heat transfer. Some separation must be maintained to avoid electrical shorts.

While TWGs have produced impressive power densities so far, the solid fuels used react at very high temperatures, often around 800 °C. Liquid fuels would enable TWGs to spread into a much wider variety of applications through relatively lower-temperature operation. Formic acid[7] and methanol,[14] decomposing over metal nanoparticle catalysts on activated carbon supports, react at around 300 °C, although the temperature depends on the activation energy as determined by the catalyst. Additionally, the secondary combustion of hydrogen may influence reaction temperature. Comparing these measurements to simulations will identify heat loss mechanisms and predict the *adiabatic* reaction temperature, which will ultimately inform the safe design of the generators and help predict their maximum efficiency.

From thermodynamics, the Carnot limit bounds the efficiency for processes generating electricity (*i.e.* work) from a temperature difference. A reaction temperature of 300 °C yields a Carnot efficiency of 48% (assuming 25 °C ambient temperature), which is actually on par with the efficiency of molten carbonate or solid oxide fuel cells operating at much higher temperatures (500 to 750 °C).[16] At this efficiency, the maximum energy density of formic acid (in the limit of negligible generator system mass) is 2.2 MJ/kg, still three times larger than Li-ion. Biofuel-powered TWGs are thus promising portable power sources.

Initial studies of thermopower waves using solid fuels indicated that the CNTs survive the reaction with no detectable damage, prompting interest in their reusability.[17-19] Using Raman spectroscopy, one can measure what is called the D mode, characteristic of defects in graphene lattice structures like CNTs, and compare it to the G mode, characteristic of in-plane stretching of carbon bonds in the lattice (*i.e.* along the length of a CNT). The D/G ratio changes very little after one thermopower wave, as one can see in Chapter 5, even though CNTs should oxidize at least somewhat at the measured reaction temperature of ~ 800 °C in air.

Several hypotheses could explain the CNTs' survival. It may be that expanding wave of gases produced by the thermopower reaction displaces the air, creating an O_2-poor local environment. Perhaps secondary reactions with these product gases rapidly consume O_2 in the vicinity of the CNTs, which would be consistent with the de-doping evidence of Chapter 6. Or it could be that the thermopower wave is simply too fast for the CNTs to have enough time to oxidize. Since liquid fuel reactions described above require oxygen to fully release energy, answering this question is vital to efficient electricity generation while preserving the CNTs enough for multiple uses.

Fundamentally, new nanostructures that can control the direction and speed of reactions and convert heat to charge carrier motion (*i. e.* current) more efficiently will drive forward the science and application of thermopower waves. Materials with large Seebeck coefficients such as silicon nanowires,

bismuth telluride, or zinc oxide could be alternative thermal conduits, and thermopower waves could increase their figures of merit for electricity production from chemical reactions by utilizing the potential difference of doping between the two sides of the wave front. Hybrid nanostructures with catalysts open many new fuel options, particularly liquid fuels that can react at lower temperatures and permit refueling for continuous power generation. These investigations will lead the way to high-power, efficient, controllable thermopower wave devices.

References

1. Hewitt, C.A., et al., *Varying the concentration of single walled carbon nanotubes in thin film polymer composites, and its effect on thermoelectric power.* Applied Physics Letters, 2011. **98**(18): p. 183110-3.
2. Liu, H., et al., *Large-scale single-chirality separation of single-wall carbon nanotubes by simple gel chromatography.* Nat Commun, 2011. **2**: p. 309.
3. Aliev, A.E., et al., *Thermal transport in MWCNT sheets and yarns.* Carbon, 2007. **45**(15): p. 2880-2888.
4. Meng, C., C. Liu, and S. Fan, *A Promising Approach to Enhanced Thermoelectric Properties Using Carbon Nanotube Networks.* Advanced Materials, 2010. **22**(4): p. 535-539.
5. Wee, J.H., *Which type of fuel cell is more competitive for portable application: Direct methanol fuel cells or direct borohydride fuel cells?* Journal of Power Sources, 2006. **161**(1): p. 1-10.
6. Wee, J.H., *A feasibility study on direct methanol fuel cells for laptop computers based on a cost comparison with lithium-ion batteries.* Journal of Power Sources, 2007. **173**(1): p. 424-436.
7. Gazsi, A., T. Bánsági, and F. Solymosi, *Decomposition and Reforming of Formic Acid on Supported Au Catalysts: Production of CO-Free H2.* The Journal of Physical Chemistry C, 2011. **115**(31): p. 15459-15466.
8. Spendelow, J.S. and A. Wieckowski, *Electrocatalysis of oxygen reduction and small alcohol oxidation in alkaline media.* Physical Chemistry Chemical Physics, 2007. **9**: p. 2654-2675.
9. Knözinger, H. and K. Kochloefl, *Heterogeneous Catalysis and Solid Catalysts*, in *Ullmann's Encyclopedia of Industrial Chemistry*2000, Wiley-VCH Verlag GmbH & Co. KGaA.
10. Choi, H.C., et al., *Spontaneous Reduction of Metal Ions on the Sidewalls of Carbon Nanotubes.* Journal of the American Chemical Society, 2002. **124**(31): p. 9058-9059.
11. Wildgoose, G.G., C.E. Banks, and R.G. Compton, *Metal Nanoparticles and Related Materials Supported on Carbon Nanotubes: Methods and Applications.* Small, 2006. **2**(2): p. 182-193.
12. Mu, Y., et al., *Controllable Pt Nanoparticle Deposition on Carbon Nanotubes as an Anode Catalyst for Direct Methanol Fuel Cells.* The Journal of Physical Chemistry B, 2005. **109**(47): p. 22212-22216.

13. Qu, L. and L. Dai, *Substrate-Enhanced Electroless Deposition of Metal Nanoparticles on Carbon Nanotubes.* Journal of the American Chemical Society, 2005. **127**(31): p. 10806-10807.
14. Choi, Y. and H.G. Stenger, *Fuel cell grade hydrogen from methanol on a commercial Cu/ZnO/Al2O3 catalyst.* Applied Catalysis B: Environmental, 2002. **38**(4): p. 259-269.
15. Zhang, Y., et al., *Decomposition of Formic Acid in Supercritical Water.* Energy & Fuels, 2009. **24**(1): p. 95-99.
16. Steele, B.C.H. and A. Heinzel, *Materials for fuel-cell technologies.* Nature, 2001. **414**(6861): p. 345-352.
17. Choi, W., et al., *Carbon Nanotube-Guided Thermopower Waves.* Materials Today, 2010. **13**: p. 22-33.
18. Choi, W., et al., *Chemically Driven Carbon Nanotube-Guided Thermopower Waves.* Nature Materials, 2010. **9**: p. 423-429.
19. Abrahamson, J.T., et al., *Synthesis and Energy Release of Nitrobenzene-Functionalized Single-Walled Carbon Nanotubes.* Chemistry of Materials, 2011. **23**(20): p. 4557-4562.

Acknowledgments

Much of this material was supported under a National Science Foundation Graduate Research Fellowship. The Air Force Office of Scientific Research provided funding under grants FA9550-06-1-0 and FA9550-09-1-0700. Additionally, the MIT Energy Initiative and Undergraduate Research Opportunities Program funded a number of undergraduate students who explored thermopower waves with me.

Many great teachers over the years have kept my interest in science and engineering and bequeathed to me the knowledge and understanding I have today. First in this line were my parents, encouraging my inquisitiveness and omnivorous reading habits from my earliest years with a periodic table placemat, model rocketry, and many great hiking/camping trips, to name but a few.

The learning process of graduate school involves many times of frustration, lack of motivation, and fatigue. I would not have reached this point without the spiritual support of many friends and family members. I have been blessed to know wise and well-rounded chaplains at MIT through the Lutheran-Episcopal Ministry, first Tim Seitz and Amy McCreath, then later Janie Donohue and Kari Jo Verhulst. They were always present for me, even if all I needed was a place to breathe and pray together. Off campus at University Lutheran, I learned about the importance of retreats and life balance from Joanne Engquist, and Don Larsen would always stimulate my curiosity and wonder. Besides these pastors, I would like to thank my church family, the communion of saints, too many to name, that have held me up over these years. Melva James deserves particular gratitude for some important conversations in the difficult middle years of grad school while we both were really searching for what we wanted to do with our careers.

Other students at MIT pitched many times along the way, but I will single out a few here. Vicky Dydek was a cheerful and encouraging office neighbor for many years. Michael C. Stern assisted me with numerical simulations in Chapter 3. Also, Prof. Seunghyun Baik of Sungkyunkwan University provided vertically aligned MWNT arrays for the experiments of Chapter 4, and Prof. Kourosh Kalantar-zadeh was a valuable collaborator for the frequency analysis of those data.

Within the Strano group, I developed many great friendships and professional relationships. These co-workers, past and present, showed me how much better research can be as a team effort. Michael Walsh, Nicole Schonenbach, Joey Park, Jared Forman, Akshar Wunnava, Jenny Hu, and Evan Piephoff worked with me as undergraduate researchers. In particular, Michael designed circuitry to synchronize instruments to measure thermopower waves and wrote software to aid with the analysis of our data. Jared was a great brainstormer, ready with new ideas for problem solving when we encountered experimental difficulties. As anyone working in an experimental science would attest, this happens quite often. Michael and Ian McKay, a student of mine when I taught 10.27 Energy Engineering Project Lab, also taught me important things about electrical engineering.

Wonjoon Choi, who conducted the first thermopower wave experiments, continued to give advice and experimental tips after moving on to other projects. Paul Barone gave me great advice on writing a thesis, and Esther Jeng motivated me through the difficult middle years of grad school. Kevin Tvrdy contributed optics ideas aiding in the creation of the laser ignition system. Tom McNicholas constantly encouraged me and was a helpful brainstorming partner. Qing Hua Wang's knowledge was invaluable when I set up the vacuum probe station. Geraldine Paulus showed me her methods to relate Raman peak shifts to Fermi levels shifts, which I could adapt for my fuel doping studies. Zack Ulissi accelerated my final modeling work when he set up a powerful multi-core workstation for the lab, and he also helped me upgrade COMSOL.

Towards the end of my graduate work, several grad students began learning about thermopower waves from me, in the process often assisting with experiments. In particular I leave the project in the very capable hands of Bernat Sempere and Sayalee Mahajan. The past year Fatih Sen and Selda Sen have also aided me with sample preparation and discussions while they spearheaded their own investigations into liquid-fueled thermopower waves.

Holding this group together is my advisor, Prof. Michael Strano. Throughout grad school he was never short for scientific guidance and mentoring about the risks and rewards of academic careers. I appreciated his continual patience with my efforts while he still exuded driving enthusiasm for science in general and this project particularly.

Finally, I express my gratitude to my wife, Dorea Ruggles, for care, support, encouragement, and understanding as I put in long hours to complete this degree.